ISBN 978-82-326-4600-5 (printed version)
ISBN 978-82-326-4601-2 (electronic version)
ISSN 1503-8181

NTNU
Norwegian University of
Science and Technology

Doctoral theses at NTNU, 2020:126

Thomas Hansen Viuff

Uncertainty assessment of wave- and current-induced global response of floating bridges

A numerical investigation

Doctoral Thesis
Thomas Hansen Viuff

Doctoral theses at NTNU, 2020:126

NTNU

NTNU
Norwegian University of
Science and Technology
Faculty of Engineering
Department of MarineTechnology

NTNU
Norwegian University of
Science and Technology

Thomas Hansen Viuff

Uncertainty assessment of wave- and current-induced global response of floating bridges

A numerical investigation

Thesis for the degree of Philosophiae Doctor

Trondheim, May 2020

Norwegian University of Science and Technology
Faculty of Engineering
Department of MarineTechnology

NTNU
Norwegian University of
Science and Technology

NTNU
Norwegian University of Science and Technology

Thesis for the degree of Philosophiae Doctor

Faculty of Engineering
Department of MarineTechnology

ISBN 978-82-326-4600-5 (printed version)
ISBN 978-82-326-4601-2 (electronic version)
ISSN 1503-8181

Doctoral theses at NTNU, 2020:126

Printed by Skipnes Kommunikasjon as

Abstract

Floating pontoon bridge concepts have proven to be useful for crossing very deep and wide waters where conventional bridge types are not feasible, and different concepts have been built in several locations around the world within the last 70 years. Norway and the United States in particular have contributed to the capabilities of the technology and some of the most impressive floating pontoon bridge structures are currently located in those two countries, i.e. the Hood Canal Bridge in the United States and the Bergsøysund- and Nordhordland Bridges in Norway.

Today the Norwegian Public Roads Administration (NPRA) has proposed to establish several fixed links across the many wide and deep fjords in the western part of Norway and floating pontoon bridge concepts are among the proposed solutions. However, with the proposed concepts having unprecedented lengths of up to 5,000 m, the current understanding and technology related to floating bridges are pushed to their limits. Uncertainty in estimation of environmental design loads and the capabilities of existing numerical tools are some of the challenges considered for the new bridge structures and question fundamental pillars in the structural design.

The present thesis focuses on uncertainty assessment of the wave- and current-induced global response of curved floating pontoon bridges. The assessment includes investigation of the effect of uncertainties in design wave environments on the extreme response, and a comparison of two commonly used computer programs, i.e. Sima and OrcaFlex, when applied to floating bridge concepts. Furthermore, Sima is verified towards previous experiments of a generic floating pontoon bridge concept carried out in 1989 by Marintek (now SINTEF Ocean).

The findings suggest that, for the studied bridge concepts, the extreme response is only slightly affected by changes in the main wave direction for directions within $\pm 15^\circ$ from beam sea and for changes in the spreading exponent within naturally occurring values, i.e. 2 and 10. Furthermore, the responses calculated with the two computer programs, Sima and OrcaFlex, are within 5-15% of each other, when applied to the Bjørnafjord phase 2 floating pontoon bridge concept, selected by the NPRA. Finally, Sima is verified towards previous experiments for a generic floating pontoon bridge concept with a length of roughly 830 m, with a comparison close to the inherent experimental uncertainties of 5-10%. This is valuable knowledge for any future experiments of the selected floating bridge concepts, since the extreme lengths of the bridges necessitate the use of hybrid tests, which utilize numerical tools in the experimental measurements.

Acknowledgements

This study was conducted with financial support from the Norwegian Public Roads Administration. I gratefully appreciate this support which has enabled me to investigate a topic that is of great interest to me.

I would like to express my gratitude to my main supervisor, Prof. Bernt Johan Leira, for giving me the opportunity to work with floating offshore structures at the Norwegian University of Science and Technology (NTNU), known for its accomplishments within the field. Special thanks are extended to my co-supervisor, Prof. Ole Øiseth, for his keen ability to spot and improve upon areas of my research with a direct and to the point approach in our discussions. Furthermore, I want to give a sincere thank you to my co-supervisor, Dr. Xu Xiang, for his theoretical guidance within the topic of hydrodynamics and his practical work approach. Our friendly discussions have been a valuable pillar of support throughout the study. The late Prof. Ragnar Sigbjörnsson was my initial co-supervisor for the first eight months of the Ph.D. study and inspired me with his pioneering contributions to the field of stochastic response of floating bridge structures.

During my stay in Trondheim, I have met many new colleagues and friends whose help and support was a crucial part of my successful completion of the Ph.D. study. Particular individuals who deserve a special thank you are Sepideh Jafarzadeh, Mauro Candeloro, Seniz Ucar, Filippo Frontini, Yuna Zhao, Ping Fu and George Katsikogiannis.

Finally, my family deserves a sincere thank you for their support and understanding throughout my time here in Norway.

Preface

The present thesis is submitted in partial fulfilment of the requirements for the degree *Philosophiae Doctor* at the Norwegian University of Science and Technology. The work has been carried out at the Department of Marine Technology, Faculty of Engineering, with supervision from Prof. Bernt Johan Leira, Prof. Ole Andre Øiseth, Dr. Xu Xiang and the late Prof. Ragnar Sigbjörnsson. The present thesis is based on a collection of two published journal papers and one submitted journal paper.

Thomas Hansen Viuff

Trondheim, Norway
May 6, 2020

List of appended papers

The main part of the thesis is comprised of the following three appended papers:

Paper 1 **T. Viuff**, B. J. Leira, X. Xiang and O. Øiseth, "Effects of wave directionality on extreme response for a long end-anchored floating bridge", Applied Ocean Research, vol. 90, pp. 101843, May 2019. doi:10.1016/j.apor.2019.05.028.

Paper 2 **T. Viuff**, X. Xiang, B. J. Leira and O. Øiseth, "Software-to-software comparison of end-anchored floating bridge global analysis", Bridge Engineering, vol. 25(5), pp. 04020022, March 2020. doi:10.1061/(ASCE)BE.1943-5592.0001545. Final draft with permission from ASCE.

Paper 3 **T. Viuff**, X. Xiang, O. Øiseth and B. J. Leira, "Model uncertainty assessment for wave- and current induced response of a curved floating pontoon bridge", Applied Ocean Research. Preprint under review.

Other scientific contributions

The following papers resulted from the work during the Ph.D. study, in addition to the three appended papers:

T. Viuff, X. Xiang, B. J. Leira, and O. Øiseth, "Code-to-code verification of end-anchored floating bridge global analysis", In proceedings of the 37th International Conference on Ocean, Offshore and Arctic Engineering, pp. 1-9, June 2018. doi:10.1115/OMAE2018-77902.

X. Xiang, **T. Viuff**, B. J. Leira, and O. Øiseth, "Impact of hydrodynamic interaction between pontoons on global responses of a long floating bridge under wind waves", In proceedings of the 37th International Conference on Ocean, Offshore and Arctic Engineering, pp. 1-10, June 2018. doi:10.1115/OMAE2018-78625.

T. Viuff, B. J. Leira, and O. Øiseth, X. Xiang, "Methods for Preliminary Analysis of Floating Bridge Structures", In proceedings of the 13th International Symposium on PRActical Design of Ships and Other Floating Structures (PRADS), DTU Mechanical Engineering, Technical University of Denmark, September 2016. http://hdl.handle.net/11250/2446697.

T. Viuff, B. J. Leira, and O. Øiseth, X. Xiang, "Dynamic Response of a Floating Bridge Structure", In 19th Congress of IABSE, Challenges in Design and Construction of an Innovative and Sustainable Built Environment, The International Association for Bridge and Structural Engineering (IABSE), September 2016. http://hdl.handle.net/11250/2469567.

Declaration of authorship

The thesis is a collection of papers and is written by myself with supervision from my main-supervisor Prof. Bernt Johan Leira and my two co-supervisors Prof. Ole Øiseth and Dr. Xu Xiang. The supervisors have contributed to the thesis with their comments and guidance on which topics were relevant for the thesis. Below is a summary of the contributions from each author to the appended papers.

Paper 1

Prof. Bernt Johan Leira initiated the idea of the research and I was responsible for establishing the numerical model, calculating the stochastic response and writing the paper. Our colleague Dr. Ping Fu was a great help in implementing the correct calculation method for the extrapolated average extreme values used in the parametric study. Prof. Ole Øiseth and Dr. Xu Xiang were both helpful in giving constructive comments on the method used and on the writing of the paper. Prof. Ole Øiseth was particularly involved in writing the abstract and introduction of the paper.

Paper 2

Dr. Xu Xiang and I initiated the idea of the research together and based on an existing numerical model in OrcaFlex from Dr. Xu Xiang, I was responsible of making a numerical model in Sima as similar as possible. The calculations and extraction of the relevant responses was done in OrcaFlex by Dr. Xu Xiang and in Sima by myself. I was responsible of handling the data, deciding on which responses to compare, creating the figures and writing the paper. Prof. Bernt Johan Leira and Prof. Ole Øiseth were both responsible for constructive comments on which results to compare and the writing of the paper. Prof. Ole Øiseth was particularly involved in writing the abstract and introduction of the paper.

Paper 3

Dr. Xu Xiang and I initiated the idea of the research together and Dr. Xu Xiang was responsible of providing crucial information regarding the experiments, such as internal reports in the NPRA. I was responsible of creating the numerical model in Sima, manually extracting data from the internal reports, deciding on how best to verify the model against the results, which results to compare with and the writing of the paper. Dr. Xu Xiang helped me with troubleshooting of the numerical model and setting up the wave-current calculation in Wadam. Both Dr. Xu Xiang, Prof. Bernt Johan Leira and Prof. Ole Øiseth were responsible for constructive comments on which results to compare and the writing of the paper. Prof. Ole Øiseth was particularly involved in writing the abstract and introduction of the paper.

Nomenclature

Abbreviations

ACER	Average conditional exceedance rates
CDF	Cumulative distribution function
COB	Centre of buoyancy
COG	Centre of gravity
c.o.v.	Coefficient of variation
DOF	Degree of freedom
FEM	Finite element method
FPSO	Floating production storage and offloading system
GEV	Generalized extreme value
IFFT	Inverse fast Fourier transform
ISORM	Inverse second order reliability method
JONSWAP	Joint North Sea Wave Project
LC	Load case
MWL	Mean water level
NTNU	Norwegian University of Science and Technology
NPRA	Norwegian Public Roads Administration
PDF	Probability density function
QTF	Quadratic wave load transfer function
RAO	Response amplitude operator
SFTB	Submerged floating tube bridge

List of symbols

A_j	Cross-section area
A_{jk}^{∞}	Potential added mass at infinite frequency
$a_{jk}(\omega)$	Potential frequency-dependent added mass matrix
$b_{jk}(\omega)$	Potential damping matrix
C_{jk}	Hydrostatic stiffness matrix
C_j^d	Drag coefficient
C_{X_e}	Coefficient of variation of extrapolated extreme
D_{jk}	Structural damping matrix
$D_\zeta(\theta)$	Directional spreading function
$E[\cdot]$	Expected value
f_{BC}, f_{EI}	Modifying factors in Model 3
$f_X(x)$	Probability density function of instantaneous values
$f_{X_m}(x)$	Probability density function of individual maxima
$f_{X\dot{X}}(x,\dot{x})$	Joint probability density function of X and $\dot{X}$
$F_{X_m}(x)$	Cumulative distribution function of individual maxima
$F_{X_e}(x)$	Cumulative distribution function of extreme value
g	Gravitational acceleration
H_s	Significant wave height
$H_j^{(1)}(\omega,\theta)$	First order wave force transfer function
$H_j^{(2-)}(\omega_l,\omega_m,\theta_n)$	Simplified difference frequency QTF
i	Imaginary unit
K_{jk}	Structural stiffness matrix
$k_{jk}(t)$	Retardation function matrix
k_m	Wave number
M_{jk}	Structural mass matrix
M_y, M_z	Weak- and strong axis bending moments
N_m	Number of global maxima
N_ω	Number of frequencies
N_θ	Number of wave directions

$P\{\cdot\}$	Probability
$q_j^{exc}(t)$	Excitation force
$q_j^{(1)}(t)$	First order wave force
$q_j^{(2)}(t)$	Second order wave force
$q_j^{(d)}(t)$	Viscous drag force
Q_y, Q_z	Shear forces
$\Re(\cdot)$	Real part of complex number
R_x	Torsional rotation
s	Spreading exponent
$S_\zeta(\omega)$	Unidirectional wave spectrum
t	Time
t_{mem}	Memory time
T_e	Effective tension
T_n	Natural period of mode n
T_p	Peak period
$u_k(t)$, $\dot{u}_k(t)$, $\ddot{u}_k(t)$	Time dependent displacement-, velocity- and acceleration vectors
$\dot{u}_r$	Relative fluid velocity
x_m	Positive maximum
x_e	Extreme value
γ	Peak enhancement factor
$\Gamma(\cdot)$	Gamma function
δ	Weibull location parameter
ε_{nm}	Random phase
θ	Wave direction
θ_0	Main wave direction
λ	Weibull scaling factor
μ_{X_e}	Extrapolated extreme
$\overline{\mu_{X_e}}$	Average extrapolated extreme
$\nu_+(\xi)$	The ξ-level upcrossing frequency
ξ	Positive upcrossing level

ρ	Water density
$\sigma_v(t)$	Von Mises stress as function of time
σ_x, $\sigma_{\dot{x}}$	Standard deviation of x and $\dot{x}$
$\overline{\sigma_{X_e}}$	Standard deviation of extrapolated extreme
$\sigma_{xx}(t)$	Normal stress as function of time
τ	Time lag
$\tau_{xy}(t)$, $\tau_{xz}(t)$, $\tau_{xx}(t)$	Shear stresses as function of time
υ	Weibull shape factor
$\varphi_{H^{(1)}_{jnm}}$	Phase angle of the first order wave force transfer function
$\varphi_{H^{(2-)}_{jnlm}}$	Phase angle of the simplified difference frequency QTF
ω	Angular wave frequency
ω_p	Peak angular wave frequency

Contents

Abstract i
Acknowledgements iii
Preface v
List of appended papers vii
Other scientific contributions ix
Declaration of authorship xi
Nomenclature xiii

1 Introduction **1**
1.1 Background and motivation 1
1.1.1 Early recordings of floating bridge structures 1
1.1.2 Making floating bridges a part of modern infrastructure 2
1.1.3 The Ferry Free Coastal Highway Route E39 Project in Norway 3
1.1.4 Current challenges for floating bridges with unprecedented lengths 3
1.2 Objectives and scope 5
1.3 Structure of the thesis 7

2 Overview of theories and methods used **9**
2.1 Predicting floating bridge global response 9
2.1.1 Overview of the coupled hydro-elastic computer program 9
2.1.2 Governing dynamic relations and environmental loads 10
2.1.3 Solving the time domain equation 13
2.2 Practical aspects of the numerical models 13
2.2.1 Brief description of the Bjørnafjord phase 2 concept 14
2.2.2 Modelling the bridge girder, columns, tower and pre-tensioned stay cables 14
2.2.3 Modelling the hydrodynamic properties of the pontoons 15
2.3 Extreme response prediction 16
2.3.1 Statistics of a stationary and narrow-banded Gaussian process 16
2.3.2 Extreme value statistics 17
2.3.3 Relevant methods to obtain extreme response 18
2.3.4 Extreme value estimation based on a Weibull initial maxima distribution . 18
2.3.5 Procedure in first paper when estimating extreme response 19

3 Effect of wave direction uncertainty **21**
3.1 Bridge concept and methodology 22
3.1.1 Description of the bridge concept and choice of load cases 22

3.1.2 Method for estimating the extreme Von Mises stress response 23
3.2 Important findings 24
3.2.1 Reference for choice of number of realizations and realization length . . . 24
3.2.2 Effect on extreme response for changing main wave direction and spreading exponent 24

4 Assessment of numerical uncertainty 27
4.1 The bridge concept and methodology 27
4.1.1 The Bjørnafjord phase 2 floating bridge concept 27
4.1.2 Modelling differences 27
4.1.3 A step-by-step comparison method 28
4.2 Important findings 29
4.2.1 Natural periods and modeshapes 29
4.2.2 Response amplitude operators 29
4.2.3 Attention to modelling details for short-crested waves 29
4.2.4 Comparison of response from second order wave loads 30
4.2.5 Comparison of viscous damping effects 30
4.2.6 Final concluding remarks 31

5 Verification towards previous experiments 33
5.1 Description of the 1989 experiments used for verification 34
5.1.1 Measurement instrumentation 35
5.1.2 Overview of tests performed in the experiment 35
5.1.3 Uncertainties in measured response 35
5.2 Important findings 35
5.2.1 Verification of static response and modal properties 35
5.2.2 Sensitivity towards drag coefficient values 36
5.2.3 Directional sensitivity for beam sea 36
5.2.4 Response from short-crested wave loads 37
5.2.5 Current-wave interaction effects 37

6 Concluding remarks 39
6.1 Original contributions 39
6.2 Limitations and future work 40

References 43

Appended papers 49
Paper 1: “Effects of wave directionality on extreme response for a long end-anchored floating bridge” 49
Paper 2: “Software-to-software comparison of end-anchored floating bridge global analysis” 63
Paper 3: “Model uncertainty assessment for wave- and current-induced global response of a curved floating pontoon bridge” 87

Previous Ph.D. theses published at the Department of Marine Technology, NTNU 103

1 Introduction

1.1 Background and motivation

1.1.1 Early recordings of floating bridge structures

Various floating bridge concepts have been used throughout history to provide temporary passage over calm rivers, lakes or straits. Often such temporary structures have been used for military purposes and were not built to withstand the more extreme conditions during stormy weather.

The earliest record of a temporary floating bridge structure is found in the *Shih Ching* (Book of Odes) [1] written during the Zhou Dynasty in ancient China between the 11th and 8th century BC. The concept described in the Book of Odes was a combination of ships, that were used as transverse buoyant beams, with wooden planks on top of them. This concept was used throughout the Zhou Dynasty and was first made into a permanent floating bridge concept in 257 BC during the Qin Dynasty [2, p. 160]. Other early historic examples of floating pontoon bridges are from the period of military conflicts between the old Greek and Persian civilizations around 500 BC in the Northwest of modern day Turkey. During the war against the Scythians in 514 BC, the Persian king Darius I crossed the Bosphorus Strait using a bridge made of boats [2; 3]. His son Xerxes I later on in 480 BC crossed the Dardanelles Strait at Hellespont during the second Persian invasion of Greece using a similar floating bridge concept. The two temporary floating pontoon bridges are thought to have been roughly 2,000 m long and to have consisted of 314-360 ships connected by wooden planks. Later on in 40 AD, the Roman Emperor Caligula ordered the construction of a floating bridge to be built across the Bay of Naples, with the purpose of him riding across it purely for his own amusement [4]. The bridge is thought to have been roughly 4,000 m long and a few days after the triumphant event, a storm hit the bridge and an estimated 2,000 ships that were otherwise needed for transportation of grain, were either destroyed or driven ashore, leading to a serious food-shortage in the city [4].

As the previous examples indicate, although the historical facts are still being discussed, floating pontoon bridges were clearly used for various purposes throughout history as both temporary and permanent structures. Since then, similar bridge concepts have been used for the same reasons and have all met similar fates. Only within the last 50 years have the understanding and methods to properly predict environmental loads and the dynamic behaviour of a floating structure become reliable enough to be used for modern infrastructure. A thorough list of modern day floating bridges are given by Kvåle [5] and notable concepts are the First Bridge on Lake Washington (1940) and the Hood Canal Bridge (1961) in the United States, the Bergsøysund Bridge (1992) and the Nordhordland Bridge (1994) in Norway and more recently the Yumemai Bridge (2000) in Japan [6].

(a) The Hood Canal Bridge concept in the United States. Photograph by Robert Cortright/www.structurae.net.

(b) The Nordhordland Bridge concept in Norway. Photograph by www.aas-jakobsen.com.

Fig. 1: Different floating bridge concepts. (a) A straight floating bridge kept buoyant by a single continuous pontoon and stiffened horizontally by side anchors. (b) A curved floating bridge with discrete pontoons, stiffened horizontally by the curved geometry.

1.1.2 Making floating bridges a part of modern infrastructure

The level of sophistication in the design of floating bridges is based on many previous achievements within ocean engineering, applied mathematics, physics, computer science, etc. and it is outside the scope of this introduction to include the historical perspective in its entirety. Instead, only the most relevant findings directly related to the development of the design of floating bridges in short-crested sea are listed in the following.

The inherent random nature of waves and wind and its effect on the dynamic behaviour of floating bridges was not initially a part of the design [5] and it is safe to assume that this was the main cause of the many structural failures. In the 70s and 80s pioneering research in the field of stochastic wave and wind load processes and their application in stochastic response estimation of floating bridges was simultaneously carried out by two research groups, each working on their own concept, see Fig. 1. One group was located in the United States and focused on the Hood Canal Bridge design, i.e. a straight bridge floating on a continuous pontoon with side anchors to keep it in place. The other group was located in Norway and mainly focused on the Nordhordland Bridge (at the time referred to as the Salhus Bridge). Today the Nordhordland Bridge floats on discretely separated pontoons, but the design considered at the time consisted of a horizontally curved bridge floating on a continuous concrete pontoon.

In the United States, the research was lead by Hartz, Richey, Mukherji and Georgiadis [7–9], who measured the dynamic response of the Hood Canal Bridge and the corresponding wave loads, calculated correlation coefficients between the two and developed a numerical model of the floating bridge. The dynamic response was studied in the frequency domain and short-crested waves were incorporated using a spatial correlation factor applied to the wave forces.

Simultaneously in Norway, the research was lead by Holand, Langen and Sigbjörnsson [10–14] who investigated the structural response of the Nordhordland Bridge during the 70s. The investigations were conducted in the time domain using both regular and irregular long-crested waves. Short-crested waves were first explicitly incorporated in a frequency domain solution by Sigbjörnsson [15] by using coherency functions, which were dependent on the spreading exponent and the spatial coordinates to account for the correlation between the wave loads. In the following year, Langen and Sigbjörnsson [16] investigated the stochastic response due

to short-crested waves in the time domain. They concluded that it was important to include short-crested waves in the design in order to have less conservative solutions. In the 80s Langen, Leira and Øderud [17–20] studied the sensitivity of the probabilistic design of the same initial design concept of the Nordhordland Bridge using both frequency- and time domain methods. They found a high sensitivity towards the peak period of the wave spectrum as well as the spreading exponent. They also found a low correlation between the response bending moments, which was important to take into account in the design.

Through the strong collaboration between NTNU, SINTEF Ocean and the Norwegian companies involved in the design and construction, the decades of research were able to mature the design into the two existing floating bridges in Norway today, i.e. the Nordhordland Bridge and the Bergsøysund Bridge. Both concepts have proven to be capable of withstanding the wind and wave conditions in Norway for the last 25 years.

1.1.3 The Ferry Free Coastal Highway Route E39 Project in Norway

Based on the previous success, the Norwegian Public Roads Administration (NPRA) has embarked upon a big national project of reducing the travel time by half along the west coast of Norway between Kristiansand and Trondheim. This includes construction of permanent structures across some of the many deep and wide fjords. With some of the fjords having extreme depths of up to 1,300 m and widths of up to 5,000 m, conventional bridges are not possible and other options need to be considered. These are either a regular suspension bridge, a multi-span suspension bridge with floating pylons, a submerged floating tube bridge (SFTB), a floating pontoon bridge or a combination thereof. In either case, the selected concept will have unprecedented dimensions and pose several unique challenges.

1.1.4 Current challenges for floating bridges with unprecedented lengths

Regardless of which floating bridge concept is chosen by the NPRA to be built, there are several new challenges associated with the extensive length of the structure. The following is a short description of some of the most distinct challenges for the selected floating pontoon bridge concept and the investigations done in order to better understand them.

With the considerable length of the structure, it is likely that the design will become more slender and hence more prone to dynamic excitation from random loads from waves and wind. For this reason, a thorough understanding of the dynamic behaviour is crucial for a safe design. The work initiated in the 70s and 80s made it possible to investigate the dynamic behaviour of floating bridges and many investigations were made on bridges with lengths up to 1,500 m. The fact that the lengths of the planned floating concepts are 3-4 times longer than the lengths of similar existing concepts, makes it questionable whether or not the previously established knowledge is still valid. Furthermore, a study by Moan et al. [21] suggests that the long-term fatigue stress and extreme response of offshore structures are sensitive to the amount of available data when estimating the long-term changes of the statistical properties of the wave environment. Bitner-Gregersen et al. [22] found that between three metocean databases, a difference of 5 m in the significant wave height and 4 s in the zero-crossing period for a 100-year return period can be found. Another study on simulated wave data such as Kvåle and Øiseth [23], suggests that the estimated directional wave spectrum depends on the wave sensor layout and the methods used to analyse the data. The extensive length of the selected bridge concept and the previously mentioned studies suggest that it is important to investigate how sensitive the structural responses

are towards different wave parameters. Following the findings between the 70s and 90s, a list of such parameters should include significant wave height and peak period of the wave spectrum, wave direction, spreading exponent and pre-tension force.

In standard design of offshore structures, the wind and wave processes are assumed to be stationary and homogeneous, which means that the statistical properties do not change over time and space, respectively. The stationary assumption is normally valid as long as the time window is kept within 3 hours, commonly referred to as a short-term response analysis. The homogeneous assumption is usually irrelevant since the structure in question usually is restricted to a relatively small area of the ocean. When planning to built a floating bridge more than 4,500 m long, this assumption can, however, be violated and the inhomogeneous assumption of the wind and wave loads has to be investigated. Cheng et al. [24] investigated the wave conditions in the Bjørnafjord using field measurements from three Datawell Waveriders spread out over the width of the fjord with a distance of up to 2831 m. The measurements were recorded over a period of roughly 19 months and the wave environment was concluded to be inhomogeneous, although a correlation was found between the three locations. Cheng et al. [25] investigated the effect of the inhomogeneous wave environment on the phase 2 floating pontoon bridge concept selected by the NPRA and found that inhomogeneous waves cause relatively larger sway motion and increase the axial force and bending moments, indicating the importance of a proper description of the wave environment on-site.

The increased length and slenderness will also increase the natural periods of the floating bridge structure. Where the existing Bergsøysund Bridge has a first natural period close to 10 s, the corresponding natural period of the phase 2 floating bridge concept will be roughly 55 s. Due to this wider range of natural periods, second order difference frequency wave loads become increasingly important and have to be included in the design. Including a full quadratic wave load transfer function (QTF) to describe the second order effects numerically is very time consuming and usually the Newman's approximation is used as a simplification [26]. Determining whether or not this assumption is valid for a floating bridge structure is important but so far no investigations have been made on the topic. Another effect from the increased slenderness is the risk of global buckling failure due to the varying axial load under dynamic loading.

When designing a floating pontoon bridge with a single continuous pontoon it is possible to simplify the wave-structure interaction as a 2-dimensional problem, which was convenient in the 70s and 80s when computational power was limited. The proposed concepts today, however, are all based on discrete pontoons with varying sizes and spaces between them. The dimensions and the distance between two adjacent pontoons are governing factors when estimating the importance of properly accounting for their hydrodynamic interaction. Xiang [27] investigated the hydrodynamic interaction between two ships and established a simplified formula to estimate when the hydrodynamic interaction becomes important. Later on Xiang et al. [28] investigated the effect of including the hydrodynamic interaction between the pontoons for the Bjørnafjord phase 5 floating pontoon bridge concept in long-crested irregular waves. They found that the sloshing and piston modes of the water between the pontoons had a significant effect on the response amplitude operators (RAOs) and in beam sea the hydrodynamic interaction increased the weak axis bending moments. A sheltering effect was instead present when the wave direction was more aligned with the longitudinal direction of the bridge.

As the previous challenges suggest, the dynamic behaviour of the proposed floating bridge concepts still needs to be investigated further. A common way of testing new concepts is to perform model tests in an ocean basin. However, the length of the proposed concepts are so extreme, that fitting a small scale model into any existing ocean basin facility will violate the

scaling laws required for the experiments to be consistent with the full scale structure. In other words, it is not possible to conduct any standard experimental investigations because no existing lab facility is big enough. One way to avoid this problem is to use a so-called hybrid approach, which has previously been used for offshore structures held in place with tethers down to extreme depths [29]. One such hybrid approach is a truncated system with off-line numerical simulations. This method focuses on a specific part of the structure and verifies a numerical model made in a computer program against experiments. The numerical model is then used to simulate the "true" experimental value of the entire structure. This method requires extensive verification of the numerical model and the accuracy of the performed tests heavily relies on the capabilities of the computer program used.

When questioning the capabilities of existing computer programs that have been verified for various offshore structures, it becomes relevant to assess if the applied numerical methods and theories used in the computer programs are capable of simulating the real wave force and structural response of existing floating bridges. Petersen et al. [30] have looked at this issue by focusing on measurements of the accelerations of the Bergsøysund Bridge and the wave elevation close by. They compared two methods to calculate the wave forces; i) using a comprehensive numerical model of the bridge and the acceleration measurements they were able to calculate the wave forces using inverse methods; and ii) using a frequency domain assessment of the wave forces based on wave elevation measurements. This comparison is possible due to the pronounced linear behaviour of the bridge and that the wave load is the dominant external force in the system. Through the study they concluded, that a reasonable match in the power spectral densities between the two methods was obtained, although some differences were observed.

Discussing the capabilities to properly model the dynamic behaviour, it is important to remember that in situations where the excitation frequency of the stochastic load processes are close to the natural periods of the structure, dynamic amplification occurs. Under such situations, the most important reducing factor for the structural response is the amount of damping present in the system. Damping is the term used when energy is dissipating from the system into its surroundings, such as the case of soil-structure interaction, fluid-structure interaction and passive or active artificial damping devices. Damping also comes from internal energy dissipation produced by the friction between the material particles when they are being displaced due to tension and compression. A better understanding of damping and how to model it along the bridge can help to reduce the loads and optimize the design.

1.2 Objectives and scope

Of the many challenges listed in the previous section, the present thesis focuses on uncertainty assessment of the wave- and current induced response of curved floating bridges with discrete pontoons. With uncertainties in both design wave parameters and the capabilities of commonly used computer programs, it is important to assess the extent of these uncertainties in order to adjust the design of the new and very long floating bridge structures accordingly. The overall aim can be decomposed into the following research objectives:

RO1 Study the effect of wave direction uncertainty on the extreme structural response of a long floating pontoon bridge

RO2 Assess the numerical model uncertainty of commonly used programs in the offshore industry when applied to floating pontoon bridges

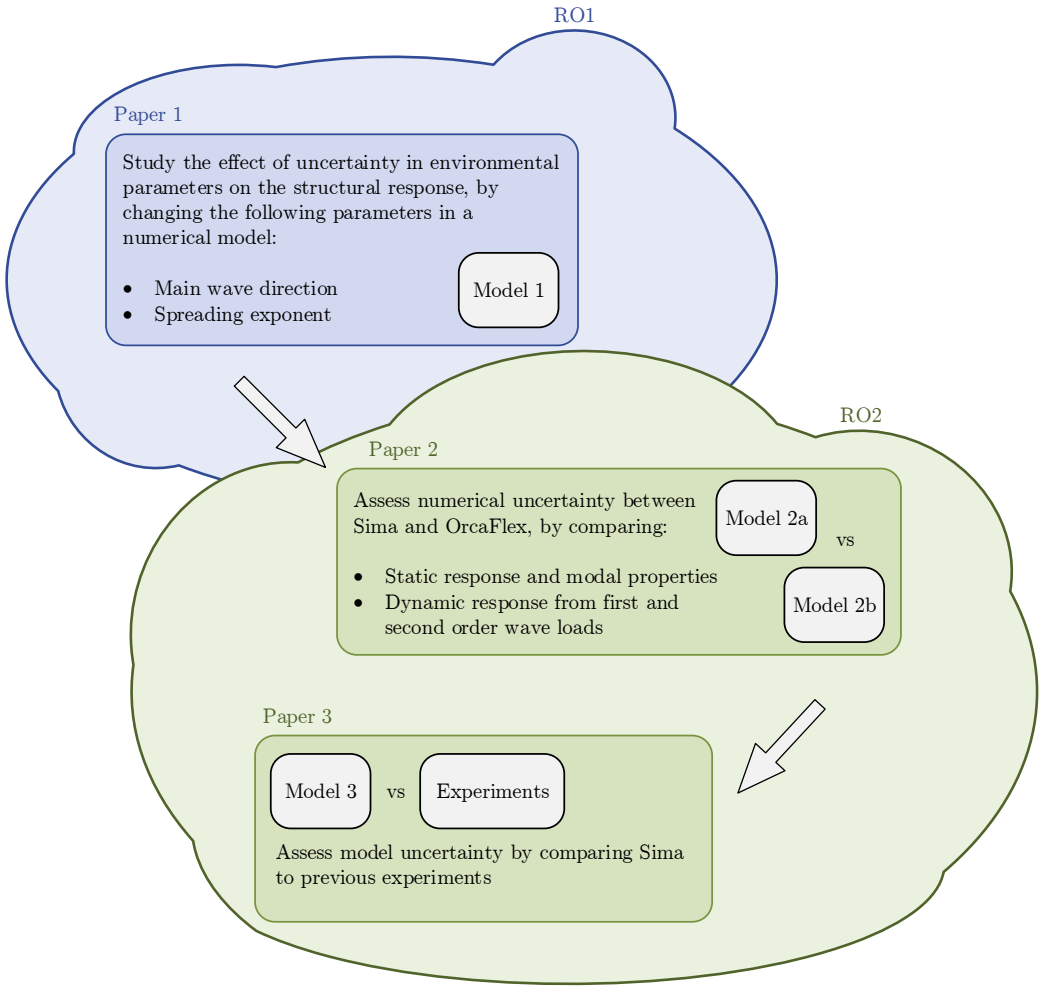

Fig. 2: Scope of the thesis and how the appended papers are related to the research objectives.

The objectives listed above are examined in the three appended papers and an illustrative overview of how the papers are connected to the objectives is shown in Fig. 2.

The first objective RO1 is achieved by performing a parametric study in the computer program Sima [31; 32] (also referred to as Simo-Riflex). The parametric study will focus on the extreme response of a simplified version of the Bjørnafjord phase 2 floating pontoon bridge concept selected by the NPRA, for two changing parameters, i.e. the main wave direction and the spreading exponent. The numerical model made in Sima is from now on referred to as Model 1.

The second objective RO2 is accomplished by comparing the structural response calculated in the two computer programs Sima and OrcaFlex [33], when applied to a complex version of the phase 2 floating pontoon bridge concept. These numerical models are from now on referred to as Model 2a for Sima and Model 2b for OrcaFlex. A further assessment of the numerical uncertainty when using Sima is performed, in reference to RO2, by comparing previous small-

scale experiments for a generic floating bridge, carried out in 1989 by Marintek (now SINTEF Ocean), to a numerical model with equivalent properties. This numerical model is from now on referred to as Model 3.

1.3 Structure of the thesis

The relevant background on methods and theory used in the thesis is covered in chapter 2. This includes a general description of the hydro-elastic coupling in the dynamic calculation using Sima, the practical aspects of creating the numerical models and the relevant background for predicting the short-term extreme response of the bridge.

The first research objective is covered in chapter 3 and is a summary of the first appended paper. The chapter focuses on how wave direction parameters, i.e. main wave direction and spreading exponent, influence the extreme displacement- and Von Mises stress response. The findings are based on a numerical, parametric study.

The second research objective is covered in both chapter 4 and 5 and covers software-to-software comparison of the global response of the same floating pontoon bridge concept (second paper) and an uncertainty assessment and verification against previously performed experiments (third paper), respectively.

A final discussion of the work carried out during the Ph.D. is given in chapter 6 together with concluding remarks, a list of original contributions and ideas of future work needed.

2 | Overview of theories and methods used

The research work, carried out as a part of the present thesis, rests on the shoulders of a substantial body of existing theory, methods and engineering assumptions. A general description of the investigations and corresponding findings was given in chapter 1 from a historical perspective. This chapter attempts to describe in more details the theoretical background for calculation of the dynamic response of floating bridges. It should be noted, however, that the theory related to all aspects of the field requires several books to cover and as a consequence hereof, the following sections are a blend of cherry-picked topics covering the most relevant areas related to the thesis. This involves a brief overview of how the dynamic loads and structural response of the floating bridge is calculated using the computer program Sima, practical aspects of how the numerical models are made, and a description of the method used for estimating the extreme response.

2.1 Predicting floating bridge global response

Estimating the dynamic response of offshore structures has become an increasingly complex task as the need for more and more specialized solutions arise. Standard design of many offshore structures include both wind, waves and current loads with associated non-linear dynamics due to effects such as second order wave loads, aerodynamic loads, etc. In order to conveniently model and analyse many different offshore structures (each with their own complex problems that have to be properly dealt with) a range of general multi-purpose computer programs have been developed. Sima is one of those programs and has been used in the present thesis to successfully model the response of curved floating pontoon bridges.

2.1.1 Overview of the coupled hydro-elastic computer program

In simplified terms, Sima is the graphical user interface used to create a 3-dimensional representation of the numerical model while verifying the consistency of the user-given inputs. Based on the graphical representation, Sima then automatically generates input files for the two underlying programs Simo and Riflex used to model the hydrodynamics and the structural system, respectively. When modelling a floating pontoon bridge both underlying programs are needed for a coupled hydro-elastic solution procedure as illustrated in Fig. 3. Riflex is used to solve the static and dynamic equations and is based on the Finite Element Method (FEM) using the Green strain formulation. It was initially developed for offshore analysis of slender structures such as risers. Simo generates the wave field and calculates the hydrodynamic loads on the pontoons, modelled as large rigid bodies.

The wave elevation and the first and second order wave forces are pre-generated in Simo and for each dynamic time step, the viscous drag loads on the pontoons are computed in Simo

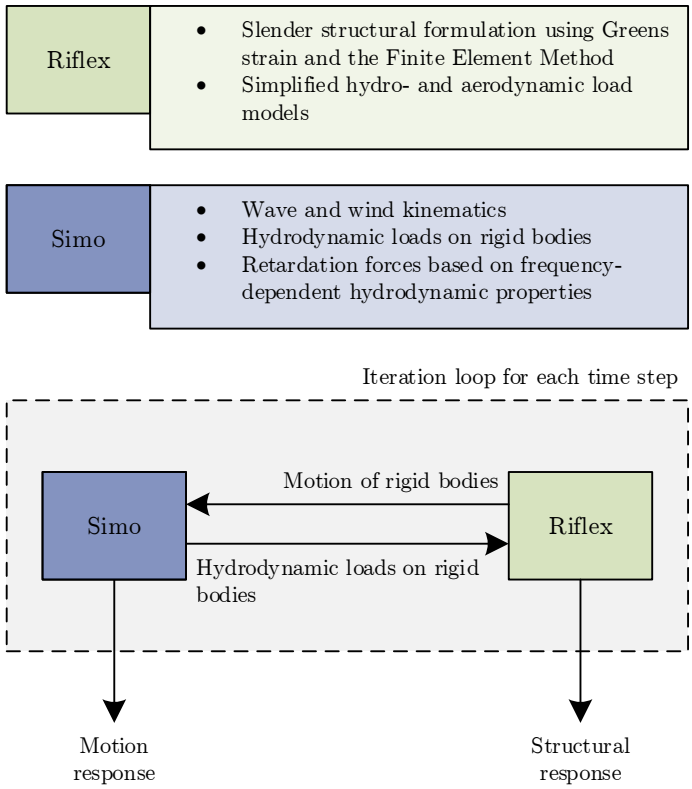

Fig. 3: General overview of the calculation procedure in Sima and the hydro-elastic coupling between Simo and Riflex, when performing a non-linear dynamic analysis, that includes viscous drag forces.

and passed to Riflex where the equation of motion is solved, resulting in a new displacement configuration, which is then sent back to Simo. This iterative loop for each time step is what makes the program able to solve the hydro-elastic problem and is particularly important when including non-linear structural properties or quadratic viscous drag forces in the analysis. This procedure is described in more detail in [34].

2.1.2 Governing dynamic relations and environmental loads

The coupled hydro-elastic calculation procedure is used to solve the hybrid frequency- and time domain formulation expressed by Eq. (1) [31; 35]. On the left hand side of the equation is the excitation force $q_j^{exc}(t)$, which is the sum of all external forces including first order wave force $q_j^{(1)}(t)$, second order wave force $q_j^{(2)}(t)$ and viscous drag force $q_j^{(d)}(t)$ related to the j'th degree of freedom (DOF) as functions of time t, described in Eq. (3), Eq. (6) and Eq. (7), respectively [31].

$$q_j^{exc}(t) = \sum_{k=1}^{6} \underbrace{\left[M_{jk} + A_{jk}^{\infty}\right]\ddot{u}_k(t)}_{\text{Inertia forces}} + \underbrace{D_{jk}\dot{u}_k(t)}_{\text{Damping forces}} + \underbrace{\left[K_{jk} + C_{jk}\right]u_k(t)}_{\text{Elastic forces}} + \int_0^{t_{mem}} \underbrace{k_{jk}(t-\tau)\dot{u}_k(\tau)}_{\text{Retardation forces}} d\tau \quad (1)$$

On the right hand side of the equation is a summation of all the acting elastic-, damping-, retardation- and inertia forces. Each force term is related to the displacement $u_k(t)$, the velocity $\dot{u}_k(t)$ or acceleration $\ddot{u}_k(t)$, respectively. The elastic forces are related to the structural stiffness K_{jk} and the hydrostatic stiffness C_{jk} of the pontoons. The damping forces are related to the structural damping D_{jk} and the retardation forces are related to the retardation function $k_{jk}(t)$. The inertia forces are stemming from the structural mass M_{jk} and the mass at infinite frequency A_{jk}^{∞} taken as the constant frequency-independent part of the added mass of the pontoons. The frequency-dependent part of the added mass $a_{jk}(\omega)$ and the potential damping $b_{jk}(\omega)$ of the pontoons, found using a 3-dimensional diffraction-radiation program, are taken into account by the convolution integral of the retardation function and the time lag τ. The idea behind the convolution integral in Eq. (1) is to separate the velocity into a series of small impulses $\dot{u}_k(t)d\tau$ and using the retardation function as an impulse response function. The combination $k_{jk}(t-\tau)\dot{u}_k(t)d\tau$ is then the response from each step $d\tau$ in time. Accordingly, the integral becomes the sum of the responses from all impulses over the relevant time interval, referred to as the memory time t_{mem}.

The retardation function is defined in Eq. (2) as the inverse Fourier transform of the frequency-dependent hydrodynamic damping based on the Kramers-Krönig relation [31].

$$k_{jk}(t) = \frac{2}{\pi}\int_0^{\infty} b_{jk}(\omega)\cos(\omega t)d\omega \tag{2}$$

Going back to the left hand side of Eq. (1), the first- and second order wave forces are generated based on their representations in the frequency domain. In the case of the first order wave force the simulation is based on the real part $\Re(\cdot)$ of the inverse fast Fourier transform (IFFT) of the unidirectional wave spectrum $S_\zeta(\omega)$, the directional spreading function $D_\zeta(\theta)$ and the first order wave force transfer function $H_j^{(1)}(\omega,\theta)$, where θ is the wave direction ans ω is the angular wave frequency.

$$q_j^{(1)}(t) = \Re\Bigg(\sum_{m=1}^{N_\omega}\sum_{n=1}^{N_\theta}\sqrt{2S_\zeta(\omega_m)D_\zeta(\theta_n)\Delta\omega_m\Delta\theta_n}\left|H_j^{(1)}(\omega_m,\theta_n)\right| \exp\left[i\left(\varepsilon_{nm}+\varphi_{H_{jnm}^{(1)}}+\omega_m t - k_m x\cos(\theta_n) - k_m y\sin(\theta_n)\right)\right]\Bigg) \tag{3}$$

The term i is the imaginary unit, x and y are the spatial coordinates of each pontoon, k_m is the wave number corresponding to the m'th wave frequency, $\varphi_{H_{jnm}^{(1)}}$ is the phase angle of the first order wave transfer function and ε_{nm} is a randomly generated phase angle value. Both $\Delta\omega$ and $\Delta\theta$ refer to frequency and wave direction step sizes, respectively, according to the discretization governed by the number of frequencies N_ω and number of wave directions N_θ.

The directional spreading function is defined in Eq. (4) and is based on the principle of a normalized distribution in order to keep the energy intact over all the chosen wave directions used. Analytically, the normalization is achieved using the Gamma function $\Gamma(\cdot)$ but in a numerical approach only a discrete number of wave directions are used. In this case, the normalization is done by dividing with the sum of the histogram areas, since the directional interval widths can be changing. The directional spreading function is governed by the main wave direction θ_0 and the spreading exponent s.

$$D_\zeta(\theta) = \frac{1}{\sqrt{\pi}} \frac{\Gamma(\frac{s}{2}+1)}{\Gamma(\frac{s}{2}+\frac{1}{2})} \cos^s(\theta-\theta_0), \quad |\theta-\theta_0| \leq \frac{\pi}{2} \tag{4}$$

The unidirectional wave spectrum $S_\zeta(\omega)$ is an idealized representation of the wind driven waves in the frequency domain and has many different mathematical formulations dependent on the physical properties of the wave environment. Depending on the duration and the distance over which the wind is blowing, the generated waves are described as either fully developed, fetch-limited or duration-limited [36]. The JONSWAP [37] wave spectrum defined in Eq. (5) is often used to describe fetch-limited developing sea such as the North Sea west of Norway and is also used in the design of the floating bridge concepts proposed by the NPRA [38].

$$S_\zeta(\omega) = \frac{\alpha g^2}{\omega^5} \exp\left[-\frac{5}{4}\left(\frac{\omega_p}{\omega}\right)^4\right] \gamma^\beta \tag{5}$$

Where,

$$\alpha = \frac{H_s^2 \omega_p^4}{16 g^2 (0.065\gamma^{0.803} + 0.135)}, \qquad \beta = \exp\left[-\frac{1}{2\sigma^2}\left(\frac{\omega}{\omega_p}-1\right)^2\right],$$

$$\sigma = \begin{cases} 0.07 & \text{for} \quad \omega < \omega_p \\ 0.09 & \text{for} \quad \omega > \omega_p \end{cases}$$

Main parameters governing the overall shape of the spectrum in Eq. (5) are the significant wave height H_s, the peak angular frequency ω_p and the peak enhancement factor γ.

The first order wave force only deals with linear theory and is not sufficient to describe observable phenomena such as mean drift and slowly-varying motion of structures with low natural frequencies such as a semi-submersible platform. In this case the motion is excited by mean and slowly-varying forces due to the low potential damping at the low wave frequencies where resonance occurs. The slowly-varying forces are second order difference-frequency effects from the interaction of two regular waves with different frequencies. Each pair of regular waves interact and generates a drift force that varies over time. Based on the perturbation method it is possible to describe the second order effects in mathematical terms by means of QTFs where the second order effects are captured for all combinations of the relevant wave frequency pairs. By applying Newman's approximation, the off-diagonal terms of the QTFs are simplified as functions of the diagonal terms. Based on the simplified QTFs, the second order difference-frequency wave force is defined in Eq. (6).

$$q_j^{(2)}(t) = \Re\Bigg(\sum_{l=1}^{N_\omega} \sum_{m=1}^{N_\omega} \sum_{n=1}^{N_\theta} \sqrt{2S_\zeta(\omega_l) D(\theta_n) \Delta\omega_l \Delta\theta_n} \left| H_j^{(2-)}(\omega_l, \omega_m, \theta_n) \right| \tag{6}$$
$$\sqrt{2S_\zeta(\omega_m) D(\theta_n) \Delta\omega_m \Delta\theta_n} \exp\left[i \left((\omega_l - \omega_m)t + \varepsilon_{nl} + \varepsilon_{nm} + \varphi_{H_{jnlm}^{(2-)}} \right) \right] \Bigg)$$

Here, $H_j^{(2-)}(\omega_l, \omega_m, \theta_n)$ is the simplified QTF and $\varphi_{H_{jnlm}^{(2-)}}$ is the corresponding phase angle. The superscript (2−) is to indicate that the QTF is based on the difference-frequency part.

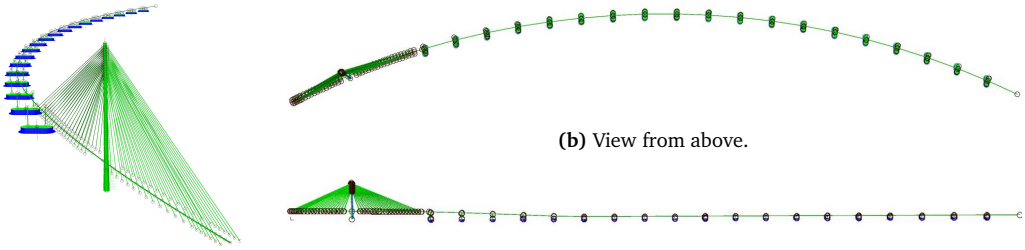

(a) View from South. **(b)** View from above. **(c)** View from East.

Fig. 4: Overview of Model 2a used in the second paper for the Bjørnafjord phase 2 concept. (a) Seen from the South, looking past the tower and stay cables towards the pontoons and connecting columns in the North. (b) Seen from above looking down over the full extension of the bridge girder. (c) Seen from the East, looking towards the West with a view of the high bridge section in the South and the floating bridge section in the North.

The final external force in the dynamic system is the viscous drag force shown in Eq. (7). The description is based on the viscous part of the standard Morison's Equation and includes the water density ρ, the drag coefficient C_j^d, the cross-section A_j and the relative fluid velocity $\dot{u}_r(t)$.

$$q_j^{(d)}(t) = \frac{1}{2}\rho C_j^d A_j \dot{u}_r(t)\,|\dot{u}_r(t)| \tag{7}$$

The viscous force is a function of the relative fluid velocity and for this reason, the dynamic response of the bridge may have a significant effect on the force magnitude as a function of time. Furthermore, it is possible to obtain negative damping forces which will excite the structure even further and hence making it important to include it in the design.

2.1.3 Solving the time domain equation

Based on the coupled hydro-elastic solution procedure illustrated in Fig. 3, the time-dependent motion $u_k(t)$ in Eq. (1) can be found for each time step of the simulation via an incremental procedure using the Newmark-β integration algorithm and equilibrium between all the force terms is obtained for each time step via the Newton-Raphson iteration procedure [32]. Based on the FEM it is possible to compute the internal forces of the structure.

2.2 Practical aspects of the numerical models

Three different numerical models have been developed during the work of the thesis - one for each of the appended papers. Model 1 and Model 3 are relatively similar in their geometry, although Model 1 is more than 5 times longer than Model 3. Model 2a, however, is the most complex of all the models, see Fig. 4, and it will be the one referred to in this section when describing the practical aspects of creating a numerical model. When discussing specific modelling aspects, however, examples from the other models might be used.

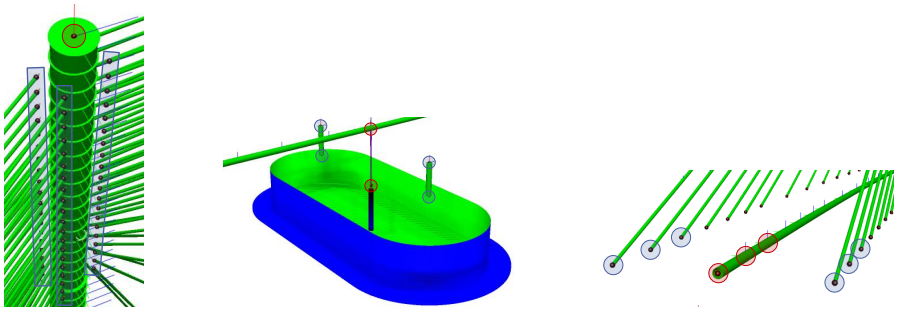

(a) Tower. **(b)** Columns. **(c)** Bridge girder.

Fig. 5: Detailed parts of Model 2a where rigid body connections are specified using master-slave connections marked with red (master node) and blue (slave nodes) colors. (a) A single master node at the top of the tower and 4×20 slave nodes. (b) Two master-slave connections are specified; i) a master node and two slave nodes connect the bridge girder with the top of the two columns; and ii) a master node and two slave nodes connect the pontoon with the bottom of the two columns. (c) A sequence of master nodes in the bridge girder, each with two slave nodes for each pair of connecting stay cable.

2.2.1 Brief description of the Bjørnafjord phase 2 concept

Model 2a illustrated in Fig. 4 is based on the Bjørnafjord phase 2 concept selected by the NPRA, described in detail in [39]. The concept is an approximately 4,600 m long curved floating pontoon bridge with a high bridge section at one end to allow for ship passage. The high bridge section contains a 230 m high tower and 4×20 pre-tensioned stay cables down to the bridge girder 55 m above the mean water level (MWL). After the high bridge section there is a transition into a floating bridge section roughly 15 m above the MWL, connected with pairs of columns to 19 equally distributed pontoons. All the pontoons have a draft of 10.5 m and have the same geometry. At each end, the bridge is fixed in all DOFs and the bridge girder is restricted from transverse motion at the tower, which in turn is fixed in all DOFs at the bottom. Throughout the length of the bridge various cross-sections are used in the bridge girder to optimize the weight-strength ratio.

The pontoons are made up of a rectangle and two half circles in the plan view and are 14.5 m high, 28 m wide and 68 m long. The bottom plate has an additional horizontal extension of 5 m in order to create a 0.6 m thick heave plate, which is commonly referred to as a bilge keel for floating production storage and offloading (FPSO) structures in the offshore oil and gas industry. The purpose of the heave plate is to increase the hydrodynamic added mass of the structure and thereby shift critical natural frequencies outside the main energy frequency interval of the wave spectrum. The draft of the pontoons is kept at 10.5 m for all of them by adding pontoon specific ballast.

2.2.2 Modelling the bridge girder, columns, tower and pre-tensioned stay cables

All the structural parts highlighted in green in Fig. 4, except for the stay-cables, are modelled as linear Euler-Bernoulli beams with St. Vernant torsion and include a linear formulation of the geometric stiffness. The stay-cables are modelled as bar elements and the connections between the tower, the stay cables and the bridge girder are modelled as rigid body connections using master-slave relations between the nodes as illustrated in Fig. 5. The same method is utilized for

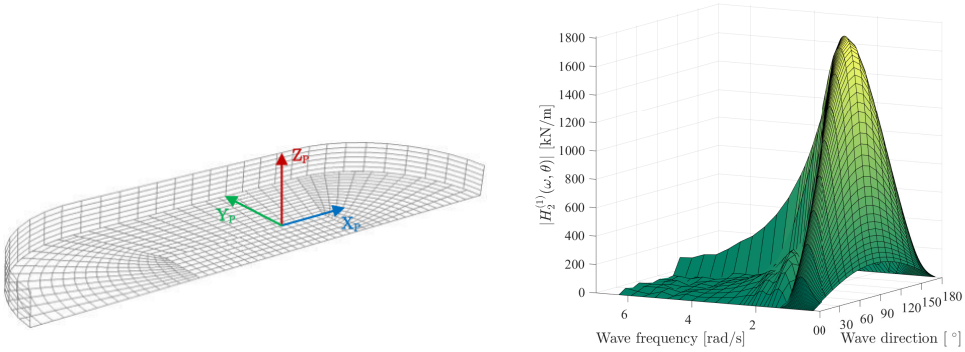

(a) Wadam input. **(b)** Wadam output.

Fig. 6: Wadam input panel model and output wave force transfer function, related to the third paper. (a) Panel model of submerged part of the pontoon. (b) Wave sway force transfer function amplitude.

connecting the columns to the bridge girder and the pontoons. The pre-tension of the cables is modelled by specifying a difference in the stress-free configuration and the final configuration lengths for each cable, equivalent to the force after static equilibrium when pre-tension is not included.

2.2.3 Modelling the hydrodynamic properties of the pontoons

The pontoons are included in the numerical model as rigid Simo bodies attached to Riflex nodes at the MWL. The hydrostatic- and non-viscous hydrodynamic properties of the pontoons are included by importing a result file from the diffraction-radiation program Wadam. This program solves the diffraction- and radiation problems using potential theory and discretely distributed panels, such as the panel model shown in Fig. 6a. A first estimate of the largest accepted panel element size is given as a $1/8$ of the wave length for the shortest wave considered [26] and the final number of panels is found based on a convergence study.

A buoyancy force from the displaced water is manually added to the Simo bodies at the center of buoyancy (COB) to achieve static equilibrium. However, the buoyancy force also contributes to the roll and pitch stiffness terms in the hydrostatic stiffness matrix and is by default included twice due to the coupling between Simo and Riflex. In Simo it is included in the hydrostatic stiffness matrix and in Riflex it is included as a buoyancy force in the COB and due to the distance between the COB and the node, a de-stabilizing moment is added. In order to avoid including the contribution from the buoyancy force to the roll and pitch stiffness twice, the buoyancy terms are removed from the hydrostatic stiffness matrix.

The hydrodynamic added mass and the first order wave force transfer function, see Fig. 6b, are taken directly from the Wadam result file and the retardation functions are calculated inside Simo based on the potential damping. The structural mass matrix is modified to include the ballast in the formulation. The simplified QTFs used to calculate the second order low-frequency force $q_j^{(2)}(t)$ are also taken from the result file.

The viscous forces are included by inserting a vertical Morison element, governed by Eq. (7), at the center of the pontoons from the bottom to the MWL as seen in Fig. 5b. In cases with a

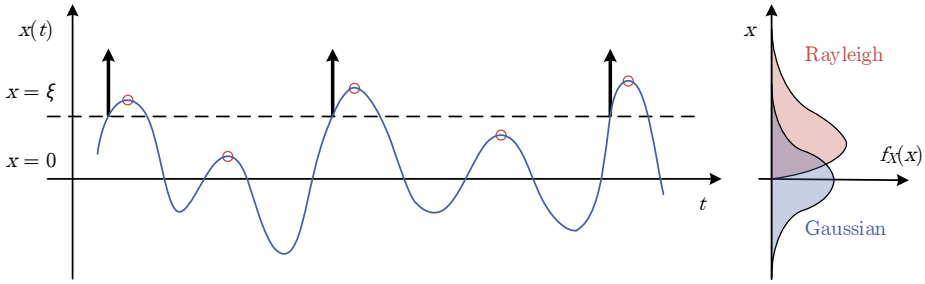

Fig. 7: Realization of a stationary, Gaussian, narrow-banded process (blue line), the individual maxima (red circles) and arrows indicating positive ξ-level upcrossings. On the right-hand side are the Gaussian and Rayleigh probability density functions for the instantaneous values and individual positive maxima, respectively.

heave plate at the bottom of the pontoons, two Morison elements are used. One 0.6 m long element over the height of the heave plate and a 9.9 m long element over the other part of the pontoon height.

2.3 Extreme response prediction

Extreme response prediction of a structural system is dependent on the characteristics of the stochastic load and whether the structural system is linear or non-linear. With only first order Gaussian waves acting on a linear structural system, the structural response can be considered Gaussian in nature with the individual maxima of the time series following a Rice distribution (Rayleigh distribution for narrow-banded processes). The statistical properties of the extreme response from several statistically independent realizations will converge towards that of a Gumbel distribution.

In the first paper, dealing with the effect of wave direction parameters on the extreme response of a floating pontoon bridge, the system behaves linearly and the aforementioned statistical relations are for that reason valid. In the two other papers, non-linear effects such as viscous drag are included and the system is found to be non-linear.

This section gives a brief description of how extreme response is defined and, based on a linear structural system, how the statistical properties of the extreme response are established. Most of the information in this section is based on Fu [40], Naess and Moan [41], Sødahl [42] and Ochi [43].

2.3.1 Statistics of a stationary and narrow-banded Gaussian process

A realization of a narrow-banded Gaussian process is illustrated in Fig. 7 with individual positive maxima x_m and the corresponding Gaussian- and Rayleigh probability density functions (PDFs). The largest maximum for a given duration is referred to as the extreme response. Illustrated in Fig. 7 are the ξ-level upcrossings, which occur when the time-derivative of the realization $\dot{x}(t) > 0$ at $x = \xi$. For a general stochastic process, several individual maxima can occur between each zero-upcrossing and they can be both positive and negative. Instead, for a narrow-banded stochastic processes only a single positive maximum exists between two adjacent zero-upcrossings.

By only assuming the stochastic process to be stationary, the ξ-level upcrossing frequency is defined as in Eq. (8) where $f_{X\dot{X}}(x,\dot{x})$ is the joint PDF of the random variable X and the corresponding time derivative $\dot{X}$.

$$\nu_+(\xi) = \int_0^\infty \dot{x} f_{X\dot{X}}(\xi,\dot{x}) d\dot{x} \qquad \text{(assumed stationary)} \tag{8}$$

By further assuming that the stationary stochastic process is Gaussian with $E[x(t)] = 0$, it then follows that $\dot{X}$ is also Gaussian with $E[\dot{x}(t)] = 0$ and consequently, $E[x(t)\dot{x}(t)] = 0$. This means, that the two random Gaussian variables X and $\dot{X}$ are statistically independent and $f_{X\dot{X}}(x,\dot{x}) = f_X(x) f_{\dot{X}}(\dot{x})$. By inserting the mathematical description of a Gaussian PDFs together with the definition of a joint PDF for two statistically independent random variables, Eq. (8) becomes

$$\nu_+(\xi) = \frac{1}{2\pi}\frac{\sigma_{\dot{x}}}{\sigma_x}\exp\left[-\frac{1}{2}\frac{\xi^2}{\sigma_x^2}\right] \qquad \text{(assumed stationary and Gaussian)} \tag{9}$$

where σ_x and $\sigma_{\dot{x}}$ are the standard deviations of the two random variables. For a narrow-banded Gaussian process the expected frequency of all individual maxima above $x = \xi$ are equal to the ξ-level upcrossing frequency $\nu_+(\xi)$. The probability $P\{X_m \geq \xi\}$ of the individual maxima to exceed $x = \xi$ then becomes the ratio between the number of individual maxima $\nu_+(\xi)(t_2 - t_1)$ above the defined level and all individual maxima $\nu_+(\xi = 0)(t_2 - t_1)$ above zero during a specific time period $t_2 - t_1$. From this relationship, the cumulative distribution function (CDF) can be found as $F_{X_m}(\xi) = 1 - P\{X_m \geq \xi\}$, which leads to the PDF shown in Eq. (10), termed the Rayleigh distribution.

$$f_{X_m}(x) = \frac{x}{\sigma_x^2}\exp\left[-\frac{1}{2}\frac{x^2}{\sigma_x^2}\right], \qquad \text{for } \xi \geq 0 \tag{10}$$

2.3.2 Extreme value statistics

The extreme value is the largest value of an ordered sample of individual maxima, as defined in Eq. (11).

$$x_e = \max\{x_{m_1}, x_{m_2}, ..., x_{m_N}\} \tag{11}$$

Assuming that the individual maxima are statistically independent and identically distributed with the CDF $F_{X_m}(x)$, the link between the CDF of the individual maxima and the extreme response X_e can be described as in Eq. (12), where N is the number of individual maxima in the sample. The assumption of the individual maxima being statistically independent is not always permissible, since waves come in groups of large waves. Furthermore, for lightly damped structures, the individual maxima are likely to arrive in groups, which leads to a conservative estimate on the extreme response [41].

$$F_{X_e}(x) = P\{X_e \leq x\} = \left[F_{X_m}(x)\right]^N, \qquad \text{for statistically independent } x_m \tag{12}$$

For $N \to \infty$, this extreme distribution CDF converges to either the Gumbel, Weibull or Frechet distribution [43], which are all regarded as special cases of the Generalized Extreme Value (GEV) distribution [44]. For marine structures the most commonly used distribution is the Gumbel distribution [41], which is often referred to as the type I asymptotic form of Eq. (12) [45].

2.3.3 Relevant methods to obtain extreme response

Different methods exist for prediction of the extreme response, e.g. the Block Maximum method, the Average Conditional Exceedance Rate (ACER) method and the moment-based Hermite method. Extreme value estimation based on an individual maxima distribution is another much applied method and when used in conjunction with a Weibull distribution and the special tail fitting method, a closer fit to the upper tail is achieved [42]. The Block Maximum method divides the response time series into individual blocks of a specified time frame and extracts the extreme response from each block. The extreme response is the largest of the individual maxima as formulated in Eq. (11) and the CDF of the extreme response hence follows Eq. (12) with the same asymptotic behaviour. It is often assumed within the design of typical offshore structures, that the extreme response follows the asymptotic Gumbel distribution, but it is not possible within classical extreme value theory to validate if this assumption is actually true [41]. The ACER method is based on a general formulation of the mean upcrossing frequency at the upper tail of the PDF. The method thereby avoids the common assumption that the extreme values follow an asymptotic extreme value distribution [41]. By basing the estimation of the extreme value on average conditional exceedance rates, hence the name of the method, it is possible to account for the correlation between adjacent maxima in the method. All clumps of exceedances are thereby separated by at least $k-1$ nonexceedances. As k increases, the method becomes more accurate but is based on less data. The moment based Hermite method is used for non-Gaussian processes by translating the non-Gaussian process into a Gaussian process and applies the standard Gaussian theory. The name of the method comes from the Hermite polynomial series expansion used when translating the non-Gaussian process into a Gaussian one.

In cases where the individual maxima distribution has an exponentially decaying tail, the extreme distribution will converge towards a Gumbel distribution. The Exponential-, Weibull-, Gaussian-, Rayleigh- and Log-Normal distributions all have exponentially decaying tails and if they are fitted to individual maxima, then the corresponding extreme distribution becomes a Gumbel distribution. The 3-parameter Weibull distribution is often utilized for this approach.

2.3.4 Extreme value estimation based on a Weibull initial maxima distribution

The Weibull distribution given in Eq. (13) is often used to fit to samples of individual maxima. The Weibull distribution is defined by the location parameter δ, the scaling factor λ and the shape factor υ. The Rayleigh and Exponential distributions are special cases of the Weibull distribution by selecting specific values of the shape factor (i.e. 2 for the Rayleigh and 1 for the Exponential distributions).

$$F_{X_m}^{W}(x) = 1 - \exp\left[-\left(\frac{x-\delta}{\lambda}\right)^{\upsilon}\right] \tag{13}$$

Based on the relationship between the Weibull distribution for individual maxima and the Gumbel distribution for extreme values, the extrapolated average extreme value μ_{X_e} can be determined based on Eq. (14) from the fitted Weibull parameters in Eq. (13) [42].

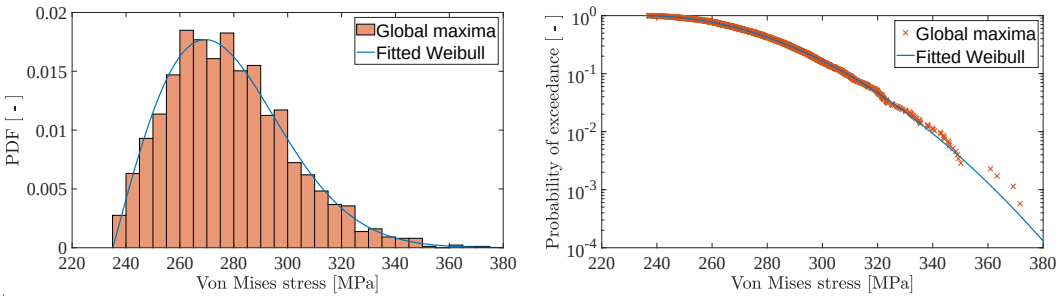

Fig. 8: Fit of Weibull distribution to global maxima of Von Mises stress time series with a threshold equal to the mean value.

$$\mu_{X_e}^W = \delta + \lambda\left[\ln(N_m)^{\frac{1}{\upsilon}} + \frac{0.57722}{\upsilon}\ln(N_m)^{\frac{1-\upsilon}{\upsilon}}\right] \tag{14}$$

Where N_m is the number of local maxima during the time interval under consideration.

2.3.5 Procedure in first paper when estimating extreme response

The extreme response investigated in the first paper is estimated using a short-term method according to recommendations given by Spidsøe and Karunakaran [46]. For a single realization of the response a Weibull distribution is fitted to the global maxima as recommended by Farnes and Moan [47] using the method of matching statistical moments. In order to predict the extreme response from extrapolation of the Weibull distribution, a good fit to the global maxima (the largest individual maximum within two upcrossings) in the upper tail is necessary. This is generally achieved using a threshold ξ-level to avoid over representation of small maxima in the fitting procedure. The threshold is an empirical value and as pointed out by Fu et al. [48] can have a significant effect on the shape of the Weibull distribution. In the first paper a good fit between the global maxima and the Weibull distribution is obtained by using a threshold of $\xi = 0$ (mean value) as illustrated in Fig. 8. The extrapolated average extreme value μ_{X_e} is calculated using Eq. (14).

3 | Effect of wave direction uncertainty

This chapter is a summary of the content of the first appended paper and deals with the effect on the average short-term extreme response of a simplified version of the Bjørnafjord phase 2 floating pontoon bridge concept selected by the NPRA when changing the main wave direction and the spreading exponent for short-crested waves.

With the relatively large uncertainties related to estimation of the correct wave parameters described in the introduction, it is important to quantify the effect of these parameters on the response of a floating bridge structure. Previous studies on the response of floating bridges have been made, see e.g. [17–19], focusing on the bending moments and pre-tension force in the bridge cross-section. They found that the peak period of the wave spectrum and the correlation between the bending moments to be important parameters in the design. Langen and Sigbjörnsson [49] applied a directional wave spectrum in the analysis of a floating pontoon bridge and found that using long-crested waves would lead to an unreasonably conservative design. Instead, short-crested waves should be applied and they found a low sensitivity in the response towards changes in the spreading exponent within naturally occurring values. Later on, Villoria [50] found the spreading exponent and the wave spectrum shape to have a low influence on the response of a floating pontoon bridge, whereas the peak period and the main wave direction were more important.

The above mentioned studies were conducted for short floating bridges with lengths of less than 1,500 m, whereas the new floating bridge concepts selected by the NPRA have lengths of up to 5,000 m. For the new floating bridge concepts, the extended length increases the slenderness and introduces several extra natural frequencies with corresponding modeshapes that are important in the design. The previous findings are for this reason not neccesarily valid for the new and longer bridge concepts. With the additional uncertainty in the metocean databases discussed in chapter 1, a comprehensive screening of several different wave environments is required before the final design condition can be obtained for each geographical location. Understanding the sensitivity in the response of long floating bridges towards different wave parameters will help decrease uncertainty in the design.

The extreme response of floating bridges has been investigated by e.g. Giske et al. [51] and Øiseth et al. [52] using different methods. Giske et al. compared a new Inverse Second Order Reliability Method (ISORM) described in [53] with the full long-term extreme method and found a close match. Øiseth et al. compared the ACER method described in [54] to the Gumbel short-term extreme method and found the former to have less uncertainty in the estimates when applied to a linear floating pontoon bridge system.

To the knowledge of the authors, all previous studies on the sensitivity of the extreme response towards wave direction parameters, have either been conducted in the frequency domain or based

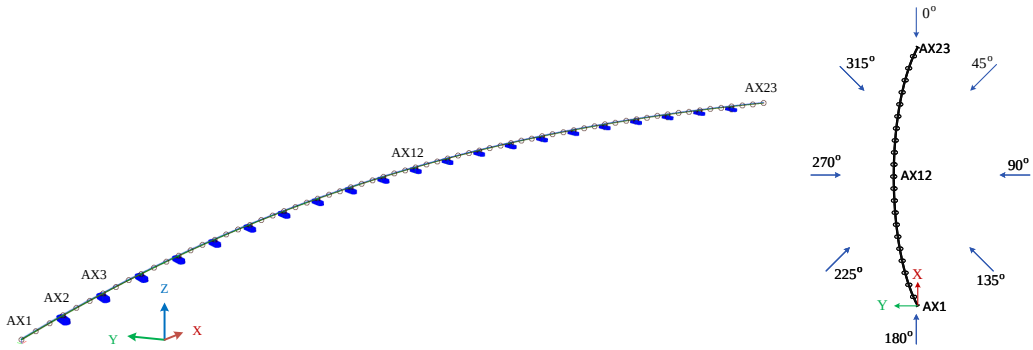

(a) Bridge layout. **(b)** Wave directions.

Fig. 9: Model 1 used in the first appended paper. (a) Bridge layout. (b) Overview of wave directions.

on a limited number of short time domain simulations. This study is the first time a numerical parametric study is based on a large amount of time domain simulations for each changed parameter and will help solidify the understanding of their effect on the extreme response of long floating bridges. As part of the extensive time domain calculations the dependency of the accuracy in the short-term extreme prediction towards the simulation length and the number of realizations has been investigated for the general floating bridge structure to be used as a reference for future investigations of the extreme response.

The following sections describe the floating bridge concept used in the study, the method used for calculating the Von Mises stress in the bridge girder cross-section, the choice of ranges in the wave parameters and the most important findings.

3.1 Bridge concept and methodology

3.1.1 Description of the bridge concept and choice of load cases

The bridge concept used is a simplification of the Bjørnafjord phase 2 concept selected by the NPRA, and is described in [39]. By keeping the bridge girder at the same heigh for the entire length of the bridge and by replacing the tower and stay-cables at the south end with extra pontoons with identical spans between them, the final numerical model is illustrated in Fig. 9. The bridge is roughly 4,360 m long and has a horizontal curvature of 5,000 m. The bridge girder is simplified as a single equivalent beam and is connected to 21 identical pontoons using two vertical columns at each connection. The span between each pontoon is 197 m. The wave direction follows the global coordinate system in Fig. 9 with waves from the 90° direction following the positive Y-axis and waves from the 0° direction following the positive X-direction.

A 100-year wave environment is used in the study based on the environmental conditions at the Bjørnafjord site described in [39] and used as the base case for all 12 load cases investigated, see Tab. 1. The governing parameters for the 100-year JONSWAP wave spectrum is $H_s = 3.0$ m, $T_p = 6.0$ s and $\gamma = 3.3$. Since the time of the study, the metocean report [38] has been updated with slightly reduced T_p and H_s values, a spreading exponent between 4 and 6, and γ between 1.8 and 2.3. These changes are however not thought to have a big impact on the findings in the first appended paper. The 12 load cases are chosen in order to estimate the effect of uncertainties

Tab. 1: Load cases used in the parametric study. First order wave loads are applied with the chosen JONSWAP parameters $H_s = 3.0$ m, $T_p = 6.0$ s and $\gamma = 3.3$ based on the wave conditions at the Bjørnafjord for a 100-year return period [39].

Load Case	Spreading	Wave Direction	Load Case	Spreading	Wave Direction
LC1.1	2	90°	LC2.1	10	90°
LC1.2	2	95°	LC2.2	10	95°
LC1.3	2	100°	LC2.3	10	100°
LC1.4	2	105°	LC2.4	10	105°
LC1.5	2	120°	LC2.5	10	120°
LC1.6	2	150°	LC2.6	10	150°

in the main wave direction close to beam sea, and the effect of uncertainties in the spreading exponent within naturally occurring values.

3.1.2 Method for estimating the extreme Von Mises stress response

The Von Mises stress is calculated manually in the post-processing of the numerical calculations using Eq. (15) based on the internal forces in the equivalent single beam cross-section. The Von Mises stress is calculated for six critical points located in the twin-box cross-section of the bridge girder based on the assumed stress distribution illustrated in Fig. 10.

$$\sigma_v(t) = \sqrt{\sigma_{xx}^2(t) + 3\left(\tau_{xx}(t) \pm \tau_{xy}(t) \pm \tau_{xz}(t)\right)^2} \tag{15}$$

The ± sign in front of the shear stresses in Eq. (15) indicates that the shear stresses are either contributing positively or negatively to the Von Mises stress at the six different points, depending on the shear flow illustrated in Fig. 10.

The extreme response is found by fitting a Weibull distribution to the global maxima of the Von Mises stress response time series at specific points in the cross-section along the bridge. With the fitted Weibull parameters, the extrapolated extreme μ_{X_e} value is found using Eq. (14). Simulating N_r statistically independent realizations, the average extrapolated extreme $\overline{\mu_{X_e}}$, the standard deviation of the extrapolated extreme $\overline{\sigma_{X_e}}$ and the corresponding coefficient of variation (c.o.v.) C_{X_e} are found using Eq. (16), Eq. (17) and Eq. (18), respectively.

$$\overline{\mu_{X_e}} = \frac{1}{N_r}\sum_{i=1}^{N_r}\left(\mu_{X_e}\right)_i \tag{16}$$

$$\overline{\sigma_{X_e}} = \sqrt{\frac{1}{N_r - 1}\sum_{i=1}^{N_r}\left((\mu_{X_e})_i - \overline{\mu_{X_e}}\right)^2} \tag{17}$$

$$C_{X_e} = \frac{\overline{\sigma_{X_e}}}{\overline{\mu_{X_e}}} \tag{18}$$

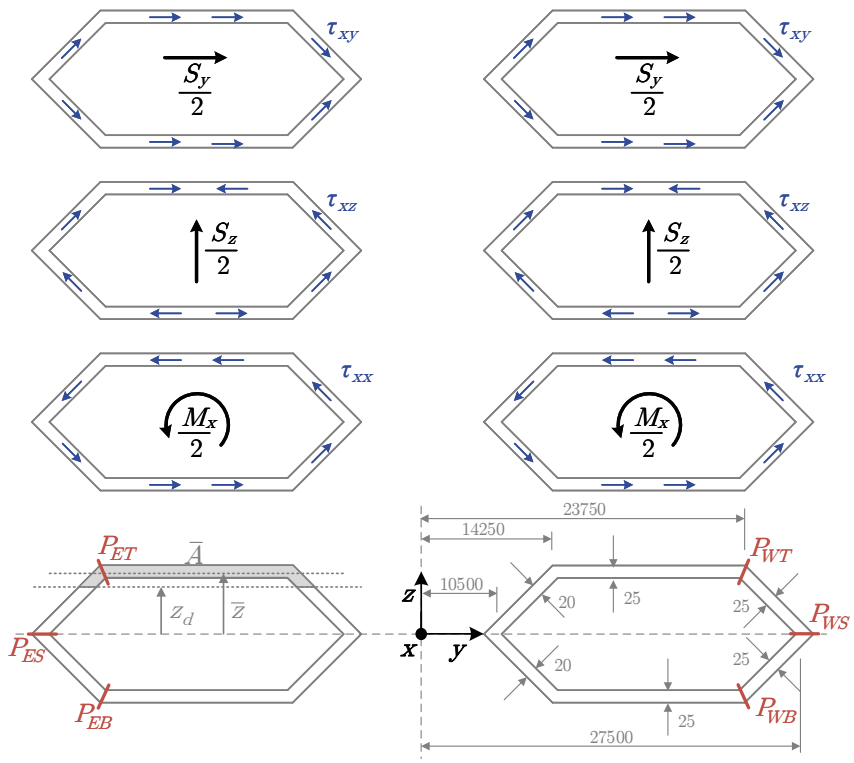

Fig. 10: Bridge girder twin-box cross-section with critical points and assumed stress distribution for calculating cross-sectional stresses. All measurements are in mm.

3.2 Important findings

3.2.1 Reference for choice of number of realizations and realization length

The largest average extrapolated extreme Von Mises stress found among all load cases are located at AX23, see Fig. 9, along the bridge at point P_{ET}, see Fig. 10, in the bridge girder cross-section. The number of realizations needed in order to gain an accurate estimate on the extreme response is found based on a convergence study of the c.o.v. in Eq. (18). By simulating three sets of 100 statistically independent realizations, each with a different realization length, the choice of the suitable number of realizations and the length of the simulations can be decided upon. Fig. 11 shows a comparison of 100 realizations with realization lengths of 1h, 2h and 3h. Based on this figure and a target accuracy of 2% in the c.o.v., 40 realizations with a realization length of 3h are found to be required.

3.2.2 Effect on extreme response for changing main wave direction and spreading exponent

Based on 40 statistically independent realizations, the average extrapolated extreme Von Mises stress at AX23 along the bridge at point P_{ET} in the bridge girder cross-section is found for all 12 load cases. Fig. 12 illustrates the changes in the average extrapolated extreme value and two

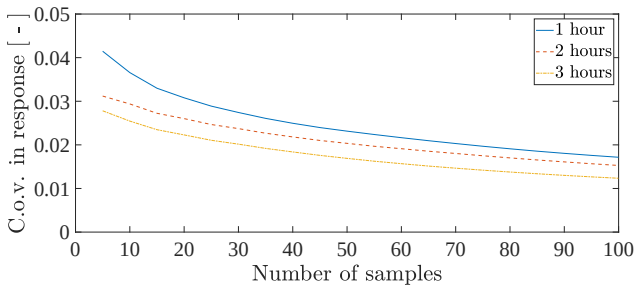

Fig. 11: Coefficient of variation (c.o.v.) of average extrapolated extremes versus simulation lengths and number of samples for Von Mises stress at point P_{ET} at AX23 for LC1.1.

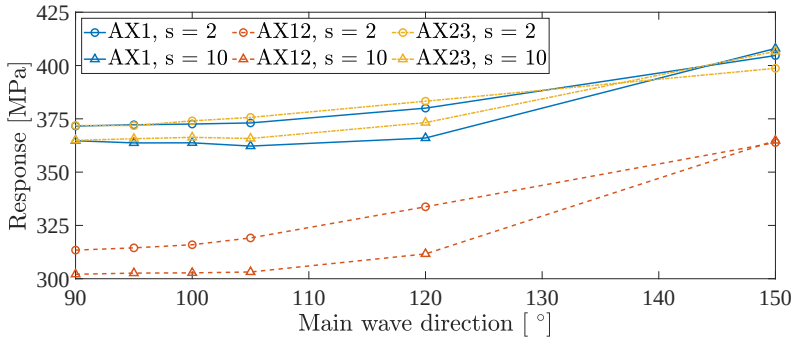

Fig. 12: Sensitivity in the average extrapolated extreme Von Mises stress in point P_{ET} towards the main wave direction and the spreading exponent.

conclusions can be made; i) a low sensitivity towards the spreading exponent is observed in the average extrapolated extreme Von Mises stress of the bridge girder; and ii) due to structural symmetry, the effect of changes in the main wave direction are insignificant for directions within 15° from beam sea.

A similar behaviour is observed in the average extreme transverse and vertical response spectra. No significant effect is observed for main wave directions within 15° from beam sea, although significant changes are present outside this range. Spatial resonance, described by Remseth et al. [55], is thought to be the main cause for this behaviour.

4 | Assessment of numerical uncertainty

This chapter is a summary of the content of the second paper and deals with software-to-software comparison of global response of the Bjørnafjord phase 2 floating bridge concept selected by the NPRA.

Today there are various commercial software available for general multi-purpose offshore structural analysis - many of which are based on the general theory and assumptions within the field and are not tailored towards the specific requirements when applied to a floating bridge structure. For this reason it is worth investigating how well current available computer programs perform. A better understanding of the uncertainties in the numerical tools available is important for the design - including the structural reliability. This chapter investigates this topic by comparing two commonly known computer programs within the offshore industry, i.e. Sima and OrcaFlex.

4.1 The bridge concept and methodology

4.1.1 The Bjørnafjord phase 2 floating bridge concept

In the second paper a detailed version of the phase 2 floating bridge concept at the Bjørnafjord is used. The structural properties follow the description in [39] with only minor simplifications. The simplifications are justified by the aim of the paper being to compare two numerical models that are close to identical. An overview of Model 2a made in Sima is shown in Fig. 4 and associated modelling details are shown in Fig. 5. The wave directions follow the same notation as shown in Fig. 9b. Section 2.2.1 gives a general description of the bridge concept and for that reason the content is not replicated here. Instead, focus is directed towards the numerical models, their differences and the method used for the software-to-software comparison.

4.1.2 Modelling differences

Although the two computer programs utilize the same general theory and assumptions, they have a few different options for the user-given inputs and for how some of the properties are specified in the numerical models. Some modelling differences worth mentioning are:

Short-crested waves are by default in both OrcaFlex and Sima included by specifying a unidirectional wave spectrum, a main wave direction, spreading exponent and the number of wave directions to be applied in the analysis. However, the default methods used for distributing the specified number of wave directions is different. In Sima the wave directions are

distributed linearly, whereas in OrcaFlex they are distributed according to the principle of equal energy. In order to obtain the exact same directional distribution, an exact copy of the directional wave spectrum in OrcaFlex has to be calculated and manually given in Sima.

Radius of gyration of the cross-sections is specified in Sima as a continuous property by writing the radius of gyration per meter for each cross-section. In OrcaFlex the property is indirectly specified by adding 6 DOF Buoys with mass properties to specific points along each line. This is a lumped method and based on a convergence study a distance of roughly 10 m is used between each 6 DOF Buoy.

Ballast is added to each individual pontoon in OrcaFlex by use of 6 DOF Buoys with the specified mass and relative location. In Sima the ballast is, instead, added manually by modifying the structural mass matrix of each individual pontoon.

Buoyancy is added to the pontoons in OrcaFlex by specifying the location of the COB and the displaced volume equivalent to the buoyancy force. In Sima the procedure for adding the buoyancy is a little more complex and due to the coupling between Simo and Riflex care must be exercised not to add the buoyancy force twice. In Riflex the buoyancy force is added by specifying a force in the COB, whereas in Simo the buoyancy force is included via the stiffness matrix. Since the buoyancy force is already accounted for in Riflex, the buoyancy terms are removed from the elements in the stiffness matrix related to roll and pitch.

Of the above mentioned differences, the one regarding short-crested waves proved to be particularly difficult to spot when doing the software-to-software comparison.

4.1.3 A step-by-step comparison method

The two computer programs have been used to model the Bjørnafjord phase 2 floating bridge concept and in order to properly compare the two numerical models, a step-wise approach has been used focusing on the static response and modal properties first and then continuing to response from regular waves shown as response amplitude operators (RAOs). Only then are stochastic response compared for the simplest case of long-crested first order irregular wave loads. From this step additional load complexity is added following two different paths; i) change to first order short-crested wave loads and later including viscous damping loads at the pontoons; and ii) add second order low-frequency wave loads and later include viscous effects at the pontoons. An overview of the stochastic load cases compared is seen in Tab. 2. The two different paths specified for the comparison of the stochastic response are chosen in order to separate second order wave load effects from the general comparison. There are two reasons; i) standard deviations of the structural response show larger variations when second order wave loads are incorporated in the analysis; and ii) the Newman approximation used for the second order wave loads is not validated for this type of structure in short-crested waves.

Tab. 2: Load cases with irregular waves used in the second paper with a main wave direction of 270° and JONSWAP parameters $H_s = 2.4$ m, $T_p = 5.9$ s and $\gamma = 2.0$. The 11 short-crested wave directions in the directional spreading function are distributed according to the default of each program in LC2a and by manually specifying the exact same directions in Sima as in OrcaFlex in LC2b and LC3.

Load Case	Waves Loads	Viscous Effects	Spreading
LC1	first order	No	-
LC2a	first order	No	4
LC2b	first order	No	4
LC3	first order	Yes	4
LC4	first and second order	No	-
LC5	first and second order	Yes	-

4.2 Important findings

4.2.1 Natural periods and modeshapes

The natural periods found in the two computer programs using the added mass at infinite frequency in the solution procedure are denoted T_n and listed in Tab. 3. The differences between the natural periods are within 5% and in most cases close to 1%. However, the corresponding modeshapes show fundamental differences for mode 6 and upwards and is thought to be the main reason for the differences found in the RAOs and the stochastic responses. The most noticeable differences in the modeshapes are for torsional motion.

4.2.2 Response amplitude operators

The regular wave responses are shown in Fig. 13 as RAOs for the vertical displacement z, the weak axis bending moment M_y and the strong axis bending moment M_z. As it can be seen, there is a shift in the peaks corresponding to the natural periods of each numerical model. To obtain similar results in the time-domain it is imperative to have the same modal properties of the structure. Even for slight differences, as in our case, the final comparison is affected. One reason for this is the strong directional sensitivity in the structural response, which has previously been confirmed for a curved submerged floating tube bridge (SFTB) by Leira and Remseth [56].

4.2.3 Attention to modelling details for short-crested waves

Modelling the short-crested waves is a straight-forward process within each computer program but extreme care must be taken when the numerical models have to be exactly the same. It was found that the absolute differences in the standard deviations of the weak axis bending moment along the bridge girder was on average 27% when using the default option in both computer programs. Instead this value was only 7% when the directional wave spectrum used in OrcaFlex was manually copied into Sima as is seen from LC2a and LC2b in Fig. 14. The absolute difference in the standard deviation of the response from the two computer programs is based on the numerical value of the difference - without regard to the sign.

Tab. 3: Natural periods of the floating bridge models. The notation T_n indicates the use of added mass at infinite frequency when solving the standard eigenvalue problem. The notations T_n^a and T_n^b indicate the use of a manual iterative and graphical procedure to include the exact added mass, respectively. The symbols for the primary (secondary) motions in the modeshape are H for horizontal, V for vertical, T for torsional and P for pendulum. Pendulum motion is the motion of the pontoons going from side to side in the longitudinal direction of the bridge like a pendulum.

Mode	Sima			OrcaFlex			Diff.
n	T_n	T_n^a	Modeshape	T_n	T_n^b	Modeshape	T_n
[-]	[s]	[s]	motion	[s]	[s]	motion	[%]
1	50.79	55.63	H	51.81	54.15	H	2.0
2	29.28	31.63	H	29.79	30.64	H	1.7
3	22.55	24.41	H (T)	21.76	22.79	H (T)	3.8
4	17.56	19.28	H (T)	17.52	18.53	H (T)	0.2
5	13.56	14.91	H (T,V)	13.59	14.66	H (T)	0.1
6	12.67	13.06	T (H,V)	12.08	12.26	H (T)	4.9
7	12.15	12.31	V (T)	11.67	11.71	H (V)	4.1
8	11.44	11.29	T (V)	11.39	11.53	V (H)	0.5
9	11.39	11.27	V	11.37	11.34	V (H,T)	0.2
10	11.39	11.09	V	11.36	11.16	V (H,T)	0.2
17	10.69	9.96	V (P)	10.61	-	V (P,H)	0.8
24	8.91	9.24	V (P)	8.81	-	V (T,P)	1.1
28	8.13	8.02	T (H)	7.97	-	V (H,P)	2.0

4.2.4 Comparison of response from second order wave loads

For comparison purposes, the second order wave loads are simplified using the Newman approximation in both computer programs and only used for long-crested waves. It should be stressed that, at the Bjørnafjord location, the second order effects and short-crested waves are expected to act simultaneously. Hence the calculated structural response from second order wave loads should only be used to compare the two computer programs and does not give any information on the expected behaviour of any future bridge with similar design. With this in mind, the response from second order difference-frequency wave loads is showing very similar behaviour in both Sima and OrcaFlex with the peaks corresponding to the natural periods in Tab. 3 within 10%. On average the absolute difference in the response standard deviations from the two computer programs are within 10-15% from each other when adding second order wave loads as illustrated in Fig. 14.

4.2.5 Comparison of viscous damping effects

The viscous effects are included for two separate scenarios: i) for short-crested first order wave loads and ii) for long-crested irregular first and second order wave loads. Due to the exclusion of second order wave loads and the fact that the applied vertical drag coefficients are larger

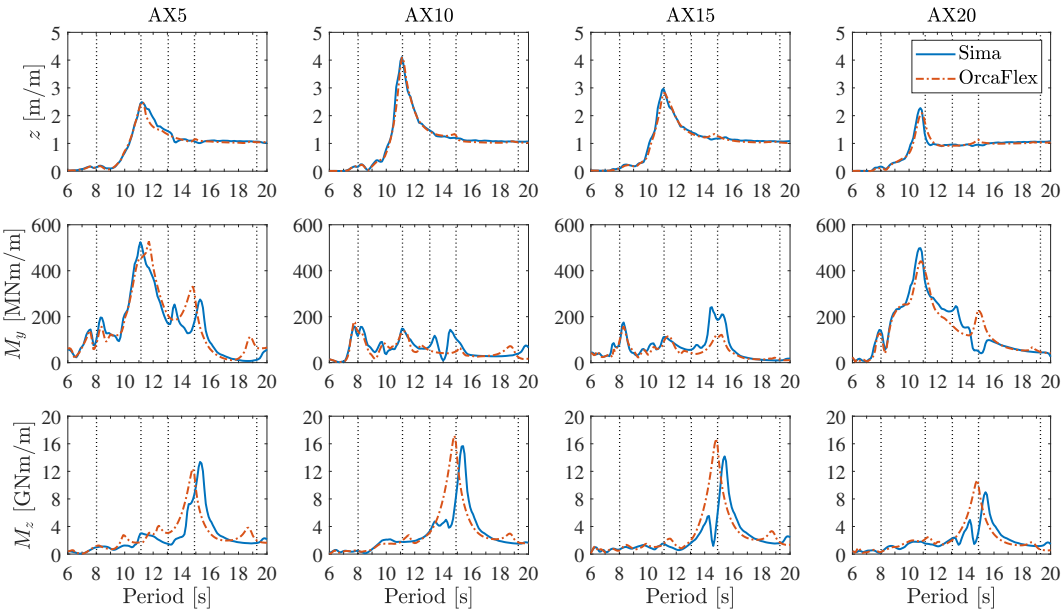

Fig. 13: RAOs at 270° waves for vertical displacement, weak axis bending moment and strong axis bending moment at axis AX5, AX10, AX15 and AX20 along the bridge (see the second appended paper for notation). The natural periods T_n^a based on the iterative method in Sima are shown as the vertical dotted lines for mode 4, 5, 6, 10 and 28 from right to left.

than the horizontal counterparts, the effect from the viscous drag is seen most clearly in the vertical displacement along the bridge with an average reduction of roughly 8%. For the case with unidirectional first and second order waves the effect is mainly seen in the horizontal response with a reduction in OrcaFlex of 20% for the horizontal motion and 14% for the effective tension T_e. The corresponding values are roughly 7-10% larger in Sima.

4.2.6 Final concluding remarks

From the extensive software-to-software comparison of the global responses, it can be concluded that a match within 5-15% can be considered within the capability of the available computer programs Sima and OrcaFlex, except for LC4.

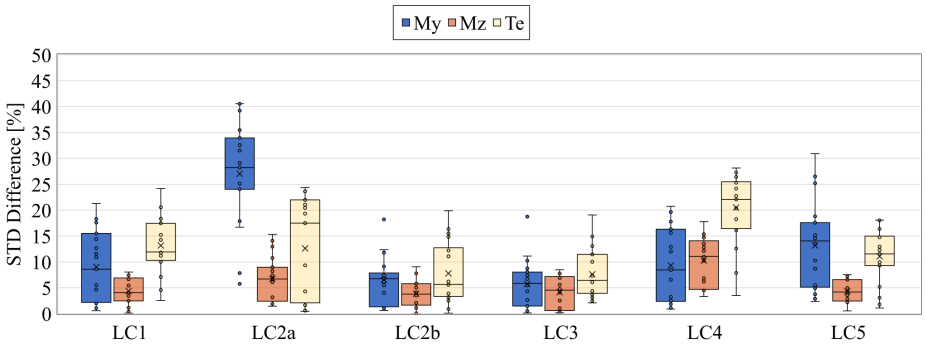

Fig. 14: Box plots of the absolute difference in the standard deviation of the response for load effects in the different load cases. LC2a and LC2b are with Sima default and manually specified angles in the spreading function, respectively. The × indicate the average value along the bridge axes.

5 | Verification towards previous experiments

This chapter is a summary of the content of the third paper and deals with uncertainty assessment and verification of Sima towards previous experiments carried out by Marintek (now SINTEF Ocean) in 1989 for a generic floating pontoon bridge concept.

Motivated by the same undocumented performance of available computer programs for general multi-purpose offshore structural analysis when applied to floating bridge concepts, as was the case for the second paper, a model uncertainty assessment and verification of Sima towards existing experiments from 1989 is carried out. Different methods are available for assessing the performance of a numerical model depending on how much information is accessible to the user. System identification based on the matrix formulation of the structural system has already been carried out for a floating bridge concept in frequency domain, see e.g. [57–59]. However, the system identification method is not a possible option as part of the general multi-purpose offshore structural analysis software such as Sima or OrcaFlex, and instead a range of sensitivity tests are performed for the most relevant parameters of interest.

Previously Sima has been verified for other applications, see e.g. [60–63], but not when applied to a floating pontoon bridge concept. Instead, other software have previously been compared to the same experiments, see Løken and Oftedal [64] and Xiang and Løken [65]. Løken and Oftedal compared the experiments to a numerical model in the frequency domain. The solution to the equation of motion was based on the direct frequency-response method with one solution for each long-crested wave frequency. Stochastic response was calculated as part of the post-processing using statistical methods. With the system being linear, no effects such as slow-drift, viscous drag or current effects were accounted for. Xiang and Løken did a comprehensive number of comparisons using three different numerical models in OrcaFlex. The first and second model were based on the time domain and frequency domain method, respectively, with no hydrodynamic interaction accounted for. The third model was based on the time domain method and included hydrodynamic interaction between the pontoons. They found that the hydrodynamic interaction had an effect on the vertical displacement response of the bridge for some frequencies of long-crested waves. They also found a dampening effect in the response when applying currents to the long-crested waves - opposite to the amplifying effect found in the experiments.

The present study describes the numerical and experimental models and the corresponding results in more detail than before in the literature and employs a meticulous step-by-step approach in order to assess the uncertainties of the numerical model using sensitivity studies. Using a manually implemented iteration for calculating the natural frequencies which includes the frequency-dependent added mass, a closer fit to the natural frequencies of the experimental model is obtained, strengthening the overall comparison.

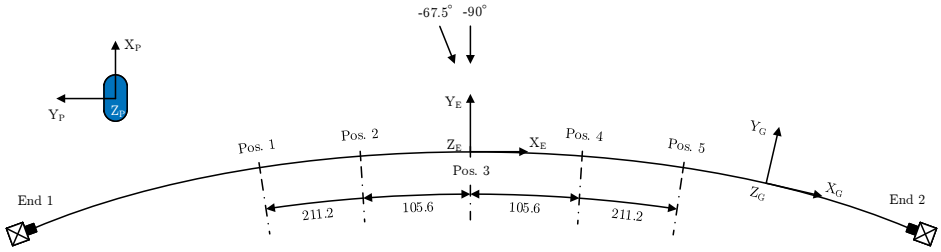

(a) View from above with location of measurement points and wave directions.

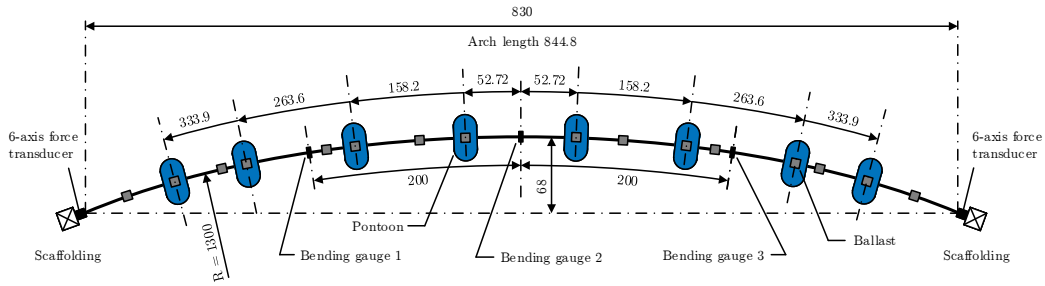

(b) View from above with location of pontoons, ballast, force transducers and bending- and shear gauges.

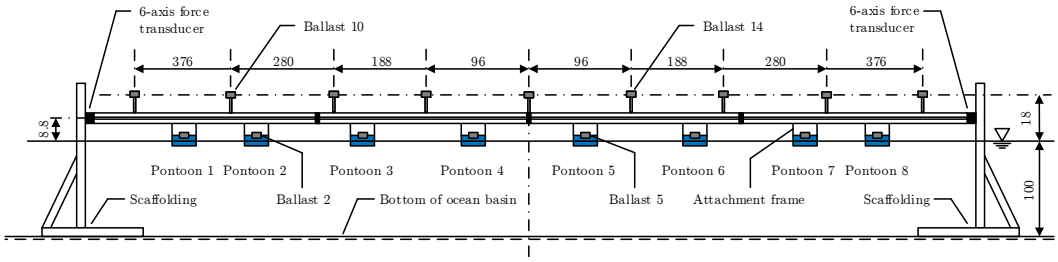

(c) View from the side showing location of traffic ballast, water depth and height of bridge girder.

Fig. 15: Sketch of the experimental model of the floating pontoon bridge used in the third paper with all dimensions in m, referring to full scale.

5.1 Description of the 1989 experiments used for verification

The experiments were carried out by Marintek (now SINTEF Ocean) in 1989 for a 830 m long simplified curved floating pontoon bridge model, used in the design of the Bersøysund- and Nordhordland Bridge. A sketch of the small scale model is illustrated in Fig. 15, giving an overview of the full scale dimensions and the location of the force- and motion response measuring devices.

The model consists of a curved bridge girder 8.8 m above the MWL with a radius of curvature of 1,300 m in the horizontal plane. Along the bridge are 8 pontoons supporting the bridge and at 17 locations ballast from traffic load is added at various heights, see Fig. 15c. The water depth is equivalent to 100 m in full scale. Rotational springs are inserted at the two ends to allow for rotation about the weak and strong axis of the bridge girder, whereas the torsional rotation of

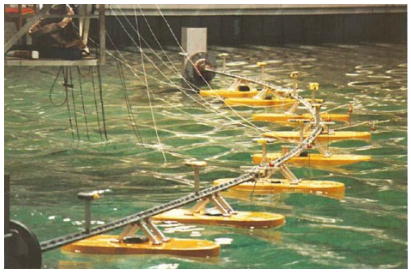

(a) Experimental model. Photograph from [65].

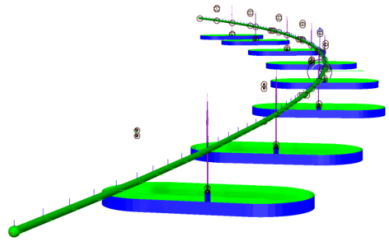

(b) Model 3.

Fig. 16: Visual comparison of the experimental and numerical models.

the bridge girder is kept fixed.

Model 3 is created in Sima with corresponding mass- and stiffness properties and a visual comparison of the experimental and numerical model is shown in Fig. 16. For details about Model 3, please see the appended third paper.

5.1.1 Measurement instrumentation

The vertical and transverse displacement of the bridge and torsional rotation are measured at five positions along the bridge corresponding to the 1/4, 3/8, 1/2, 5/8 and 3/4 points of the bridge, illustrated in Fig. 15a. The reaction forces are measured at the two ends of the bridge with 6-axis force transducers and at the 1/4, 1/2 and 3/4 points along the bridge using shear- and bending gauges, see Fig. 15b.

5.1.2 Overview of tests performed in the experiment

The performed tests include both static load tests, decay tests, regular and irregular long-crested waves, short-crested waves and a combination of long-crested waves and current. The dynamic response is given as standard deviations, RAOs and response spectra.

5.1.3 Uncertainties in measured response

Based on the Marintek report [66] about the experiments and a previously published article [64], the uncertainty related to the experiments is estimated to be 5-10%. However, due to inevitable inaccuracies in the wave generation procedure and positioning of the model, changes in the wave direction of up to 0.4° are present [66]. Combined with the symmetric shape of the first horizontal mode, the response from beam sea is strongly sensitive to those changes in the long-crested wave direction.

5.2 Important findings

5.2.1 Verification of static response and modal properties

A significant difference was observed between the numerical and experimental model in the initial comparison of the static response and modal properties. Two possible reasons were identified:

Tab. 4: Modal properties of the Model 3 using different modifiers f_{BC} and f_{EI}. The experimental model is compared with Model 3 based on $f_{BC} = 1.00$ and $f_{EI} = 1.18$. Frequency-dependent added mass is taken into account manually.

Mode	$f_{BC} = 1.00$ $f_{EI} = 1.00$		$f_{BC} = 1.00$ $f_{EI} = 1.18$		Experiments	
					Value	Diff.
n	Shape	[s]	Shape	[s]	[s]	[%]
1	Y2	10.64	Y2	9.95[‡]	9.96[†]	-0.1
2	Z1	7.89	Z1	7.88	7.85[§]	0.4
3	Z2	7.70	Z2	7.67	7.35[§]	4.4
4	Z3	7.17	Z3	7.08	6.87[§]	3.1
5	Z4	6.24	Z4	6.07	-	-
6	Y3	5.35	RX1	5.12	5.53[§]	-7.4
7	RX1	5.13	Y3	4.97	4.95[§]	0.4
8	Z5	5.10	Z5	4.88	-	-
9	RX2	4.58	RX2	4.56	4.82[§]	-5.4
10	RX3	4.02	RX3	3.99	-	-

[§] Based on peaks in response spectra from [67]
[†] Based on an experimental decay test [66]
[‡] A numerical decay test returns 9.94 s

i) incorrect rotational spring stiffness values at the two ends, or ii) significant contribution to the bending stiffness from the three shear- and bending gauges inserted at the 1/4, 1/2 and 3/4 points along the bridge. Both scenarios were checked by first multiplying the original rotational spring stiffness with a modifier f_{BC} of various values and later by multiplying the bridge girder bending stiffness with a modifier f_{EI} with different values. From a sensitivity study of the static response and the modal properties, the modifiers were finally chosen as $f_{BC} = 1.00$ and $f_{EI} = 1.18$. The natural periods of the initial and final versions of Model 3 are listed in Tab. 4. The mode shape notation is defined as Y2 for the first horizontal mode with two half sine waves, Z1 for the first vertical mode with one half sine wave and RX1 for the first torsional mode with one half sine wave. The reason for the final choice was mainly that the natural periods of the first two horizontal modes were matching and the static response were most sensitive to changes in f_{EI}.

5.2.2 Sensitivity towards drag coefficient values

In the study, 2-dimensional drag coefficients from the literature are applied in order to include the viscous loads on the pontoons. Due to uncertainties in the applied values a sensitivity study was performed based on ±50% of the initial values. The study found insignificant changes in the response.

5.2.3 Directional sensitivity for beam sea

The symmetric shape of the first horizontal mode makes the response from beam sea strongly sensitive to changes in the long-crested wave direction. Model 3 is idealized and therefore has

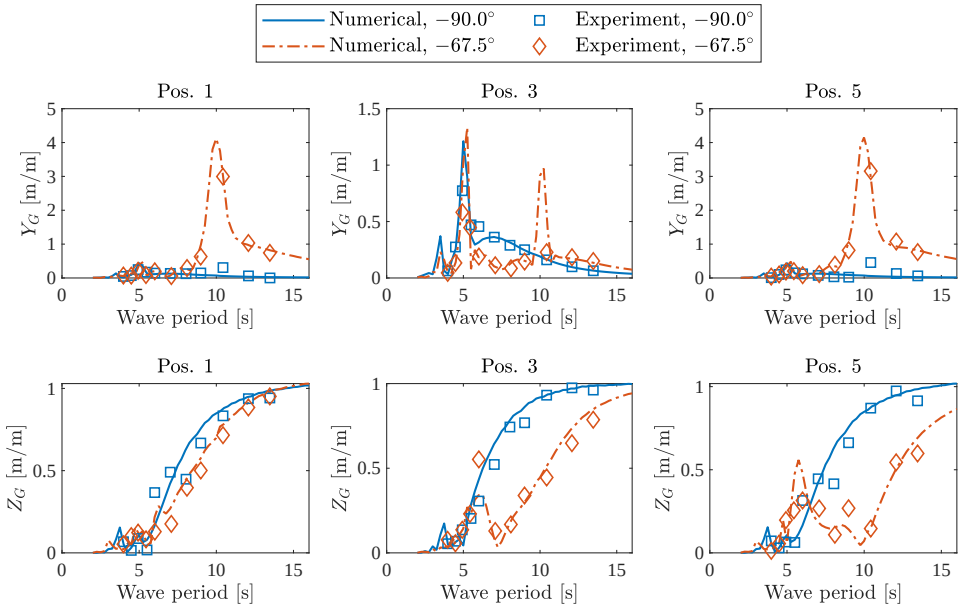

Fig. 17: Comparison of vertical and transverse displacement RAOs between Sima and experiments.

a wave direction of exactly −90.0°, which will cancel out the first horizontal mode due to the structural symmetry. Instead, in the experiments, the wave direction is slightly inaccurate with −90.0 ± 0.4° [66]. In this case, the first mode can be excited. This is clearly shown in the difference between the experiments and Model 3 for the horizontal displacement response Y_G at Pos. 5 in Fig. 17 for waves from −90.0° with a wave period close to 10 s, corresponding to the first horizontal mode. The same directional sensitivity in the response is illustrated in Fig. 18 for irregular long-crested waves.

5.2.4 Response from short-crested wave loads

A good agreement is found between Model 3 and the experiment for short-crested wave loads. The calculated response is less sensitive to the number of wave directions when using more than 50 wave directions in the directional spreading function.

5.2.5 Current-wave interaction effects

For cases with long-crested irregular waves, there is roughly a 6% increase in the measured response with increased wave height. The same increase is present for cases with and without an added current. The corresponding increase is calculated to roughly 9% in Model 3.

When keeping the significant wave height constant there is an increase in the measured response of roughly 17% when adding current to cases of both low and high significant wave heights. The same increase is roughly 10% in Model 3.

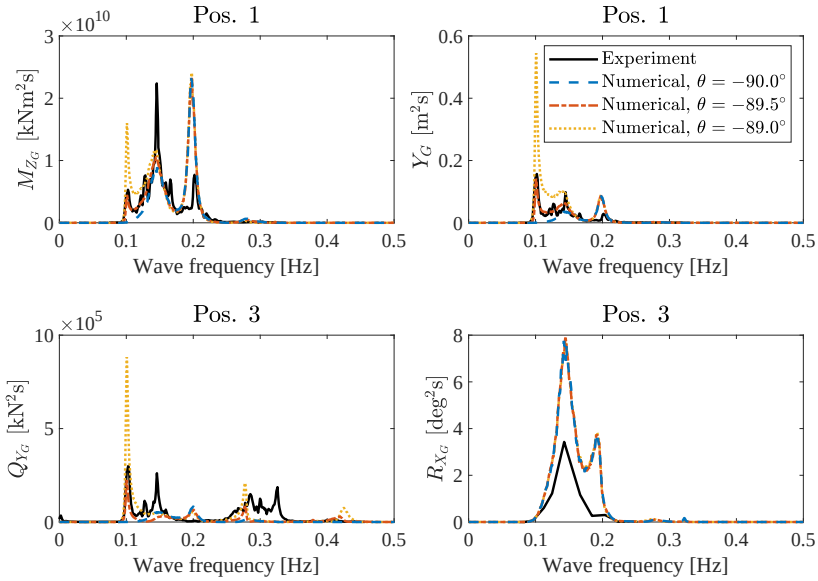

Fig. 18: Directional sensitivity in structural response for irregular long-crested waves.

6 | Concluding remarks

The present thesis describes research related to uncertainty assessment of the wave- and current induced global response for horizontally curved floating pontoon bridges. The research is based on numerical studies performed mainly with the computer program Sima, used for general multi-purpose offshore structural analysis, and some studies are performed with the computer program OrcaFlex for comparison purposes. As a pre-requisite for the numerical studies, three different numerical models are created in Sima - one model for each appended paper, with corresponding numbers.

Model 1. A simplified version of the Bjørnafjord phase 2 concept with one single equivalent beam cross-section for the bridge girder at a constant height along the bridge with supporting pontoons for every 197 m, connected with columns

Model 2a. A complex version of the Bjørnafjord phase 2 concept following the design description with only slight simplifications in order to better compare Sima and OrcaFlex

Model 3. A replica of the experimental model used in the 1989 ocean basin experiments carried out by Marintek (now SINTEF Ocean), in order to verify Sima against experiments when applied to a floating pontoon bridge structure

The numerical studies assess uncertainties related to the analysis and design of floating pontoon bridges. The assessment started with an investigation of the effect of wave direction uncertainty on the extreme response, then a comparison of the performance of two commonly used computer programs when used for a global response analysis and, finally, an uncertainty assessment and verification of the computer program Sima by comparing with existing experimental results.

6.1 Original contributions

The present thesis is a collection of three appended papers and their original contributions to the scientific community can be boiled down to the following points.

Reference for accuracy in extreme response. Based on a large amount of statistically independent realizations, a reference is made in the first appended paper for how many samples are needed and how long each time series should be, in order to accurately describe the short-term extreme structural response of a floating pontoon bridge structure.

Effect of wave direction parameters on extreme response. A parametric study is conducted in the first appended paper to investigate the relationship between changes in two common

wave direction parameters for short-crested waves and the extreme structural response of a floating pontoon bridge concept. The two parameters are the main wave direction and the spreading exponent. Based on the above mentioned reference and a target accuracy of 2%, 40 statistically independent 3-hour realizations are used for each combination of the parameters. The study concludes that changes in the main wave direction only have a small effect on the response as long as the variation is within ±15° from beam sea. Similarly, varying the spreading exponent between two opposing but naturally occurring spreading exponent values, i.e. 2 and 10, has a relatively small effect on the response.

Reference for comparison of Sima and OrcaFlex floating bridge models. A comprehensive comparison is made between two commonly used computer programs for general multi-purpose offshore structural analysis. The comparison is based on numerical models created in Sima and OrcaFlex based on the exact same geometric input for the Bjørnafjord phase 2 floating bridge concept selected by the NPRA. Care has been taken to make both computer programs compatible when different methods had to be used in the user-given inputs. A step-by-step approach has been used to make sure static and modal properties are as close as possible before comparison of the dynamic responses. Overall, the global responses calculated in the two computer programs, are found to be within 5-15% of each other, depending on the load case and response type. Although the differences in the modal properties are as small as possible, they are thought to be the underlying cause of the differences in the calculated structural responses.

Verification of Sima when applied to a floating pontoon bridge concept. A numerical model is created to verify Sima towards experiments carried out in 1989 by Marintek (now SINTEF Ocean) for a generic floating pontoon bridge. The comparison involves several sensitivity studies in order to quantify the effect of uncertainties in physical properties, due to the lack of information in the 30 year old reports from the experiments. Based on these sensitivity studies, the bending stiffness of the bridge girder in the numerical model is updated in order to match the stiffness from inserted shear- and bending gauges in the experimental model. A good match is found in the static response and the modal properties with natural periods coinciding with that of decay tests and stochastic response spectra from experimental tests. Based on an uncertainty in the measured response of 5-10%, a good fit is obtained with the calculated response and Sima is thereby verified for application to such curved floating pontoon bridge concepts with similar span lengths.

6.2 Limitations and future work

In pursuit of the research objectives of the present thesis, different assumptions and simplifications are made in order to narrow the scope of the research. These assumptions and simplifications, however, impose some limitations on the conclusions and further work is suggested in order to improve upon or extent the current research.

In estimating the effect of wave direction parameters on the extreme response of a floating bridge concept, a simplified linear numerical model of the Bjørnafjord phase 2 floating bridge concept is utilized with only first order wave loads. This decision was based on the fact that waves are the dominant load for the Bergsøysund Bridge [68] and the assumption that the same would hold in our case since the geometry is very similar. The drawback of this approach is that other environmental loads have proved to be important for the dynamic response and the findings

should therefore be used with these limitations in mind. For instance, Wang et al. [69] showed that wind loads can have a significant dampening effect on the wave load response for a 3-span suspension bridge structure with floating pylons. More specifically for the Bjørnafjord phase 2 floating pontoon bridge concept, Cheng et al. [70] have shown that for combined wind and wave loads from a 270° direction, the horizontal response and the axial force were dominated by wind loads, whereas the vertical response and torsional moments were dominated by wave loads. In the same study they found current to have a dampening effect on the response in general. Cheng et al. [71] investigated the statistical properties of the extreme strong axis bending moment- and axial force responses of the same bridge concept when subjected to only waves from beam sea and when subjected to aligned waves and wind from beam sea. By looking at the PDF of the 100-year response time series they found that for both response processes, the skewness was very close to zero and that the kurtosis was close to 3. This suggests that the underlying processes for both response types are close to a Gaussian process. Based on these findings, future studies are suggested to include both first order waves, wind, current and non-linear effects such as viscous damping, low-frequency wind and second order difference-frequency wave loads when estimating the extreme response for a bridge such as the Bjørnafjord phase 2 floating bridge concept.

Two extensive numerical models of the Bjørnafjord phase 2 floating bridge concept are used to compare the two computer programs Sima and OrcaFlex. However, the comparison is limited to only include first and second order wave forces, viscous drag and short-crested waves. Both wind and current loads have been disregarded and this introduces the same drawbacks as discussed above. Future work is needed in order to estimate the differences when the structure is exposed to wind and current loads. For instance, in the third appended paper wave-current interaction in Sima amplifies the structural response of a floating pontoon bridge, whereas Xiang and Løken [65] predict a dampening effect in OrcaFlex.

The verification of Sima towards the 1989 experiments conducted by then Marintek is based on a generic floating pontoon bridge concept with a length of roughly 830 m. With lengths of up to 5,000 m for the current floating bridge concepts selected by the NPRA, the verification is questionable for similar structures with lengths more than five times that of the previously tested model. Future experiments are required to verify Sima for longer bridge concepts, although this is not feasible due to the extensive lengths of the bridge concepts, the scaling requirements and the size of existing ocean basins. Instead hybrid tests need to be performed. Finally, the conducted verification is based on response quantities such as response amplitude operators, standard deviations and response spectra. A future verification would be enhanced by comparing with actual time series from the experiment.

References

[1] Sturgeon, D. Chinese Text Project: a dynamic digital library of premodern Chinese. *Digital Scholarship in the Humanities*, 08 2019. doi:10.1093/llc/fqz046.

[2] Needham, J., Ling, W., and Gwei-Djen, L. *Science and Civilization in China*, volume 4. Cambridge University Press, 1971.

[3] Herodotus. *The history of Herodotus*, volume IV. 2013. https://www.gutenberg.org/files/2707/2707-h/2707-h.htm. Accessed January 22, 2020.

[4] Graves, R. *I, Claudius*. Vintage Books, A Division of Random House, New York, 1989.

[5] Kvåle, K. A. *Dynamic behaviour of floating bridges exposed to wave excitation - A numerical and experimental investigation*. Phd thesis, Norwegian University of Science and Technology, 2017. http://hdl.handle.net/11250/2479175.

[6] Watanabe, E. Floating Bridges : Past and Present Types of Floating Bridge. *Structural Engineering International*, 2:128–132, 2003.

[7] Hartz, B. J. and P., R. E. Structural response of floating bridge under wind wave loading. In *ASCE National Transportation Engineering Conference*, Portlan, Oregon, 1970.

[8] Hartz, B. J. and B., M. Response of Floating Bridges to Random Wave Forces. In *ASCE-ASME National Transportation Engineering Conference*, Seattle, 1971.

[9] Hartz, B. J. and Georgiadis, C. A finite element program for dynamic response of continuous floating structures in short-crested waves. In *Proceedings, International Conference on Finite Element Analysis*, Shanghai, 1982. PRC 1982.

[10] Holand, I. and Langen, I. Salhus floating bridge: theory and hydrodynamic coefficients. Technical report, SINTEF, 1972.

[11] Sigbjörnsson, R. and Langen, I. Wave-induced vibrations of a floating bridge - a monte carlo approach. Technical report, SINTEF, Trondheim, Norway, 1975.

[12] Sigbjörnsson, R. and Langen, I. Wave-induced vibrations of a floating bridge - The Salhus Bridge. Technical report, SINTEF, Trondheim, Norway, 1975.

[13] Clough, D., Sigbjörnsson, R., and Remseth, S. N. Response of a submerged, buoyant tubular bridge subjected to irregular sea waves. Technical report, SINTEF, 1977.

[14] Holand, I., Sigbjörnsson, R., and Langen, I. Dynamic analysis of a curved floating bridge. *IABSE Proceedings*, pages 1–16, 1977. , P-5/77.

[15] Sigbjörnsson, R. Stochastic theory of wave loading processes. *Engineering Structures*, 1(2): 58–64, 1979. ISSN 01410296. doi:10.1016/0141-0296(79)90014-2.

[16] Langen, I. and Sigbjörnsson, R. On stochastic dynamics of floating bridges. *Engineering Structures*, 2(4):209–216, 1980. ISSN 01410296. doi:10.1016/0141-0296(80)90002-4.

[17] Langen, I. Probabilistic methods for dynamic analysis of floating bridges. *Norwegian Maritime Research*, 11(1):2–15, 1983.

[18] Leira, B. J. Probabilistic design - An application to floating bridges. Technical report, SINTEF, 1983.

[19] Leira, B. J. and Langen, I. On probabilistic design of a concrete floating bridge. *Nordic concrete research*, (3):140–166, 1984.

[20] Leira, B. J. and Øderud, H. T. Load combinations for continuous floating bridges. In *Proceedings of the 1st Symposium on Strait Crossings*, pages 299–318, Stavanger, Norway, 1986.

[21] Moan, T., Gao, Z., and Ayala-Uraga, E. Uncertainty of wave-induced response of marine structures due to long-term variation of extratropical wave conditions. *Marine Structures*, 18(4):359–382, 2005. ISSN 0951-8339. doi:10.1016/j.marstruc.2005.11.001.

[22] Bitner-Gregersen, E. M., Ewans, K. C., and Johnson, M. C. Some uncertainties associated with wind and wave description and their importance for engineering applications. *Ocean Engineering*, 86:11–25, 2014. ISSN 00298018. doi:10.1016/j.oceaneng.2014.05.002.

[23] Kvåle, K. A. and Øiseth, O. Characterization of the wave field around an existing end-supported pontoon bridge from simulated data. In *Proceedings of the International Conference on Earthquake Engineering and Structural Dynamics*, volume 47, pages 345–359. Springer International Publishing, 2019. ISBN 978-3-319-78187-7. doi:10.1007/978-3-319-78187-7_26.

[24] Cheng, Z., Svangstu, E., Gao, Z., and Moan, T. Field measurements of inhomogeneous wave conditions in bjørnafjorden. *Journal of Waterway, Port, Coastal, and Ocean Engineering*, 145 (1):05018008, 2018. doi:10.1061/(ASCE)WW.1943-5460.0000481.

[25] Cheng, Z., Gao, Z., and Moan, T. Wave load effect analysis of a floating bridge in a fjord considering inhomogeneous wave conditions. *Journal of Engineering Structures*, 163: 197–214, 2018. ISSN 0141-0296. doi:10.1016/j.engstruct.2018.02.066.

[26] Faltinsen, O. M. *Sea loads on ships and offshore structures*. Cambridge University Press, 1993. ISBN 0521458706.

[27] Xiang, X. *Maneuvering of two interacting ships in waves*. Phd thesis, Norwegian University of Science and Technology, 2012. https://brage.bibsys.no/xmlui/handle/11250/238361.

[28] Xiang, X., Viuff, T., Leira, B., and Øiseth, O. Impact of hydrodynamic interaction between pontoons on global responses of a long floating bridge under wind waves. In *Proceedings of the 37th International Conference on Ocean, Offshore and Arctic Engineering*, pages 1–11, 2018. doi:10.1115/OMAE2018-78625.

[29] Stansberg, C. T., Ormberg, H., and Oritsland, O. Challenges in deep water experiments: Hybrid approach. *Journal of Offshore Mechanics and Arctic Engineering*, 124:90–96, 2002. doi:10.1115/1.1464129.

[30] Petersen, Ø. W., Øiseth, O., and Lourens, E. Full-scale identification of the wave forces exerted on a floating bridge using inverse methods and directional wave spectrum estimation. *Mechanical Systems and Signal Processing*, 120:708–726, 2019. ISSN 0888-3270. doi:10.1016/j.ymssp.2018.10.040.

[31] SINTEF Ocean. *SIMO 4.14.0 Theory Manual*. Trondheim, Norway, 2018.

[32] SINTEF Ocean. *RIFLEX 4.14.0 Theory Manual*. Trondheim, Norway, 2018.

[33] Orcina. *OrcaFlex Documentation*, 2019. https://www.orcina.com/webhelp/OrcaFlex/. Accessed January 22, 2020.

[34] Ormberg, H., Fylling, I. J., Larsen, K., and Sødahl, N. Coupled analysis of vessel motions and mooring and riser system dynamics. In *Proceedings of the International Conference on Offshore Mechanics and Arctic Engineering*, pages 91–100. American Society of Mechanical Engineers, 1997.

[35] Cummins, W. E. *The impulse response function and ship motions*. Washington DC, USA, 1962. https://dome.mit.edu/handle/1721.3/49049. Report no. DTMB-1661.

[36] Lui, Z. and Frigaard, P. *Generation and analysis of random waves*. Aalborg University, 3 edition, 2001.

[37] Hasselmann, K., Barnett, T. P., Bouws, E., Carlson, H., Cartwright, D. E., Enke, K., Ewing, J. A., Gienapp, H., Hasselmann, D. E., Kruseman, P., Meerburg, A., Muller, P., Olbers, D. J., Richter, K., Sell, W., and Walden, H. Measurements of Wind-Wave Growth and Swell Decay during the Joint North Sea Wave Project (JONSWAP). *Deutsche Hydrographische Zeitschrift*, 8(12), 1973.

[38] Statens vegvesen. *Design basis MetOcean*. Oslo, Norway, 2017. Report no. SBJ-01-C3-SVV-01-BA-001.

[39] Statens vegvesen. *Curved bridge - navigation channel in south*. Oslo, Norway, 2016. https://www.vegvesen.no/_attachment/1605060/. Report no. NOT-KTEKA-021.

[40] Fu, P., Leira, B. J., Myrhaug, D., and Chai, W. Assesment of methods for short-term analysis of riser collision probability. *Ocean Engineering*, 2019. , Under review.

[41] Naess, A. and Moan, T. *Stochastic Dynamics of Marine Structures*. Cambridge University Press, 2013.

[42] Sødahl, N. *Methods for design and analysis of flexible risers*. Phd thesis, The Norwegian Institute of Technology, 1991.

[43] Ochi, M. K. *Applied Probability and Stochastic Processes*. John Wiley & Sons, Inc., 1990. ISBN 0-471-85742-4.

[44] Fu, P. *Reliability Analysis of Wake-induced Riser Collision*. Phd thesis, Norwegian University of Science and Technology, 2019. http://hdl.handle.net/11250/2631481.

[45] Gumbel, E. J. *Statistics of Extremes*. Columbia University Press, 1958.

[46] Spidsøe, N. and Karunakaran, D. N. Nonlinear dynamic behaviour of jack-up platforms. *Marine Structures*, 9(1):71–100, 1996. ISSN 0951-8339. doi:10.1016/0951-8339(95)00005-Q.

[47] Farnes, K.-A. and Moan, T. Extreme dynamic, non-linear response of fixed platforms using a complete long-term approach. *Applied Ocean Research*, 15(6):317–326, 1993. ISSN 0141-1187. doi:10.1016/0141-1187(93)90001-E.

[48] Fu, P., Leira, B. J., and Myrhaug, D. Assesment of methods for short-term extreme value analysis of riser collision. pages 1–9, 2018. doi:10.1115/OMAE2018-78318.

[49] Langen, I. and Sigbjörnsson, R. On stochastic dynamics of floating bridges. *Engineering Structures*, 2(4):209–216, 1980. ISSN 0141-0296. doi:10.1016/0141-0296(80)90002-4.

[50] Villoria, B. Floating bridge technology - prediction of extreme environmental load effects. In *Proceedings of the 35th International Conference on Ocean, Offshore and Arctic Engineering*, pages 1–8. ASME, 2016. doi:10.1115/OMAE2016-54433.

[51] Giske, F.-I. G., Kvåle, K. A., Leira, B. J., and Øiseth, O. Long-term extreme response analysis of a long-span pontoon bridge. *Marine Structures*, 58:154–171, 2018. ISSN 0951-8339. doi:10.1016/j.marstruc.2017.11.010.

[52] Øiseth, O., Rönnquist, A., Naess, A., and Sigbjörnsson, R. Estimation of extreme response of floating bridges by monte carlo simulation. In *Proceedings of the 9th International Conference on Structural Dynamics, EURODYN*, pages 2905–2912, 2014. ISBN 978-972-752-165-4.

[53] Giske, F.-I. G., Leira, B. J., and Øiseth, O. Long-term extreme response analysis of marine structures using inverse sorm. *Journal of Offshore Mechanics and Arctic Engineering*, 140(5): 1–8, 2018. doi:10.1115/1.4039718.

[54] Naess, A. and Gaidai, O. Estimation of extreme values from sampled time series. *Structural Safety*, 31(4):325–334, 2009. doi:10.1016/j.strusafe.2008.06.021.

[55] Remseth, S. N., Leira, B. J., Okstad, K. M., Mathisen, K. M., and Haukås, T. Dynamic response and fluid/structure interaction of submerged floating tunnels. *Computers and Structures*, 72(4):659–685, 1999. ISSN 00457949. doi:10.1016/S0045-7949(98)00329-0.

[56] Leira, B. J. and Remseth, S. Directional effects and multicomponent dynamic response of marine bridges. In *Proceedings of the 2nd Symposium on Strait Crossings*, pages 233–239. Balkema Publishers Rotterdam, 1990.

[57] Larssen, R. M., Leira, B. J., and Remseth, S. N. Structural parameter identification for marine bridges. In *Proceedings of the 15th International Conference on Offshore Mechanics and Arctic Engineering*, volume 2, Florence, 1996.

[58] Petersen, Ø. W. and Øiseth, O. Sensitivity-based finite element model updating of a pontoon bridge. *Engineering Structures*, 150:573–584, 2017. ISSN 0141-0296. doi:10.1016/j.engstruct.2017.07.025.

[59] Kvåle, K. A., Øiseth, O., and Rønnquist, A. Operational modal analysis of an end-supported pontoon bridge. *Engineering Structures*, 148:410–423, 2017. ISSN 0141-0296. doi:10.1016/j.engstruct.2017.06.069.

[60] Viuff, T., Xiang, X., Leira, B., and Øiseth, O. Code-to-code verification of end-anchored floating bridge global analysis. In *Proceedings of the 37th International Conference on Offshore Mechanics and Arctic Engineering*, pages 1–9, 2018. doi:10.1115/OMAE2018-77902.

[61] Karimirad, M., Meissonnier, Q., Gao, Z., and Moan, T. Hydroelastic code-to-code comparison for a tension leg spar-type floating wind turbine. *Marine Structures*, 24:412–435, 10 2011. doi:10.1016/j.marstruc.2011.05.006.

[62] Robertson, A., Jonkman, J., Vorpahl, F., Popko, W., Qvist, J., Frøyd, L., Chen, X., Azcona, J., Uzunoglu, E., Soares, C. G., Luan, C., Yutong, H., Pengcheng, F., Yde, A., Larsen, T., Nichols, J., Buils, R., Lei, L., Nygaard, T. A., Manolas, D., Heege, A., Vatne, S. R., Ormberg, H., Duarte, T., Godreau, C., Hansen, H. F., Nielsen, A. W., Riber, H., Cunff, C. L., Beyer, F., Yamaguchi, A., Jung, K. J., Shin, H., Shi, W., Park, H., Alves, M., and Guérinel, M. Offshore Code Comparison Collaboration Continuation Within IEA Wind Task 30: Phase II Results Regarding a Floating Semisubmersible Wind System. In *Proceedings of the 33rd International Conference on Ocean, Offshore and Arctic Engineering*. ASME, 2014. ISBN 978-0-7918-4554-7. doi:10.1115/OMAE2014-24040.

[63] Sørum, S. H., Horn, J.-T. H., and Amdahl, J. Comparison of numerical response predictions for a bottom-fixed offshore wind turbine. *Energy Procedia*, 137:89–99, 2017. ISSN 1876-6102. doi:10.1016/j.egypro.2017.10.336.

[64] Løken, A. E. and Oftedal, R. A. Aspects of hydrodynamic loading and response in design of floating bridges. *Second Symposium on Strait Crossings*, pages 479–486, 1990.

[65] Xiang, X. and Løken, A. Hydroelastic analysis and validation of an end-anchored floating bridge under wave and current loads. In *Proceedings of the 38th International Conference on Offshore Mechanics and Arctic Engineering*, pages 1–9, 2019.

[66] Statens vegvesen. *Modellforsøk med flytebru: Kontinuerlig pontongbru*. Oslo, Norway, 1989. Report no. MT40 F89-0252.

[67] Statens vegvesen. *Sammenligning mellom modellforsøk og beregninger av en enkelt pongtong og en flytebru med separate pongtonger*. Høvik, Norway, 1990. Report no. 89-3440.

[68] Kvåle, K. A. and Øiseth, O. Structural monitoring of an end-supported pontoon bridge. *Marine Structures*, 52:188–207, 2017. ISSN 0951-8339. doi:10.1016/j.marstruc.2016.12.004.

[69] Wang, J., Cheynet, E., Snæbjörnsson, J., and Jakobsen, J. B. Coupled aerodynamic and hydrodynamic response of a long span bridge suspended from floating towers. 177:19–31, 4 2018. doi:10.1016/j.jweia.2018.03.024.

[70] Cheng, Z., Gao, Z., and Moan, T. Numerical modelling and dynamic analysis of a floating bridge subjected to wind, wave and current loads. *Journal of Offshore Mechanics and Arctic Engineering*, 141, 2018. doi:10.1115/1.4040561.

[71] Cheng, Z., Gao, Z., and Moan, T. Extreme Response Analysis of an End-Anchored Floating Bridge. In *Proceedings of the 38th International Conference on Ocean, Offshore and Arctic Engineering*, pages 1–10. ASME, 6 2019. doi:10.1115/OMAE2019-96793.

Paper 1

Thomas Viuff, Bernt Johan Leira, Xu Xiang and Ole Øiseth

"Effects of wave directionality on extreme response for a long end-anchored floating bridge"

Applied Ocean Research, vol. 90, pp. 101843, May 2019.

Applied Ocean Research 90 (2019) 101843

Contents lists available at ScienceDirect

Applied Ocean Research

journal homepage: www.elsevier.com/locate/apor

Effects of wave directionality on extreme response for a long end-anchored floating bridge

Thomas Viuff[a,*], Bernt Johan Leira[a], Xu Xiang[b], Ole Øiseth[c]

[a] Department of Marine Technology, Norwegian University of Science and Technology, N-7491 Trondheim, Norway
[b] Norwegian Public Roads Administration, N-0667 Oslo, Norway
[c] Department of Structural Engineering, Norwegian University of Science and Technology, N-7491 Trondheim, Norway

ARTICLE INFO

Keywords:
Floating bridge
Von Mises stress
Short-term extreme response
Accuracy in extreme response prediction
Main wave direction
Spreading exponent

ABSTRACT

Reliable design codes are of great importance when constructing new civil engineering concepts such as floating bridges. Previously only a scarce number of floating bridges have been built in rough wave conditions and only limited knowledge of the extreme environmental conditions and the associated extreme response exists. To form a better design basis an increased understanding of the sensitivity in the structural response towards changes in short-crested sea parameters is needed. Furthermore, acquiring the necessary accuracy in simulated extreme response is often a computationally expensive endeavour and the number of simulations needed is often based on experience. The present study investigates the wave-induced short-term extreme response of a simplified end-anchored floating bridge concept for several wave environments with a return period of 100 years. The study includes convergence of the coefficient of variation for the extreme response for different realization lengths as well as number of realizations. The sensitivity in the structural response towards different main wave directions and spreading exponents is investigated and includes both transverse and vertical displacement response spectra and extreme Von Mises stress in the bridge girder cross-section. The extreme response is based on an accuracy of 2% in the coefficient of variation equivalent to 40 3-h realizations and a low sensitivity in the response is found for natural occurring spreading exponents and for main wave directions within 15° from beam sea.

1. Introduction

The Norwegian Public Roads Administration (NPRA) is currently undertaking a large infrastructure project involving floating bridge structures over their wide and deep fjords. The fjords are up to 1300 m deep, 6000 m wide and located in the western part of Norway exposing the structures to rough wind and wave conditions from the North Sea. These extreme conditions make it important to understand the structural response and their sensitivity to changes in the wave environment. Stochastic wave loading processes and their application in stochastic response of floating bridges has been a research topic since the late 1970s and the structural response of a short (less than 1500 m) curved floating bridge with continuous pontoons was thoroughly investigated in the late 1970s and the 1980s [1–6] when construction of the Bergsøysund Bridge and the Nordhordland Bridge was under way. The studies included both time domain and frequency domain analyses and included regular waves, irregular long-crested waves and short-crested waves. Sigbjörnsson [2] described an explicit representation of the short-crested behaviour of waves in the frequency domain. Coherency functions were used to show the correlation between wave loads as a function of the spreading exponent and the spatial coordinates, based on previous research by Borgman [7]. Langen and Sigbjörnsson [3] applied the directional wave spectrum in time domain and concluded that a design using long-crested waves would yield unreasonably conservative results, whereas for short-crested waves a low sensitivity was found in the response towards changes within naturally occurring spreading exponent values. Hutchison [8] showed that a logical consistency existed between the two principal methods existing at the time for describing the dynamic response from short-crested waves, i.e. superposition of long-crested waves and an explicit representation of the short-crested behaviour of the incident wave field such as the one described by Sigbjörnsson [2]. Another method to give an explicit representation of the wave field mentioned by Hutchison was the use of an empirical *spacial correlation factor* described by Hartz and Georgiadis as a reduction factor for the time series of nodal wave forces in a numerical analysis [8]. Langen and Leira [4–6] carried out several studies on the probabilistic design of the short floating bridge structure focusing on the bending moments and pre-tension force in the bridge

* Corresponding author.
E-mail address: thomas.h.viuff@ntnu.no (T. Viuff).

https://doi.org/10.1016/j.apor.2019.05.028
Received 31 October 2018; Received in revised form 24 May 2019; Accepted 29 May 2019

cross-section. The studies found that the correlation between the bending moments was important to take into account and that it was dependent on the peak period in the wave spectrum. In more recent years Villoria [9] found a lower influence in the response from changes in the spreading exponent and the wave spectrum shape than from changes in the wave direction and wave period for a long (more than 4000 m) straight and a curved floating pontoon bridge.

For many engineering purposes the design wave parameters are taken as valid inputs but as Moan et al. [10] describes, generally for marine structures the extreme response is very sensitive to the amount of data available to represent the long-term variability of the wave conditions. Bitner-Gregersen et al. [11] noted that some epistemic (knowledge based) uncertainties related to environmental descriptions of wind and waves exists, such as non-stationarity, sampling variability and directionality of wind and waves. A comparison of three metocean databases is described in Bitner-Gregersen et al. and the difference in the significant wave height and the zero-crossing period for return periods of 100 years was found to be over 5 m and 4 s, respectively. Another issue argued by Bitner-Gregersen et al. is the frequency-dependent behaviour of the directional spreading in in-situ measurements. Other uncertainties related to in-situ measurements are pointed out by Kvåle and Øiseth [12] who describes the differences in identification methods for characterizing the wave field based on simulated data. They conducted a comparison of two identification methods using three different sensor layouts and found clear differences in the methods for the sensor layouts they used. These uncertainties all relate to the design wave environment and a thorough understanding of the sensitivity in the extreme floating bridge response is needed in order to quantify the importance of these uncertainties.

The extreme response for long floating bridge structures is a topic touched upon in recent years. Giske et al. [13] have compared the environmental contour method with the full long-term extreme method for a long double-curved floating pontoon bridge and found that it can give a rough estimate of the real long-term extreme response. Giske et al. also compared a new Inverse Second Order Reliability Method (ISORM) described in [14] to the full long-term extreme method and found it to give a high accuracy in the long-term extreme response. Øiseth et al. [15] compared the Average Conditional Exceedance Rates (ACER) method described in [16] to the Gumbel method for the extreme response for a short curved floating pontoon bridge and found that the ACER method had a significantly narrower confidence interval, introducing less uncertainty in the estimation of the extreme response. Xu et al. [17] compared two short-term extreme methods based on the ACER method to a full long-term extreme method for a single-span suspension bridge and found the extreme load effects from the full long-term extreme method to be 14% higher.

With the rough wave conditions at the Bjørnafjord and the described uncertainties in the estimation of the wave parameters, it is important to understand the structural response and the effect of changes in these parameters on the extreme response. The current paper presents an extensive numerical study of the extreme response for a long end-anchored floating pontoon bridge with emphasis on the needed simulation length and number of realizations in order to achieve the necessary accuracy and a parametric study of the extreme response based on the main wave direction and the spreading exponent for short-crested sea. To the knowledge of the authors, all previous studies on the sensitivity of the extreme response to the wave directionality has either been conducted in frequency domain or on a few short time domain simulations. In the present paper it is the first time a numerical parameter study is based on an extensive amount of time domain simulations for each changed parameter and will help solidify the understanding of their effect on the extreme response of a long floating bridge. As part of the extensive time domain calculations the dependency of the accuracy in the short-term extreme prediction towards the simulation length and the number of realizations has been investigated for the general floating bridge structure to be used as a reference for future investigations of the extreme response.

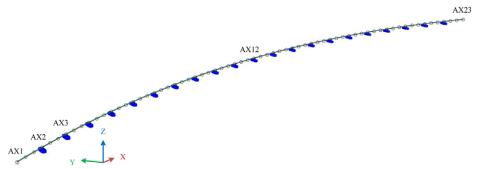

Fig. 1. Numerical model of the end-anchored floating bridge.

2. Description of the floating bridge concept

The floating bridge modelled in the present study is a simplification of the Bjørnafjord end-anchored floating bridge concept described by COWI [18]. The simplified concept seen in Fig. 1 consists of a double-symmetric twin-box cross-section bridge girder at roughly 15 m height, covering roughly 4360 m of roadline and has a curvature of 5000 m in the horizontal plane. The bridge girder is connected to 21 floating pontoons every 197 m with two circular columns. The pontoons are the only part of the bridge in contact with the water and the bridge girder is connected to the shore at each end of the bridge, modelled as fixed connections. The bridge girder and the columns are modelled as single equivalent beams in the numerical model with the cross-sectional properties listed in Table 1.

The pontoons all consist of the same geometry, draft and hydrodynamic coefficients. Looking at a pontoon from above, the geometry is made up of two half circles with a rectangle in between, see Fig. 2. The total length is 68 m, the total width is 28 m and the height is 14.5 m with a draft of 8.8 m found from static equilibrium. For all the pontoons surge follows the global x-axis and sway follows the global y-axis as shown in Fig. 2. Throughout this paper indices one to six for hydrodynamic coefficients indicate surge, sway, heave, roll, pitch and yaw accordingly. Table 2 lists the properties of the pontoon. Based on the bridge girder mass in Table 1 and the pontoon mass and displacement in Table 2 the static equilibrium can be verified.

3. Methodology

The aim of the paper is two-fold: (1) to find the required realization length and number of realizations to achieve a reliable accuracy in the extreme response and (2) to describe the effect of changing short-crested sea parameters on the extreme response. In the following a description is given of the numerical model as well as the assumptions made in order to calculate the stresses in the bridge girder from the internal forces given as output in the numerical model. Later on the choice of parameters to be changed in the parametric study is argued and finally a description is given of how the extreme response is estimated and how the necessary accuracy is achieved.

Table 1
Single equivalent beam cross-section properties [18]. The notations EI_y and EI_z refer to the bending stiffness about the weak and strong axis, respectively, and the notation EA refer to the axial stiffness. Similarly the notations GI_x and r_x refer to the torsional stiffness and the radius of gyration, respectively.

Property	Unit	Girder	Column
Mass	[ton/m]	2.67E+01	1.60E+01
r_x	[m]	2.02E+01	1.84E+01
EA	[kN]	3.87E+08	3.68E+08
EI_y	[kNm^2]	2.76E+09	2.92E+09
EI_z	[kNm^2]	1.56E+11	1.29E+11
GI_x	[kNm^2/rad]	6.10E+10	5.07E+10

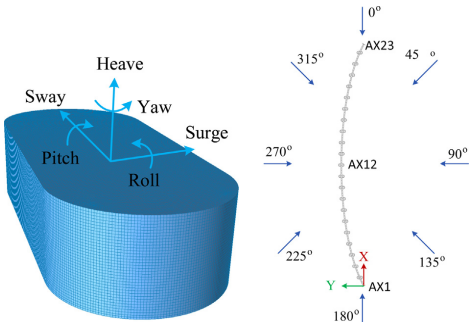

Fig. 2. Pontoon panel model and body-fixed coordinate system (left) and compass notation of wave directions and global coordinate system (right).

Table 2
Pontoon properties [18].

Property	Unit	Value
Mass	[ton]	1.03E+04
Roll inertia	[ton m^2]	4.93E+06
Pitch inertia	[ton m^2]	1.21E+06
Yaw inertia	[ton m^2]	5.47E+06
COG from waterline	[m]	−2.53E+00
Displacement	[ton]	1.57E+04
Roll water plane stiffness	[kNm/rad]	5.33E+06
Pitch water plane stiffness	[kNm/rad]	6.18E+05
Heave stiffness	[kN/m]	1.75E+04

3.1. Numerical model

The numerical model of the floating bridge is developed in the coupled hydro-elastic code SIMO-RIFLEX [19,20]. The structural system is idealized using the Finite Element Method (FEM) with the bridge girder and the columns modelled as Euler-Bernoulli beams and the pontoons as 6 degrees of freedom (DOF) nodes with hydrodynamic mass, stiffness and damping properties. The bridge girder is fixed at each end in all DOF. The mesh of the model is made up of girder elements of roughly 5 m and column elements of roughly 3 m lengths, resulting in a total of roughly 950 beam elements in the model. The hybrid frequency- and time domain model is utilized in the code to set up the equation of motion commonly known as the Cummin's equation [21,22].

$$\begin{aligned} q_j^{\text{exc}}(t) &= \sum_{k=1}^{6} [M_{\text{jk}} + A_{\text{jk}}^{\infty}]\ddot{u}_k(t) + D_{\text{jk}}\dot{u}_k(t) \\ &+ [K_{\text{jk}} + C_{\text{jk}}]u_k(t) + \int_0^{t_{\text{mem}}} k_{\text{jk}}(t-\tau)\dot{u}_k(\tau)d\tau \end{aligned} \quad (1)$$

Here, M_{jk}, D_{jk} and K_{jk} are the structural mass-, damping-, and stiffness matrix, respectively, and C_{jk} is the hydrostatic stiffness matrix. The hydrodynamic added mass $A_{\text{jk}}(\omega) = A_{\text{jk}}^{\infty} + a_{\text{jk}}(\omega)$ is here divided into a frequency-independent part A_{jk}^{∞} corresponding to the added mass at infinite frequency and a frequency-dependent term $a_{jk}(\omega)$. The same goes for the hydrodynamic damping $B_{\text{jk}}(\omega) = B_{\text{jk}}^{\infty} + b_{\text{jk}}(\omega)$. The notation ω here refers to angular frequency. The indices are defined according to the body-fixed coordinate system with $j = 1, 2, \ldots$ signifying surge, sway and so forth. The wave excitation force $q_j^{\text{exc}}(t)$ is a combination of the Froude-Krylov force and the diffraction force from solving the diffraction problem and is equivalent to the first order wave force $q_j^{(1)}(t)$. The displacement and its time derivatives are symbolized with $u_k(t)$, $\dot{u}_k(t)$ and $\ddot{u}_k(t)$ with t referring to time and τ representing the time lag in the convolution within the "memory" time t_{mem}. The hydrodynamic frequency-dependent added mass and damping found by solving the radiation problem are included in Eq. (1) through the retardation function $k_{jk}(t)$.

$$\begin{aligned} k_{\text{jk}}(t) &= \frac{1}{2\pi}\int_{-\infty}^{\infty} [b_{\text{jk}}(\omega) - i\omega a_{\text{jk}}(\omega)]e^{i\omega t}d\omega \\ &= \frac{2}{\pi}\int_0^{\infty} b_{\text{jk}}(\omega)\cos(\omega t)d\omega \end{aligned} \quad (2)$$

Here i is the imaginary unit. The retardation function $k_{jk}(t) = 0$ for $t < 0$ due to causality and $k_{jk}(t) \to 0$ for $t \to \infty$. The last term in Eq. (2) is derived by expanding the complex notation, removing the odd parts of the equation and applying the causality property. The frequency-independent damping B_{jk}^{∞} is zero since physically no waves are generated when the structure is oscillating at infinite frequency.

3.1.1. Modelling the first order wave load

The sea surface elevation consists of wind-generated waves approximated as a stationary and homogeneous random field. The wind-generated waves are described by a directional wave spectrum $S_\zeta(\omega, \theta)$ approximated as the product of the unidirectional wave spectrum $S_\zeta(\omega)$ and the directional spreading function $D_\zeta(\theta)$. The JONSWAP [23] wave spectrum in Eq. (3) is applied in the analysis.

$$S_\zeta(\omega) = \frac{\alpha g^2}{\omega^5}\exp\left(-1.25\frac{\omega_p^4}{\omega^4}\right)\gamma^{\exp\left(-\frac{(\omega-\omega_p)^2}{2\beta^2\omega_p^2}\right)} \quad (3)$$

The spectral parameters α and β are, for North Sea projects, often defined as $\alpha = 5.061H_s^2T_p^{-4}[1 - 0.287\ln(\gamma)]$ and $\beta = 0.07$ for $\omega \le \omega_p$ or $\beta = 0.09$ for $\omega > \omega_p$, respectively. g is the gravitational acceleration and the remaining variables are the peak angular frequency ω_p, the peakedness parameter γ and the significant wave height H_s. The directional spreading function is given in Eq. (4) where θ is the wave direction, θ_0 is the main wave direction, s is the spreading exponent and $\Gamma(\cdot)$ is the Gamma function.

$$D_\zeta(\theta) = \frac{1}{\sqrt{\pi}}\frac{\Gamma(\frac{s}{2}+1)}{\Gamma(\frac{s}{2}+\frac{1}{2})}\cos^s(\theta-\theta_0), \quad |\theta-\theta_0| \le \frac{\pi}{2} \quad (4)$$

The first order wave force is generated by Monte Carlo simulation using fast Fourier transformations (FFT) of the real part $\Re(\cdot)$ of the first order wave force transfer function $H_j^{(1)}(\omega_m, \theta_n)$ and the wave spectrum $S_\zeta(\omega_m)$.

$$\begin{aligned} q_j^{(1)}(\text{x, y, t}) = \Re\sum_{m=1}^{N_\omega}\sum_{n=1}^{N_\theta}\sqrt{2S_\zeta(\omega_m)D_\zeta(\theta_n)\Delta\omega_m\Delta\theta_n} \\ |H_j^{(1)}(\omega_m,\theta_n)|\exp\left[i\left(\varepsilon_{\text{nm}} + \varphi_{H_{\text{jnm}}^{(1)}}\right)\right] \\ \exp[i(\omega_m t - k_m x\cos(\theta_n) - k_m y\sin(\theta_n))] \end{aligned} \quad (5)$$

Where k_m is the wave number, ε_{nm} is the random phase angle and $\varphi_{H_{\text{jnm}}^{(1)}}$ is the phase angle.

The JONSWAP wave spectrum is used to describe the wave elevation with the parameters listed in Table 4. These parameters represents the preliminary wave condition at the Bjørnafjord for a 100-year return period [18]. The main wave direction follows the compass notations illustrated to the right in Fig. 2.

The hydrodynamic properties of the pontoon are found using the Boundary Element Method software Wadam [24]. With the extreme wave conditions located inside the Bjørnafjord the design wave height and wave period are still relatively small in comparison to the pontoon dimensions. For these specific wave conditions and pontoon geometry the structure is classified as a large structure with mainly diffraction loads being important. Utilizing the concept of double-symmetry the panel model used is one quarter of the pontoon. The panel model is given a general mesh size of 0.4 m resulting in a total of 5450 panel elements. The wave directions used are going from 90° to 180° with a 5°

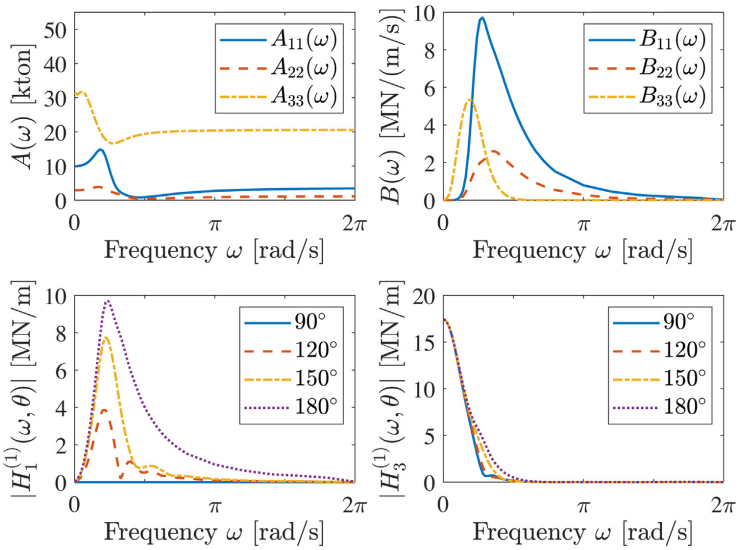

Fig. 3. Hydrodynamic coefficients following the body-fixed coordinate system of the pontoon with wave direction notation according to Fig. 2, i.e. waves from 90° and 180° follow sway and surge in the body-fixed coordinate system, respectively.

resolution following the notation in Fig. 2. Similarly the wave frequencies are between $2\pi/1000$ to 6π rad/s with varying frequency step (from $\Delta\omega = 2\pi/100$ at the lowest frequencies, to $\Delta\omega = 2\pi$ at the highest frequencies) in order to represent the hydrodynamic coefficients sufficiently. Fig. 3 illustrates the hydrodynamic properties of the pontoon. Noticeable information from Fig. 3 is the variation in the first order wave force transfer function for heave $|H_3^{(1)}(\omega, \theta)|$ within the frequency range of the wave spectrum for different wave directions.

In the hydrodynamic analysis of the pontoon the stiffness of the bridge superstructure is not taken into account. The solution of the classic radiation problem and diffraction problem does not depend on the pontoon stiffness and will not affect the hydrodynamic coefficients or the first order wave load transfer function. The first order motion transfer function, however, is affected but is not used in the estimation of the wave loads or the general response of the bridge. Instead the stiffness of the bridge superstructure is taken into account in the time domain analysis carried out in SIMO-RIFLEX. In other words, here the hydro-elasticity is only influencing the motions and responses, not the hydrodynamic coefficients in the model. The influence on motions may become more important when considering second order loads, but that is out of the scope of the present paper.

The option of modelling the wave loads as functions of spatial coordinates is built into the code. However, the correlation of the wave elevation at the different pontoon locations is significantly influenced by the irregular behaviour and the wave spreading. For short-crested beam sea the correlation is insignificant as pointed out by Kvåle et al. [25]. The almost non-existing correlation suggests that the wave forces acting on the pontoons could instead have been modelled as 21 independent wave loads.

In practice, the relative dimensions of the pontoons compared to the distance between them will govern whether the interaction effects should be accounted for or not. A simple estimation for hydrodynamic interaction between two ships is described in Xiang [26]. Based on this simplified estimation the interaction effects are assumed to be negligible for the present case study. Other studies have been made on floating bridges accounting for the hydrodynamic interaction effects such as Xiang et al. [27] and Seif and Inoue [28].

3.1.2. Tidal variation

The tidal variation is ± 0.75 m from the mean sea level. An expected increase in the mean sea level of 0.8 m is expected in the future due to climate change [29]. Any effects of the tidal variations are assumed to be a static effect and for this reason is neglected in the present study.

3.1.3. Note on using single equivalent beams

Both the bridge girder and the connection between the bridge girder and each pontoon are modelled as equivalent single beams with the cross-section properties listed in Table 1. When extracting the internal forces in the post-processing the effect of local stresses is neglected. For instance the stresses in the weld between the bridge girder and each column is not considered when calculating the stresses in the bridge girder.

3.1.4. Structural damping

In the numerical model the structural damping is applied globally using Rayleigh damping. The mass and stiffness proportional damping coefficients are 0.01208 and 0.03061, respectively, resulting in a damping ratio between 0.02 and 0.03 within the frequency range of the wave spectrum. With a damping ratio of less than 0.02 for standard civil engineering structures the chosen damping ratio is on the un-conservative side. However, given the simplifications already listed, the present study is not focused on the correct modelling of the bridge but rather on the sensitivity of the extreme response towards the short-crested sea parameters. Furthermore, the choice of the increased damping ratio can be argued by the exclusion of other damping effects such as the viscous drag on the pontoons and the aerodynamic damping from wind. For instance, Wang et al. [30] showed that for a floating multi-span suspension bridge the aerodynamic damping from the wind significantly dampened the wave-induced response.

In the present study the Rayleigh damping applied with the mentioned coefficients is furthermore of low influence to the response due

to the large amount of potential hydrodynamic damping stemming from the pontoons.

3.1.5. Solution procedures

The theory of the FEM is well established and hence only a general description of the solution procedures are given in the current section. For more details, the reader is referred to [20,31–33]. The solution $u(t)$ to the global system, i.e. the response time history, is first found based on a Newmark time step integration procedure and a Newton-Raphson iteration within each time step. The internal forces and moments at each time step are then found using the theory of virtual work using the global displacements and rotations at the end nodes of each individual beam element in the system together with the stress-strain relationships and the element interpolation functions. As an example, the internal weak axis bending moment M_y is found through the following integration over the initial element length L_0.

$$M_y = \int_{L_0} N''^{T}_{z,xx} \mathrm{EI}_y \kappa_y \mathrm{d}x \tag{6}$$

Where $N''^{T}_{z,xx}$ is the transpose of the vector of second derivatives with respect to the longitudinal direction x of the cubic interpolation functions for the transverse displacement z for a beam element. The remaining quantities κ_y and EI_y refer to the curvature and the bending stiffness around the y-axis, respectively.

Static equilibrium is obtained using an incremental loading of the static forces in the system. At each incremental step the Newton-Raphson iterative procedure is used to find convergence [20].

For solving the standard eigenvalue problem SIMO-RIFLEX uses the iterative Lanczos Method. The build-in procedure makes use of the hydrostatic stiffness and the hydrodynamic added mass at infinite frequency for the pontoons in the solution. Table 3 lists a manual pseudo-procedure used in order to take into account the frequency-dependent added mass in the solution.

Stability of the time-domain solution is obtained by specifying a ramping time of 10 s and a time step of 0.05 s based on an initial convergence study.

3.2. Parametric study

A parametric study is carried out in order to investigate the sensitivity of the response to the different naturally occurring spreading exponents and main wave directions.

3.2.1. Load cases for short-crested sea

A total of 12 load cases are specified for the parametric study listed in Table 4. They are made up of two main groups with different spreading exponents for normal occurring short-crested sea. For each group the main wave direction is changed. Due to a strong linear relationship between the response and the wave height a constant significant wave height is specified in the study. The peak period of the wave spectrum is also kept constant in the current study, although Larssen et al. [34] has shown that the peak period has a significant effect on the probability of failure for a curved submerged floating tube bridge (SFTB). While the significance of the peak period for the response most probably is transferable to a floating pontoon bridge the parameter has been kept constant due to time considerations.

Table 3
Manual pseudo procedure for solving the standard eigenvalue problem when accounting for frequency-dependent added mass.

INPUT N, $A(\omega)$, tolerance
Solve $[K - \omega^2(M + A^{\infty})]\psi = 0$
Store the first N natural angular frequencies as ω_n
FOR n = 1 to N
  $\omega_{out} = \omega_n$
  diff = tolerance + 1
  WHILE diff > tolerance
$\omega_{in} = \omega_{out}$
Solve $[K - \omega^2(M + A(\omega_{\mathrm{in}}))]\psi = 0$
Store the n'th natural angular frequency as ω_{out}
diff = $|\omega_{\mathrm{in}} - \omega_{\mathrm{out}}|$
  END
  Store ω_{out} as ω_n^*
END

Table 4
Load cases used in the parametric study. First order wave loads are applied with the chosen JONSWAP parameters H_s = 3.0 m, T_p = 6.0 s and γ = 3.3 based on the wave conditions at the Bjørnafjord for a 100-year return period [18].

Load case	Spreading	Wave direction	Load case	Spreading	Wave direction
LC1.1	2	90°	LC2.1	10	90°
LC1.2	2	95°	LC2.2	10	95°
LC1.3	2	100°	LC2.3	10	100°
LC1.4	2	105°	LC2.4	10	105°
LC1.5	2	120°	LC2.5	10	120°
LC1.6	2	150°	LC2.6	10	150°

3.2.2. Estimating Von Mises stress in bridge girder

From the global analysis only internal forces are extracted from the numerical model. In the post-processing of the results the internal forces are used as input to calculate the Von Mises stress $\sigma_v(t)$ in the bridge girder. Fig. 4 illustrates the basic assumptions made in order to estimate the Von Mises stress. One such assumption is the shear forces and torsional moments being divided equally among the two boxes in the twin-box cross-section. The second assumption is that the shear flow from the torsional force follows the contour of each box cross-section. This assumption is based on Damkilde [35] stating that the torsional shear flow is constant over a closed thin-walled cross-section. With the assumed distribution of the internal forces Eq. (7) is used to calculate the Von Mises stress at each time step t.

$$\sigma_v(t) = \sqrt{\sigma_{xx}^2(t) + 3(\tau_{xy}(t) \pm \tau_{xz}(t) \pm \tau_{xx}(t))^2} \tag{7}$$

Here $\sigma_{xx}(t)$ is the normal stress, $\tau_{xy}(t)$ and $\tau_{xz}(t)$ are the shear stress from the horizontal and vertical shear force $S_y(t)$ and $S_z(t)$, respectively. The torsional shear stress $\tau_{xx}(t)$ is associated with the torsional moment $M_x(t)$. The sign convention used depends on the direction of the shear flow as illustrated in Fig. 4.

The normal stress is found using Eq. (8) with the internal forces being the effective tension $T_e(t)$, the weak axis bending moment $M_y(t)$ and the strong axis bending moment $M_z(t)$. The total cross-sectional area of the twin-box cross-section is given by A_x and the notations y and z are the distance between the neutral axes of the twin-box cross-section and the point in question. The second moment of area I_y and I_z of the twin-box girder are around the two neutral axes indicated by the index.

$$\sigma_{xx}(t) = \frac{T_e(t)}{A_x} + \frac{M_y(t)z}{I_y} - \frac{M_z(t)y}{I_z} \tag{8}$$

The shear stresses $\tau_{xy}(t)$ and $\tau_{xz}(t)$ in the local y and z direction, respectively, are found using Eqs. (9) and (10) for points located y_d or z_d from the neutral axes. In the case of calculating $\tau_{xz}(t)$ at the point z_d from the neutral axis $\bar{A}$ is the area of the cross-section from the point to the top of the box as illustrated in Fig. 4. Similarly $\bar{z}$ is the centroid of that given area measured from the neutral axis. The torsional shear stress $\tau_{xx}(t)$ is given by Eq. (11) with t_w being the thickness of the girder wall at the point of interest and A_c is the enclosed area of a single box girder.

$$\tau_{xy}(t) = \frac{S_y(t)}{2} \frac{\bar{A}_y \bar{y}}{I_z t_w} \tag{9}$$

$$\tau_{xz}(t) = \frac{S_z(t)}{2} \frac{\bar{A}_z \bar{z}}{I_y t_w} \tag{10}$$

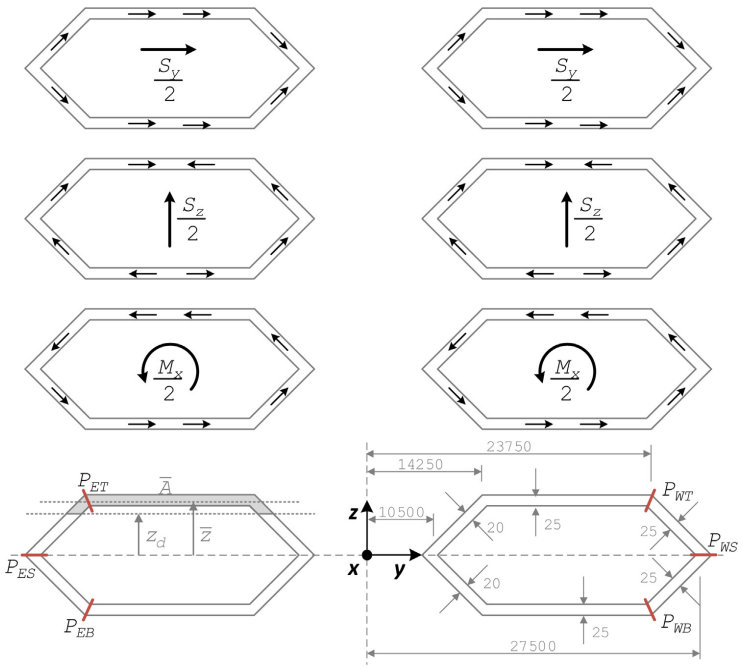

Fig. 4. Bridge girder cross-section with critical points and assumed stress distribution for calculating cross-sectional stresses. All measurements are in mm.

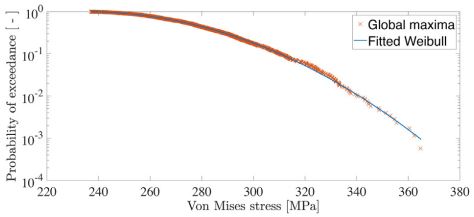

Fig. 5. Fit of a Weibull distribution to the global maxima Von Mises stress in point P_{ET} at AX23 for LC1.1 from a single 3-h realization.

$$\tau_{xx}(t) = \frac{M_x(t)}{2}\frac{1}{2A_c t_w} \tag{11}$$

The six critical points in the bridge girder cross-section are P_{WT}, P_{WS}, P_{WB}, P_{ET}, P_{ES} and P_{EB} with the first index being E or W for eastern or western box. Similarly the second index is T, S or B short for top, side or bottom. The locations of the six critical points are shown in Fig. 4.

3.2.3. Extreme response prediction

Extreme response prediction of a structural system is dependent on the characteristics of the stochastic load and the (non)-linearity of the structural system. With only first order Gaussian waves acting on a linear structural system, the structural response can be considered Gaussian in nature with the local maxima of the time series following a Rice distribution (Rayleigh distribution for narrow-banded processes) and the largest maxima for several statistically independent realizations will hence follow a Gumbel distribution asymptotically. An initial investigation has been conducted with several regular wave scenarios with changing wave height in order to see if the structural response is linear. Even though SIMO-RIFLEX include non-linear behaviour such as geometric stiffness in the solution algorithm, the relationship between the wave height and the dynamic structural response was found to be linear. It then follows that the extreme response should follow a Gumbel distribution.

The extreme response is estimated using a short-term method according to recommendations given in Spidsøe and Karunakaran [36]. For a single realization of the response a Weibull distribution is fitted to the global maxima as recommended by Farnes and Moan [37] using the method of matching statistical moments. In order to predict the extreme response from extrapolation of the Weibull distribution a good fit to the global maxima in the upper tail is necessary. This is generally achieved using a threshold to avoid over representation of small maxima in the fitting procedure. The threshold is an empirical value and as pointed out by Fu et al. [38] can have a significant effect on the shape of the Weibull distribution. Using a threshold equal to the mean value of the time series the Weibull fits well to the global maxima as illustrated in Fig. 5.

Based on the number of global maxima N_m in the time series and the Weibull location parameter δ, scaling factor λ and shape factor υ an estimate of the *extrapolated extreme* μ_{X_e} is calculated.

$$\mu_{X_e} = \delta + \lambda\left[(\ln(N_m))^{\frac{1}{\upsilon}} + \frac{0.57722}{\upsilon}(\ln(N_m))^{\frac{1-\upsilon}{\upsilon}}\right] \tag{12}$$

Based on N_r realizations the *average extrapolated extreme* $\bar{\mu_{X_e}}$ and the corresponding standard deviation $\sigma_{\bar{X}_e}$ and coefficient of variation (c.o.v.) C_{X_e} are found.

$$\bar{\mu_{X_e}} = \frac{1}{N_r}\sum_{i=1}^{N_r}(\mu_{X_e})_i \tag{13}$$

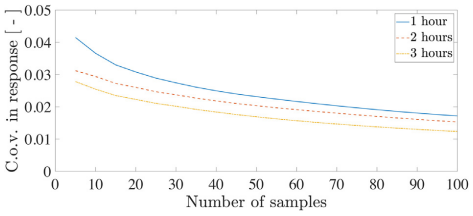

Fig. 6. C.o.v. of *average extrapolated extremes* vs simulation length and number of samples for Von Mises stress in point P_{ET} at AX23 for LC1.1.

$$\sigma_{\bar{X}_e} = \sqrt{\frac{1}{N_r - 1}\sum_{i=1}^{N_r}\left(\left(\mu_{X_e}\right)_i - \mu_{\bar{X}_e}\right)^2} \tag{14}$$

$$C_{X_e} = \frac{\sigma_{\bar{X}_e}}{\mu_{\bar{X}_e}} \tag{15}$$

For load case LC1.1 the largest *average extrapolated extreme* of the Von Mises stress is observed to be in point P_{ET} at axis AX23 on the bridge. Here a comparison of the c.o.v. of the *average extrapolated extreme* is performed for three sets of 100 realizations, each with the realization length of 1 h, 2 h and 3 h, respectively. In Fig. 6 the c.o.v. of the *average extrapolated extremes* is presented as a function of the realization length and the number of realizations. These results show that one will obtain a c.o.v. of less than 4% for even the shortest realization length using roughly 10 realizations. For a 3 h realization length 10 realizations give a c.o.v. of approximately 2.5% while 40 realizations give less than 2%. This is thought to be an acceptable level of accuracy. The Type I extreme value distributions obtained from the fitted Weibull parameters from 2 sets of 40 realizations are compared to the *sample extremes* as well as a Gumbel distribution fitted to the 100 *sample extremes* in Fig. 7. Based on the $-log(-log(\cdot))$ values of the cumulative distribution functions denoted with F_x the two Type I distributions based on 40 independent 3 h realizations both show a good fit and will be used in the following parametric study for each load case listed in Table 4.

4. Results and discussion

4.1. Modal properties

Table 5 lists the natural frequencies of the structure with modes 3–30 in the range of the 100-year wave spectrum applied in the parametric study. Many of the active natural periods are within 0.1 s of each other, making the floating bridge a complex structural system. Fig. 8 shows the transverse and vertical displacements of the corresponding modeshapes when accounting for the frequency-dependent added mass, which have a significant effect on the weak and strong axis bending moment in the bridge girder. With the structural system being strongly

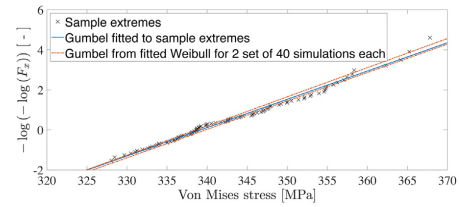

Fig. 7. Fit of *sample extreme* Von Mises stress in point P_{ET} at AX23 for LC1.1 to the Gumbel distribution. They are compared to two Gumbel distributions obtained from fitted Weibull distributions.

Table 5
Eigenvalues of the floating bridge structure when accounting for frequency-dependent added mass (ω_n^*) and when not (ω_n). The corresponding modeshapes are of the same shape with insignificant differences.

Mode n	ω_n [rad/s]	ω_n^* [rad/s]	Mode n	ω_n [rad/s]	ω_n^* [rad/s]
1	0.133	0.126	16	0.732	0.780
2	0.232	0.220	17	0.750	0.801
3	0.396	0.372	18	0.773	0.826
4	0.441	0.409	19	0.799	0.854
5	0.671	0.620	20	0.828	0.887
6	0.685	0.726	21	0.861	0.899
7	0.685	0.726	22	0.896	0.918
8	0.686	0.726	23	0.910	0.922
9	0.686	0.727	24	0.920	0.957
10	0.687	0.728	25	0.929	0.992
11	0.690	0.731	26	0.960	1.023
12	0.693	0.735	27	0.985	1.048
13	0.699	0.741	28	1.000	1.064
14	0.707	0.751	29	1.229	1.257
15	0.718	0.764	30	1.393	1.438

linear the response is expected to be a superposition of the mode shapes and the Von Mises stress will in turn be affected by the contributions from the bending moments to the normal stress at the critical points of the girder cross-section. It should be noted that the modeshapes when *not* accounting for the frequency-dependent added mass show the same shape with insignificant differences. The corresponding frequencies, however, are slightly different.

4.2. Parametric study

In the following sections the sensitivity towards the main wave direction and the spreading exponent is summarized for the transverse and vertical displacement response spectra, the extreme Von Mises stress and the correlation between the weak and strong axis bending moment.

4.2.1. Effect on displacement response spectra

Based on the time series of the transverse and vertical displacement at each axis the corresponding response spectra, $S_2(\omega)$ and $S_3(\omega)$ respectively, are found through a fast Fourier transformation (FFT) of the auto-correlation function of the said time series. This is done using WAFO [39] and the average of all 40 response spectra is used as the representative response spectrum for each load case. Although the response spectra are slightly different along the bridge the response spectra at the midspan illustrates the general effect at each pontoon. Figs. 9 and 10 show the changes in $S_2(\omega)$ and $S_3(\omega)$, respectively, towards the main wave direction and the spreading exponent for the midspan at AX12.

As a general observation, a low sensitivity in both response spectra towards the spreading exponent persists. The energy in $S_3(\omega)$ is only affected by the spreading exponent for main wave directions between 90° (beam sea) and 105°. Similarly, a low sensitivity towards the main wave direction is observed between beam sea and 105°. However, significant changes in $S_3(\omega)$ are observed for main wave directions larger than 105°.

Fig. 9 illustrates the changes in $S_3(\omega)$ for changing main wave direction and spreading exponent. Two main peaks are present corresponding to mode 21 and 22 of the structure (first peak) and the peak period T_p of the wave spectrum (second peak). Although a slight shift is observed for the first peak this is too small to conclude anything about the relationship with the modeshapes. The first peak is significantly larger than the second peak and no peak is visible around mode 29. Instead a significant increase in the spectra around mode 26 is present for 150° even though the transverse displacement of this said mode is almost non-existing for AX12.

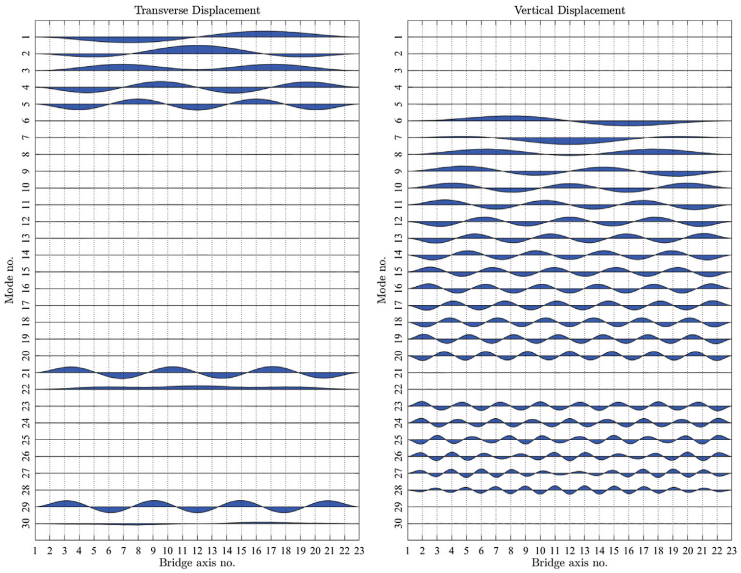

Fig. 8. Transverse and vertical displacement of the floating bridge modes based on exact added mass.

A low sensitivity in $S_3(\omega)$ towards the main wave directions between 90° and 150° is illustrated in Fig. 10. For these cases the spectra show a peak around mode 14 and 16 as well as at the peak corresponding to T_p and mode 28. A significant increase in the overall energy is observed for main wave directions 120° and 150° and especially for the most short-crested seas does the peak at T_p become more dominant. This behaviour is most likely related to the strong directional dependency in the first order wave force transfer function for heave $|H_3^{(1)}(\omega, \theta)|$ seen in Fig. 3. For frequencies between $2\pi/10$ and $2\pi/4$ rad/s corresponding to the frequencies within the applied wave spectrum the values for 150° are up to four times larger than the values for 90° (sway). In general, larger heave wave forces are present for directions closer to 180° (surge). A notable feature in $S_3(\omega)$ is the significant relative increase in the peak at T_p for a main wave direction of 150° and although the larger heave force explains the general energy increase the first order wave transfer function for heave at 150° is only twice that for

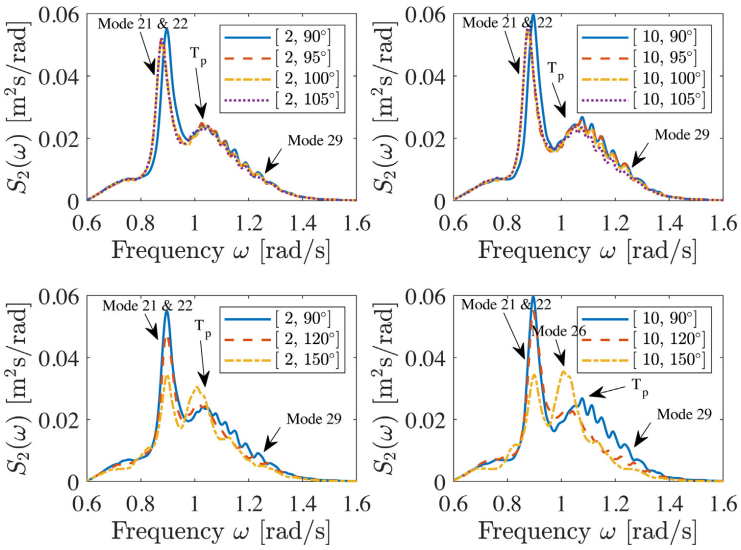

Fig. 9. Transverse response spectra of the bridge girder at the midspan AX12 for all load cases with different $[s, \theta_0]$ values.

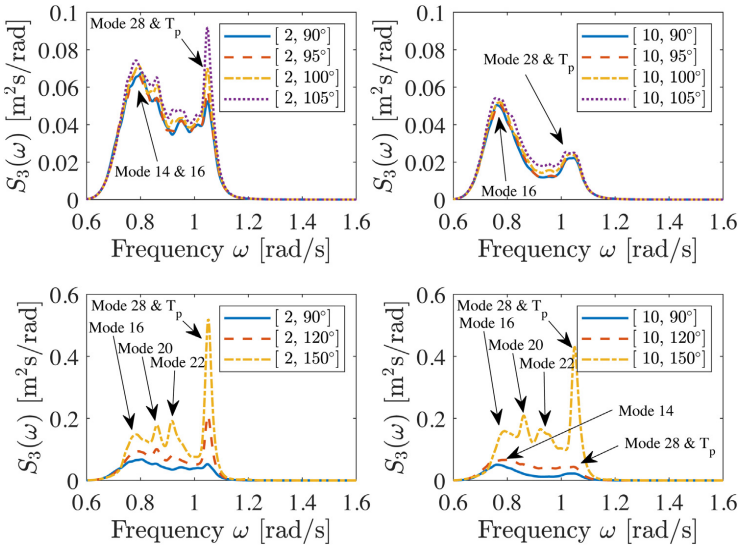

Fig. 10. Vertical response spectra of the bridge girder at the midspan AX12 for all load cases with different [s, θ_0] values.

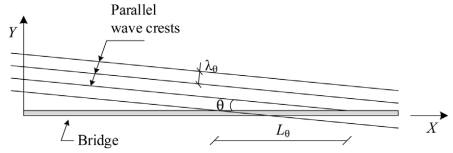

Fig. 11. Parallel wave crests propagating at an angle Θ from the normal of a straight bridge [40].

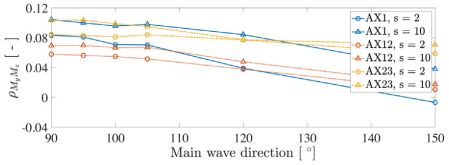

Fig. 12. Sensitivity in correlation of weak and strong axis bending moment to main wave direction and spreading exponent at specific points in the bridge.

heave at 90°. Remseth et al. [40] has described the principal effect of spacial resonance for a straight SFTB using regular long-crested waves at angles slightly different from beam sea. For a given regular wave with the frequency ω_8 corresponding to the natural frequency of the 8th mode of the SFTB propagating at a specific angle Θ to the bridge normal as shown in Fig. 11 the distance L_Θ between the wave crests hitting the SFTB coincide with the peaks of the 8th modeshape of the structure and thereby amplifying the resonance effect. This effect is thought to be present in $S_3(\omega)$ at the midspan of the floating bridge in the current study, although it is difficult to verify systematically due to the many closely spaced natural periods of the structure and the neglected damping in the procedure to obtain said natural periods. Exposing the structure to long-crested regular waves at different wave directions with a wave period corresponding to a specific modeshape might work for low modes but in this case study the relevant modes are between 19 and 30. Furthermore, the strong directional dependency in the first

Table 6
Largest *average extrapolated extreme* Von Mises stress and their corresponding location in the bridge girder

Load case	Axis	Point	Mean [MPa]	Std [MPa]	C.o.v. [%]
LC1.1	AX23	P_{ET}	371.9	4.1	1.1
LC1.2	AX23	P_{ET}	372.2	3.6	1.0
LC1.3	AX23	P_{ET}	374.0	3.7	1.0
LC1.4	AX23	P_{ET}	375.7	4.4	1.2
LC1.5	AX23	P_{ET}	383.3	5.6	1.5
LC1.6	AX23	P_{ET}	404.7	6.0	1.5
LC2.1	AX23	P_{ET}	364.9	4.0	1.1
LC2.2	AX23	P_{ET}	365.7	4.5	1.2
LC2.3	AX23	P_{ET}	366.3	3.4	0.9
LC2.4	AX23	P_{ET}	365.8	3.7	1.0
LC2.5	AX23	P_{ET}	373.2	6.0	1.6
LC2.6	AX23	P_{ET}	408.0	6.6	1.6

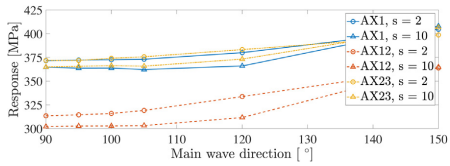

Fig. 13. Sensitivity in the *average extrapolated extreme* Von Mises stress in point P_{ET} towards the main wave direction and the spreading exponent.

order wave load transfer functions will add further uncertainty to the results.

4.2.2. Effect on bending moment correlation

The weak and strong axis bending moments are generally important factors in the design of floating bridges as pointed out by e.g. Leira and Langen [6]. For the current structure the correlation coefficient ρ_{MyMz} between the weak and strong axis bending moments is calculated for each realization within each load case listed in Table 4. The sensitivity

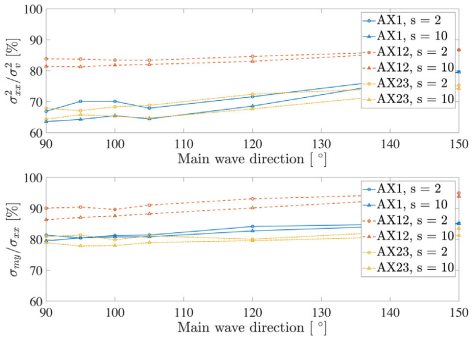

Fig. 14. Average contribution to *sample extreme* Von Mises stress at point P_{ET} (top) and the associated normal stress (bottom).

towards changes in main wave direction and spreading exponent for the average correlation coefficient at the midspan and each end of the bridge is shown in Fig. 12. The correlation coefficient remains within 10% and seem to depend slightly on changes of both main wave direction and spreading exponent, although for main wave direction 90° and up to 105° the sensitivity towards the main wave direction is insignificant.

4.2.3. Effect on extreme Von Mises stress

The Von Mises stress is evaluated at all six points shown in Fig. 4 and the value of the largest occurring *average extrapolated extreme* Von Mises stress for each load case is listed in Table 6 together with their corresponding location in the bridge. For all load cases the most critical point is in point P_{ET} at AX23 in the bridge. The sensitivity in the response at this location is illustrated in Fig. 13 for changing main wave direction and spreading exponent showing that the *average extrapolated extremes* are within 10% for all load cases, except at AX12 for main wave direction 150° which is 20% larger. A relatively low sensitivity towards the spreading exponent is observed, although larger values are found for the most short-crested load cases. Similarly the main wave direction only has a measurable effect on the response for 120° and up. The observation of a low sensitivity towards the spreading exponent is supported by other studies made by Langen and Sigbjörnsson [3] who investigated the effect of short-crested sea in the design of a floating pontoon bridge.

In general P_{ET} is found to be the most critical point in the cross-section for all load cases and at all axes along the bridge, except for AX20, AX21 and AX22 where P_{WT} is the most critical. Fig. 14 illustrates the average contributions to the *sample extreme* Von Mises stress in point P_{ET} at AX1, AX12 and AX23 for changing main wave directions and spreading exponents. The squared normal stress σ^2_{xx} is the main contributor to the squared Von Mises stress σ^2_v with at least 65% at the bridge abutments and up to 85% at the middle of the bridge. On average the largest contributor to the normal stress is the stress from the weak axis bending moment σ_{my}, which is responsible for roughly 80% of the normal stress at the two ends and up to 90% for the middle of the bridge.

5. Conclusion

A numerical study of the extreme wave-induced response for a long end-anchored floating bridge has been presented based on a short-term extreme method with a wave environment having a return period of 100 years.

The accuracy of the short-term extreme response method is investigated based on three sets of 100 realizations with realization lengths of 1 h, 2 h and 3 h, respectively. The coefficient of variation (c.o.v.) of the *average extrapolated extremes* from fitting Weibull distributions to realization maxima show clear dependency on both realization length and number of realizations. A chosen accuracy of less than 2% in the c.o.v. is achieved using 40 3-h realizations.

An extensive parametric study has been performed based on 40 3-h realizations for 12 different wave environments accounting for changing main wave direction and spreading exponent. A low sensitivity towards the spreading exponent is observed in the *average extrapolated extreme* Von Mises stress of the bridge girder and based on structural symmetry changes in the main wave direction are insignificant for directions within 15° from beam sea. The transverse and vertical response spectra show a similar behaviour, except for main wave directions more than 15° from beam sea where a significant change is observed. This effect is thought to be linked to spatial resonance described by Remseth et al. [40], although, the high structural complexity with several important natural periods within 0.1 s of each other makes it difficult to verify.

Acknowledgements

This research was carried out with financial support from the Norwegian Public Roads Administration. The authors greatly acknowledge this support. We would also like to thank our colleague Ping Fu for her assistance in applying the extreme response prediction method used in the paper.

References

[1] I. Holand, R. Sigbjörnsson, I. Langen, Dynamic analysis of a curved floating bridge, IABSE Proc. 1-16 (1977) P-5/77.
[2] R. Sigbjörnsson, Stochastic theory of wave loading processes, Eng. Struct. 1 (2) (1979) 58–64, https://doi.org/10.1016/0141-0296(79)90014-2.
[3] I. Langen, R. Sigbjörnsson, On stochastic dynamics of floating bridges, Eng. Struct. 2 (4) (1980) 209–216, https://doi.org/10.1016/0141-0296(80)90002-4.
[4] I. Langen, Probabilistic methods for dynamic analysis of floating bridges, Nor. Marit. Res. 11 (1) (1983) 2–15.
[5] B.J. Leira, Probabilistic Design – An Application to Floating Bridges, Tech. Rep., SINTEF, (1983).
[6] B.J. Leira, I. Langen, On probabilistic design of a concrete floating bridge, Nordic Concr. Res. 3 (1984) 140–166.
[7] L.E. Borgman, Statistical models for ocean waves and wave forces, Advances in Hydroscience vol. 8, Elsevier, 1972, pp. 139–181, https://doi.org/10.1016/B978-0-12-021808-0.50008-5.
[8] B.L. Hutchison, Impulse response techniques for floating bridges and breakwaters subject to short-crested seas, Mar. Technol. 21 (3) (1984) 270–276.
[9] B. Villoria, Floating bridge technology – prediction of extreme environmental load effects, Proceedings of the 35th International Conference on Ocean, Offshore and Arctic Engineering, ASME, 2016, pp. 1–8, , https://doi.org/10.1115/OMAE2016-54433.
[10] T. Moan, Z. Gao, E. Ayala-Uraga, Uncertainty of wave-induced response of marine structures due to long-term variation of extratropical wave conditions, Mar. Struct. 18 (4) (2005) 359–382, https://doi.org/10.1016/j.marstruc.2005.11.001.
[11] E.M. Bitner-Gregersen, K.C. Ewans, M.C. Johnson, Some uncertainties associated with wind and wave description and their importance for engineering applications, Ocean Eng. 86 (2014) 11–25, https://doi.org/10.1016/j.oceaneng.2014.05.002.
[12] K.A. Kvåle, O. Øiseth, Characterization of the Wave Field Around an Existing End-Supported Pontoon Bridge from Simulated Data, Springer International Publishing, 2019, pp. 345–359, https://doi.org/10.1007/978-3-319-78187-7_26.
[13] F.-I.G. Giske, K.A. Kvåle, B.J. Leira, O. Øiseth, Long-term extreme response analysis of a long-span pontoon bridge, Mar. Struct. 58 (2018) 154–171, https://doi.org/10.1016/j.marstruc.2017.11.010.
[14] F.-I.G. Giske, B.J. Leira, O. Øiseth, Long-term extreme response analysis of marine structures using inverse SORM, J. Offshore Mech. Arctic Eng. 140 (5) (2018) 1–8, https://doi.org/10.1115/1.4039718.
[15] O. Øiseth, A. Rönnquist, A. Naess, R. Sigbjörnsson, Estimation of extreme response of floating bridges by Monte Carlo simulation, Proceedings of the 9th International Conference on Structural Dynamics, EURODYN (2014) 2905–2912.
[16] A. Naess, O. Gaidai, Estimation of extreme values from sampled time series, Struct. Saf. 31 (4) (2009) 325–334, https://doi.org/10.1016/j.strusafe.2008.06.021.
[17] Y. Xu, O. Øiseth, A. Naess, T. Moan, Prediction of long-term extreme load effects due to wind for cable-supported bridges using time-domain simulations, Eng. Struct. 148 (2017) 239–253, https://doi.org/10.1016/j.engstruct.2017.06.051.
[18] Statens Vegvesen, Curved Bridge – Navigation Channel in South, Oslo, Norway, (2016) Report No. NOT-KTEKA-021.
[19] SINTEF Ocean, SIMO 4.10.0 Theory Manual, Trondheim, Norway, (2017).
[20] SINTEF Ocean, RIFLEX 4.10.0 Theory Manual, Trondheim, Norway, (2017).

[21] W.E. Cummins, The Impulse Response Function and Ship Motions, Washington DC, USA, (1962) Report No. DTMB-1661.
[22] L.J. Tick, Differential equations with frequency-dependent coefficients, J. Ship Res. 3 (1959) 45–46.
[23] K. Hasselmann, T.P. Barnett, E. Bouws, H. Carlson, D.E. Cartwright, K. Enke, J.A. Ewing, H. Gienapp, D.E. Hasselmann, P. Kruseman, A. Meerburg, P. Muller, D.J. Olbers, K. Richter, W. Sell, H. Walden, Measurements of wind-wave growth and swell decay during the Joint North Sea Wave Project (JONSWAP), Dtsch Hydrogr. Z. 8 (12) (1973).
[24] D.N.V. Wadam, Wave Analysis by Diffraction and Morison Theory, SESAM User Manual, Høvik, Norway, (2014) Report no. 94-7100.
[25] K.A. Kvåle, R. Sigbjörnsson, O. Øiseth, Modelling the stochastic dynamic behaviour of a pontoon bridge: a case study, Comput. Struct. 165 (2016) 123–135, https://doi.org/10.1016/j.compstruc.2015.12.009.
[26] X. Xiang, Maneuvering of Two Interacting Ships in Waves (Ph.D. thesis), Norwegian University of Science and Technology, 2012, https://brage.bibsys.no/xmlui/handle/11250/238361.
[27] X. Xiang, T. Viuff, B. Leira, O. Øiseth, Impact of hydrodynamic interaction between pontoons on global responses of a long floating bridge under wind waves, Proceedings of the 37th International Conference on Ocean, Offshore and Arctic Engineering (2018) 1–11, https://doi.org/10.1115/OMAE2018-78625.
[28] M.S. Seif, Y. Inoue, Dynamic analysis of floating bridges, Mar. Struct. 11 (1–2) (1998) 29–46, https://doi.org/10.1016/S0951-8339(97)00012-9.
[29] Statens Vegvesen, Design Basis, Oslo, Norway, (2016) Report No. RAP-GEN-001.
[30] J. Wang, E. Cheynet, J. Snæbjörnsson, J.B. Jakobsen, Coupled aerodynamic and hydrodynamic response of a long span bridge suspended from floating towers, J. Wind Eng. Ind. Aerodyn. 177 (2018) 19–31, https://doi.org/10.1016/j.jweia.2018.03.024.
[31] A. Naess, T. Moan, Stochastic Dynamics of Marine Structures, Cambridge University Press, 2013.
[32] R.D. Cook, D.S. Malkus, M.E. Plesha, R.J. Witt, Concepts and Applications of Finite Element Analysis, John Wiley & Sons, Inc., 2002.
[33] J. Fish, T. Belytschko, A First Course in Finite Elements, John Wiley & Sons, Ltd., 2007.
[34] R.M. Larssen, S.N. Remseth, B.J. Leira, Parameter sensitivity of predicted extreme response for a submerged tubular bridge, Proceedings of the 3rd symposium on strait crossings, Balkema Publishers, Rotterdam, 1994, pp. 607–613.
[35] L. Damkilde, Stress and Stiffness Analysis of Beam-Sections, Technical University of Denmark, 2000.
[36] N. Spidsøe, D.N. Karunakaran, Nonlinear dynamic behaviour of jack-up platforms, Mar. Struct. 9 (1) (1996) 71–100, https://doi.org/10.1016/0951-8339(95)00005-Q.
[37] K.-A. Farnes, T. Moan, Extreme dynamic, non-linear response of fixed platforms using a complete long-term approach, Appl. Ocean Res. 15 (6) (1993) 317–326, https://doi.org/10.1016/0141-1187(93)90001-E.
[38] P. Fu, B.J. Leira, D. Myrhaug, Assessment of Methods for Short-Term Extreme Value Analysis of Riser Collision, (2018), pp. 1–9, https://doi.org/10.1115/OMAE2018-78318.
[39] P. Brodtkorb, P. Johannesson, G. Lindgren, I. Rychlik, J. Rydén, E. Sjö, WAFO – a matlab toolbox for the analysis of random waves and loads, Proc. 10'th Int. Offshore and Polar Eng. Conf., ISOPE, Seattle, USA (2000) 343–350.
[40] S.N. Remseth, B.J. Leira, K.M. Okstad, K.M. Mathisen, T. Haukås, Dynamic response and fluid/structure interaction of submerged floating tunnels, Comput. Struct. 72 (4) (1999) 659–685, https://doi.org/10.1016/S0045-7949(98)00329-0.

Paper 2

Thomas Viuff, Xu Xiang, Bernt Johan Leira and Ole Øiseth

"Software-to-software comparison of end-anchored floating bridge global analysis"

Bridge Engineering, vol. 25(5), pp. 04020022, March 2020.

Software-to-Software Comparison of End-Anchored Floating Bridge Global Analysis

Thomas Viuff[1,*], Xu Xiang[2], Bernt Johan Leira[3], and Ole Øiseth[4]

[1]Department of Marine Technology, Norwegian University of Science and Technology, N-7491 Trondheim, Norway
[2]Norwegian Public Roads Administration, N-0667 Oslo, Norway
[3]Department of Marine Technology, Norwegian University of Science and Technology, N-7491 Trondheim, Norway
[4]Department of Structural Engineering, Norwegian University of Science and Technology, N-7491 Trondheim, Norway
[*]Corresponding author. Email address: thomas.h.viuff@ntnu.no

ABSTRACT

Several computer programs exist to handle general multi-purpose offshore structural analysis of slender structures subjected to wave loading, although, they have not been developed with the specific purpose of floating bridge global analysis in mind. Due to the inherent complexity of a floating bridge structure, this poses a valid concern regarding the accuracy in the calculated response. Normally, the intended computer program is validated against experiments but in the case of extremely long floating bridges the size limitations of existing ocean basins necessitates the use of hybrid testing where the computer program is a part of the method to obtain the true value from the experiments. It is, therefore, crucial to get an overview of how sensitive the numerical results are to inaccurate user inputs, approximations introduced in the theory and the software implementation of the theory as well as possible settings that the user does not have access to. An extensive comparison between two commonly used commercial computer programs in the offshore industry is presented in the present paper for a global analysis of a floating pontoon bridge concept. The comparison includes modal properties as well as deterministic and stochastic structural response due to wave loads based on coupled hydro-elastic time domain simulations. First and second order wave loads are included in the comparison as well as viscous drag. The study indicates a reasonable agreement in the response acquired by the two computer programs and highlights consequences of differences in some of the input parameters.

INTRODUCTION

The common practice when designing offshore structures is to validate the numerical analysis with experiments obtained from tests carried out in e.g. an ocean basin facility. In some cases, however, the full-scale dimensions of the structure are of such proportions that it conflicts with the size limitations of the relevant test facilities and requirements in accuracy regarding the model scale. Due to the scale of the model, a so-called hybrid test, see e.g. Stansberg et al. (2002), is usually carried out where only parts of the model are tested in the ocean basin and used for calibration of the relevant computer program. In turn, the validated computer program is used to predict the full-scale response of the entire structure. This highlights the necessity of software-to-software comparison since the software is a part of the tests to obtain the true value. For the engineers who will plan such tests, the software-to-software comparison is of uttermost importance for their informed choice and quality control purposes as well as to have an estimate on the uncertainties related to the numerical results.

In Norway the Norwegian Public Roads Administration (NPRA) is working on establishing fixed links across the many deep and wide fjords along the E39 Coastal Highway Route. The extreme depths of up to 1,300 m and widths of up to 6,000 m makes the project particularly challenging. One of the proposed structural concepts to cross the fjords is an end-anchored floating pontoon bridge described in the present paper. Due to the extreme length requirements of the bridge the validation of the numerical models fall under the hybrid test procedure mentioned above. Experimental results exist for a shorter but similar floating bridge structure from when the first floating bridges were constructed in Norway in the early 1990s and have been used as a first step in the validation of existing computer programs, see Løken and Oftedal (1990) and Xiang and Løken (2019). However, the effect of the increased slenderness of the proposed floating bridge structure is not well understood and renders the validation towards the previous experiments insufficient. Furthermore, with several numerical studies conducted in the last five years with respect to end-anchored floating pontoon bridges related to the E39 Coastal Highway Route Project, see e.g. Xiang et al. (2017); Fu et al. (2017); Cheng et al. (2018a,b,c), either in the coupled SIMO (SINTEF Ocean, 2017b) and RIFLEX (SINTEF Ocean, 2017a) program, further on referred to as SIMO-RIFLEX, or OrcaFlex (Orcina, 2019) focusing on the stochastic

response from wind and waves, there is a significant interest in how well results obtained by the two different computer programs compare.

The use of software-to-software comparison is a necessary option when experimental data is scarce due to the high financial costs, see e.g. Karimirad et al. (2011), Sørum et al. (2017) or Robertson et al. (2014) on validation of numerical software applied to offshore floating wind turbines. Robertson et al. (2014) did an extensive comparison of several well-known computer programs within ocean engineering, including SIMO-RIFLEX. Less available literature describes comparison of computer programs with regard to long floating bridges. Statens Vegvesen (2016) described the general design of a floating bridge structure including a comparison of the dynamic wind response between OrcaFlex and an in-house software. The present paper is a continuation of a previous paper (Viuff et al., 2018) with preliminary findings on the software-to-software comparison for the global analysis of a similar end-anchored floating pontoon bridge concept. In the present paper the comparison is more rigorously carried out and with more attention to modelling details. In our experience, different software and different users can provide results with large discrepancies, which is important when assessing the reliability of large and innovative bridge concepts. The differences will diminish with the development of special software, where all approximations and settings unavailable to the user are implemented while keeping these special structures in mind. We have made our best effort to compensate for the differences in the implementation of the theory in the two computer programs, but there are still significant differences, which illustrates the challenges that need to be solved when designing new and innovative floating bridges. Focusing on a software-to-software comparison of the two computer programs, the aim of the paper is two-fold: 1) Contribute to the knowledge of the uncertainty associated with the calculated response obtained by application of commercial software for analysis of end-anchored floating pontoon bridges. 2) Highlight the structural complexity of the end-anchored floating pontoon bridge concept and the inherent sensitivity to certain input parameters related to the numerical modelling. The comparison is performed using OrcaFlex (Orcina, 2019) version 10.2c and SIMO-RIFLEX (SINTEF Ocean, 2017b,a) version 4.10.0.

THE BJØRNAFJORD FLOATING BRIDGE CONCEPT

The end-anchored floating pontoon bridge illustrated in Fig. 1 is one of the main concepts evaluated by NRPA for crossing the Bjørnafjord in western Norway. The floating bridge consists of a single 230 m high tower in the southern end connected to the bridge girder with 4x20 pre-tensioned stay-cables. North of the tower the bridge girder is resting on columns connected to 19 floating pontoons. The bridge has a radius of curvature in the horizontal plane of 5,000 m, resulting in a total road line of 4,602 m going from south to north. The geometry and structural properties of the bridge is based on Statens Vegvesen (2016) and only the most relevant information is given in this section. The bridge girder consists of a twin-box cross-section modelled as a single equivalent beam with properties listed in Tab. 1. The road line at the high bridge part from AX1 to AX3 is divided into five consecutive segments of 220, 100, 100, 100, 330 and 10 m with cross-section H1, H2, H3, H2, H1 and S1, respectively. Similarly at the low bridge part from AX3 to AX22, the 197 m road line between each pontoon and between the last pontoon and the northern end is divided into three consecutive sections of 25, 147 and 25 m with cross-section S1, F1 and S1, respectively. The distribution of the cross-sections along the bridge girder is illustrated in Fig. 1.

The vertical position of the bridge girder is mainly 15 m along the low bridge part but at the tower the freeboard is roughly increased to 55 m to allow for ship traffic. Along the bridge at each pontoon, two columns are positioned perpendicular to the bridge axis consisting of circular cross-sections of varying height.

The same pontoon geometry is used for all 19 pontoons. The geometry is made up of a rectangular box in the middle, two half circle cylinders at each end and an extended bottom plate, which in the following will be referred to as a heave plate following the terminology from the offshore wind turbine industry. The pontoons are 14.5 m high, 28 m wide and 68 m long, and the heave plate is 5 m wide and 0.6 m high. All pontoons are oriented with surge along the global x-axis and sway following the global y-axis. Figure 2 illustrates the coordinate definitions and the wave directions used in the model and Tab. 2 lists the properties of the pontoon without ballast. Ballast between roughly 750 and 2,500 ton is added to the different pontoons in order to keep them all at the same draft of 10.5 m. The application of a heave plate on the pontoons is not a new concept but has been applied for many years in the offshore industry where it has been used to change the mass and damping properties of structures such as floating wind turbines (Tao and Cai, 2004) or floating production storage and offloading (FPSO) units (Shao et al., 2016). The heave plate has been proposed for this bridge concept and Xiang et al. (2017) has shown that a significant reduction in the global response can be obtained from this change in the pontoon geometry.

METHODOLOGY

The numerical models created in both computer programs are based on many of the same assumptions and the

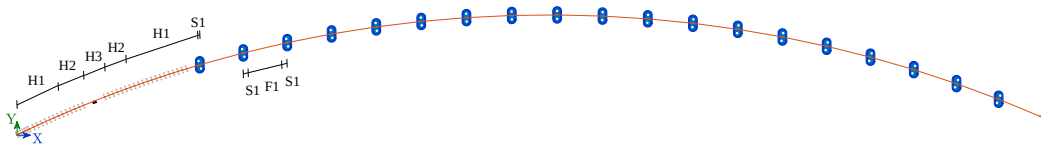

(a) View from above

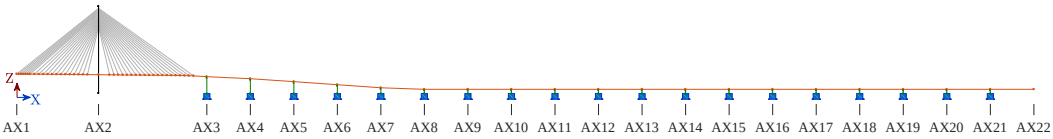

(b) View from side

Fig. 1. End-anchored horizontally curved floating pontoon bridge. (a) View from above. (b) View from the side.

TABLE 1. Properties of bridge girder cross-sections. The bending stiffness about the weak and strong girder axis is denoted by EI_y and EI_z, respectively. The torsional stiffness and the radius of gyration are denoted by GI_x and r_x respectively.

Property	Unit	H1	H2	H3	S1	F1
Mass	[ton/m]	2.40E+01	2.91E+01	3.31E+01	3.18E+01	2.67E+01
r_x	[m]	1.66E+01	1.73E+01	1.76E+01	1.82E+01	1.76E+01
EA	[kN]	3.06E+08	4.41E+08	5.51E+08	5.25E+08	3.89E+08
EI_y	[kNm^2]	1.28E+09	1.98E+09	2.48E+09	3.85E+09	2.77E+09
EI_z	[kN^2]	1.16E+11	1.70E+11	2.12E+11	2.18E+11	1.55E+11
GI_x	[kN^2/rad]	1.42E+09	1.98E+09	2.48E+09	3.70E+09	2.90E+09

Source: Data from Statens Vegvesen (2017).

same theoretical background. The present paper describes the general procedure for both computer programs and seek to point out any existing differences between them.

Numerical Model of the Floating Bridge

The structure is modelled using beam and bar elements in both computer programs and the pontoons are modelled as 6 degree of freedom (DOF) rigid bodies with mass, stiffness and damping matrices according to the relevant hydrodynamic properties. The structural damping in both computer programs is modelled using Rayleigh damping and linear material properties are applied. Rigid body connections are used to model the connections between the tower and the stay-cables, the girder and the stay-cables, the columns and the girder, and the pontoons and the columns. Both models are fixed at the bottom of the tower and at each end of the bridge, as well as in the global y-direction for the girder at AX2. The element length varies according to the location. The length of the elements are roughly 3 m for the tower, 20 m for the stay-cables, 7 to 27 m for the columns, and 10 to 20 m for the girder.

In both computer programs the hybrid frequency- and time domain method is used to solve the equation of motion, resulting in the well-known Cummins Equation (Cummins, 1962).

$$q_j^{exc}(t) = \sum_{k=1}^{6} \left[M_{jk} + A_{jk}^{\infty} \right] \ddot{u}_k(t) + D_{jk}\dot{u}_k(t) + \left[K_{jk} + C_{jk} \right] u_k(t) + \int_0^{t_{mem}} k_{jk}(t-\tau)\dot{u}_k(\tau)d\tau \tag{1}$$

Here, $q_j^{exc}(t)$ represents the wave excitation load, which includes the first order wave load $q_j^{(1)}(t)$, the second order wave loads $q_j^{(2)}(t)$ and the drag load $q_j^{(d)}(t)$. The notations M_{jk}, K_{jk}, D_{jk} represent the structural mass, stiffness and

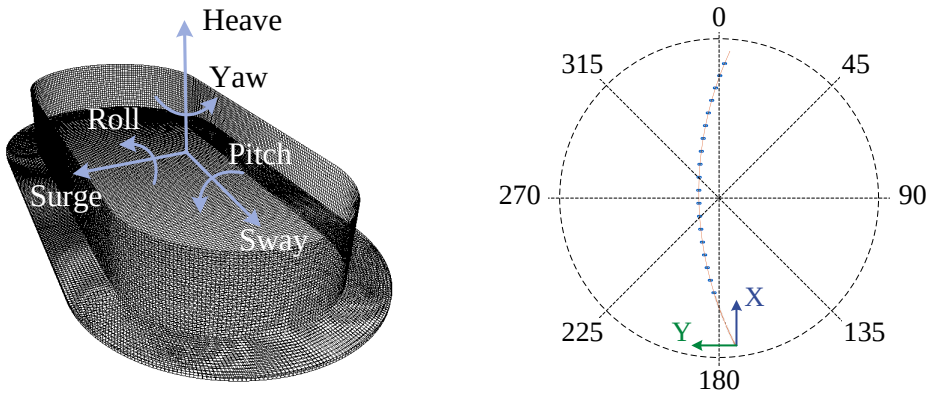

(a) Panel model. **(b)** Wave directions.

Fig. 2. Pontoon panel model with heave plate extruding from the bottom and compass notation of wave directions at the Bjørnafjord site. (a) Panel model. (b) Wave directions.

TABLE 2. Pontoon properties without ballast

Property	Unit	Value
Mass	[ton]	1.13E+04
Roll inertia	[ton·m^2]	4.90E+06
Pitch inertia	[ton·m^2]	1.36E+06
Yaw inertia	[ton·m^2]	5.70E+06
COG from waterline	[m]	-4.20E+00
Displacement	[ton]	1.88E+04
Roll water plane stiffness	[kNm/rad]	3.98E+06
Pitch water plane stiffness	[kNm/rad]	7.38E+05
Heave stiffness	[kN/m]	1.74E+04

Source: Data from Statens Vegvesen (2017).

damping in the system. The frequency-dependent added mass $A_{jk}(\omega)$ and damping $B_{jk}(\omega)$ are included by the added mass at infinite frequency A^{∞}_{jk} and the retardation function $k_{jk}(t)$. The time dependent displacement response and its time derivatives are symbolized by $u_k(t)$, $\dot{u}_k(t)$ and $\ddot{u}_k(t)$. Finally the time shift is denoted by τ and the time "memory" by t_{mem}.

Modelling Hydrodynamic Loads

Generating Wave Elevation

The wave elevation in the floating bridge models is based on a 3-parameter JONSWAP (Hasselmann et al., 1973) wave spectrum, see Eqn. (2), with parameters according to the 100-year wave environment at the Bjørnafjorden site (Statens Vegvesen, 2017):

$$S_{\zeta}(\omega) = \frac{\alpha g^2}{\omega^5} \exp\left[-\frac{5}{4}\left(\frac{\omega_p}{\omega}\right)^4\right] \gamma^{\,b} \tag{2}$$

where,

$$\alpha = \left(\frac{H_s \omega_p^2}{4g}\right)^2 \frac{1}{0.065\gamma^{0.803} + 0.135}$$

$$b = \exp\left[-\frac{1}{2\sigma^2}\left(\frac{\omega}{\omega_p} - 1\right)^2\right]$$

$$\sigma = \begin{cases} 0.07 & \text{for} \quad \omega < \omega_p \\ 0.09 & \text{for} \quad \omega > \omega_p \end{cases}$$

and g is the gravitational constant. The directional spreading is governed by the spreading function $D(\theta)$ where θ_0 is the main wave direction, $\Gamma(\cdot)$ is the Gamma function and s is the spreading exponent. The spreading exponent value used in the comparison is set to 4, within naturally occurring short-crested wave environments.

$$D(\theta) = \frac{1}{\sqrt{\pi}} \frac{\Gamma(\frac{s}{2} + 1)}{\Gamma(\frac{s}{2} + \frac{1}{2})} \cos^s(\theta - \theta_0), \quad |\theta - \theta_0| \leq \frac{\pi}{2} \tag{3}$$

An important note should be made about the implementation of the directional spreading function in the two computer programs, which has a significant influence on the response characteristics in short-crested seas. The numerical implementation is based on a chosen number of wave directions, which in this study is set to 11. Based on the number of wave directions the exact wave directions are calculated automatically in both computer programs. In SIMO-RIFLEX the wave directions are chosen based on a linear distribution from $-\frac{\pi}{2}$ to $\frac{\pi}{2}$, whereas OrcaFlex distributes the wave directions according to the equal energy strategy (Orcina, 2019) giving a more narrow spreading around the main wave direction. Due to the orientation and geometry of the floating pontoons even small waves in surge are expected to have a significant effect on the bridge response. In order to compensate for this difference in the two computer programs, a user specified directional wave spectrum is used in SIMO-RIFLEX based on the spectrum values and directional spreading values used in OrcaFlex.

Modelling the Pontoon-Wave Interaction

The interaction between the pontoons and the water is based on linear potential theory using Wadam (DNV, 2014) for a single pontoon with the dimensions previously described. The draft is set to 10.5 meter and a double-symmetric panel model is used in the analysis. The wave directions applied goes from 0° to 90° with a resolution of 5° and the 60 wave frequencies are within 0.033 to 1 Hz with varying step length in order to give a smooth description of the first order wave load transfer function and the mean drift load. An element mesh density of 0.4 meter is applied to the panel model resulting in roughly 9,200 elements. The high resolution of the panel model is used in order to minimize the sensitivity to the mesh. Figure 3 shows the convergence of the frequency-dependent added mass in roll with respect to the panel element size as well as the convergence of the mean wave load with respect to the panel element size using both direct pressure integration (near-field method) and conservation of momentum (far-field method). The far-field method converges very fast and for the chosen mesh resolutions the result is the same. Instead the near field method shows slow or non-existing convergence for the horizontal mean drift loads. Pan et al. (2013) investigated the convergence of a panel model in Wadam with regard to the far-field and near-field solutions of mean drift loads. They tested different panel mesh quality of an LNG model, showing that for horizontal mean drift loads (surge, sway and yaw) the near-field method exhibits great difficulty to converge even for a very fine panel model, while vertical mean drift loads (heave, roll and pitch) tends to converge faster for the near-field method. Their recommendation for a common calculation is to apply the far-field method for the horizontal loads, and near-field method for the vertical loads if necessary. For the current study only horizontal mean drift loads estimated using the far-field method is considered since the focus is on comparison of the structural response and less on modelling details. The hydrodynamic coefficients calculated in Wadam are used as input for the numerical model in both computer programs.

Ballast is included in OrcaFlex by using 6 DOF buoys with the relevant inertia properties, whereas in SIMO-RIFLEX the relevant elements in the pontoon mass matrices are updated accordingly.

Buoyancy is implemented in SIMO-RIFLEX using a constant vertical force at the center of buoyancy on each pontoon and by removing the buoyancy terms for roll and pitch in the hydrostatic stiffness matrix. In OrcaFlex the buoyancy is defined by the displaced volume and the location of the center of buoyancy.

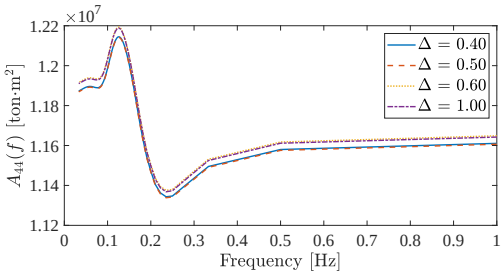

(a) Convergence of total hydrodynamic added mass in roll

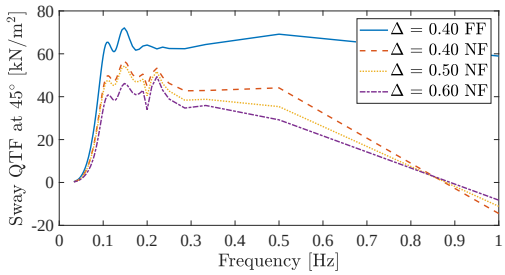

(b) Convergence of the mean drift load

Fig. 3. Convergence with respect to element length Δ in the pontoon panel model. (a) Convergence of total hydrodynamic added mass in roll. (b) Convergence of the mean drift load using near-field (NF) and far-field (FF) methods. For convenience, only a single line is shown for the FF method since the remaining lines, representing the other mesh sizes when using the FF method, are almost identical.

Generating First Order Wave Loads

The first order wave loads are generated by Monte Carlo simulation using fast Fourier transformation (FFT) of the real part of the product of the first order wave transfer function and the wave elevation:

$$q_j^{(1)}(x,y,t) = \Re \sum_{m=1}^{N_\omega} \sum_{n=1}^{N_\theta} \sqrt{2S_\zeta(\omega_m)D(\theta_n)\Delta\omega_m\Delta\theta_n} \tag{4}$$
$$\left|H_j^{(1)}(\omega_m,\theta_n)\right| \exp\left[i\left(\varepsilon_{nm} + \varphi_{H_{jnm}^{(1)}}\right)\right] \exp\left[i\left(\omega_m t - k_m x\cos(\theta_n) - k_m y\sin(\theta_n)\right)\right]$$

where $S_\zeta(\omega_m)$ is the unidirectional wave spectrum, $D(\theta_n)$ is the directional spreading function, k_m is the wave number, ε_{nm} is the random phase angle, $H_j^{(1)}(\omega_m,\theta_n)$ is the first order wave load transfer function and $\varphi_{H_{jnm}^{(1)}}$ the phase angle.

Generating Second Order Wave Loads

In both computer programs the second order wave loads in the horizontal plane are generated by Monte Carlo simulation using second order FFT:

$$q_j^{(2)}(x,y,t) = \Re \sum_{l=1}^{N_\omega} \sum_{m=1}^{N_\omega} \sum_{n=1}^{N_\theta} \sqrt{2S_\zeta(\omega_l)D(\theta_n)\Delta\omega_l\Delta\theta_n} \tag{5}$$
$$\left|H_j^{(2-)}(\omega_l,\omega_m,\theta_n)\right| \sqrt{2S_\zeta(\omega_m)D(\theta_n)\Delta\omega_m\Delta\theta_n} \exp\left[i\left((\omega_l-\omega_m)t + \varepsilon_{nl} + \varepsilon_{nm} + \varphi_{H_{jnlm}^{(2-)}}\right)\right]$$

where $H_j^{(2-)}(\omega_l,\omega_m,\theta_n)$ denotes the quadratic transfer function (QTF) of the difference-frequency wave load, and $\varphi_{H_{jnlm}^{(2-)}}$ is the phase angle. The Newman's approximation (Faltinsen, 1993) is applied to simplify the above equation by reducing the full QTF data to only diagonal terms representing component pairs with identical wave direction and wave period. The consequence of the Newman approximation is that the phase angle $\varphi_{H_{jnlm}^{(2-)}} = 0$ and

$$H_j^{(2-)}(\omega_l,\omega_m,\theta_n) = \sqrt{|H_j^{(2-)}(\omega_l,\omega_l,\theta_n)H_j^{(2-)}(\omega_m,\omega_m,\theta_n)|} \tag{6}$$

taken as the geometric mean. The Newman's approximation is most likely not valid for the short-crested sea used in the present study. However, since the focus of the paper is more on how well the two computer programs compare than

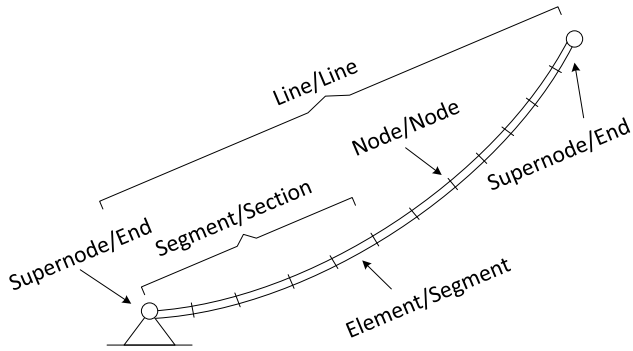

Fig. 4. Sketch of Finite Element model for a line with specified SIMO-RIFLEX/OrcaFlex nomenclature. (Adapted from SINTEF Ocean 2017a.)

on making the analysis completely physically correct, the authors find that the results obtained from the comparison would still be of interest to the reader.

The mean drift load coefficients are in principle influenced by the first order motion, which is unknown before the final hydro-elastic time-domain simulation is made. As a consequence the coefficients should be obtained based on an iterative loop between the radiation and diffraction analysis and the following time-domain simulations. As a first approximation of the mean wave load in the present study, however, the pontoon is fixed in its mean position in all six DOFs in the Wadam analysis. With a focus on comparing the two computer programs, this approximation is acceptable for the present study.

Modelling Viscous Effects

The viscous effects on the pontoons are modelled as drag loads using Morison elements. Equation (7) describes the viscous drag load for a single element in the local element coordinate system.

$$q_j^{(d)}(t) = \frac{1}{2}\rho C_j^d A_j u_r(t)\,|u_r(t)| \tag{7}$$

Where C_j^d is the quadratic drag coefficient, ρ is the density of the water, A_j is the cross-sectional area in direction j and $u_r(t)$ is the relative velocity of the water at the Morison element.

Different values have been suggested for the quadratic drag coefficients. Xiang et al. (2017) suggested a vertical drag coefficient of 4.2 according to model tests and supporting literature, whereas Cheng et al. (2018a) used a more conservative estimation of $C_x^d = 1.0$, $C_y^d = 0.6$ and $C_z^d = 2.0$ following the global coordinate system notation. The latter option is applied in the present study.

For each pontoon two Morison elements are used, and these are oriented with the axial direction pointing along the positive global z-axis The first element starts at the bottom of the pontoon and continues up to the top of the heave plate. The second element starts at the top of the heave plate and continues up to the mean water line. The cross-sectional areas in the three directions for the first element are $A_x^{(1)} = 47$ m^2, $A_y^{(1)} = 23$ m^2 and $A_z^{(1)} = 2654$ m^2. Similarly for the second element the values are $A_x^{(2)} = 673$ m^2, $A_y^{(2)} = 277$ m^2 and $A_z^{(2)} = 0$ m^2.

Modelling Structural Properties

The presented computer programs make use of the Finite Element Method (FEM) formulation to combine the structural and hydrodynamic parts into a complete Finite Element (FE) model. The theory of FEM is well-known and will not be covered here. For more detailed information the reader is referred to the respective theory manuals for the two computer programs (SINTEF Ocean, 2017a; Orcina, 2019). Instead a short description of the relevant assumptions is given in this section following the nomenclature within each of the two theory manuals, see Fig. 4 for a clarification of the nomenclature.

Line Theory

The lines in both computer programs are comprised of the same FE structure as illustrated in Fig. 4 and the smallest FE unit is the element/segment between each node, which model the axial and torsional properties using sets of springs and dampers. The bending properties are represented by springs and dampers at each node and mass properties are lumped to the nodes. Both computer programs are capable of including non-isotropic bending stiffness and non-linear geometric stiffness used in the comparison. Large rotations of the elements/segments are made possible by implementing Green strain theory to account for geometric stiffness. Linear material properties are defined for each element/segment cross-section and no torsion-bending coupling or torsion-tension coupling is included. Bending stiffness properties are modelled using Bernoulli-Euler beam theory.

Note on Modelling the Twin-Box Bridge Girder

The bridge girder is modelled as a single equivalent beam in both computer programs based on the properties listed in Tab. 1. In SIMO-RIFLEX the radius of gyration is given as a single value for the cross-section, whereas in OrcaFlex the radius of gyration is estimated based on user specified inertial values for each box in the twin-box cross-section. The effect of this difference is unknown but thought to be insignificant for the analysis.

Structural Damping

The structural damping is modelled as Rayleigh damping, see Eqn. (8), in both computer programs and the mass proportional damping coefficient μ and the stiffness proportional damping coefficient λ are based on a target damping ratio ξ of less than 2 % in the frequency range of the natural periods and the wave spectrum.

$$\xi = \frac{1}{2}\left(\frac{\mu}{\omega} + \lambda\omega\right) \tag{8}$$

For the target value of the damping ratio the corresponding damping coefficients used are $\mu = 0.0025$ and $\lambda = 0.02$. The damping ratio for the first two natural frequencies are thereby given as 1.22 % and 0.83 %, respectively.

Solution Procedures

Finding Static Equilibrium

The static equilibrium is found through incremental loading of the external forces and using an iterative procedure (SINTEF Ocean, 2017a; Orcina, 2019). In SIMO-RIFLEX this iterative procedure is the Newton-Raphson iteration procedure.

Solving the Standard Eigenvalue Problem

In both computer programs the iterative Lanczos Method is applied when solving the standard eigenvalue problem of the system. In this method the hydrodynamic added mass of the pontoons is taken into account by summing the added mass at infinite frequency and the structural mass of the pontoons before solving the equations. The main drawback of this method is that the frequency-dependent added mass is simplified into a constant value. The natural periods found based on this method are denoted by T_n, where n is the number of the mode. In order to account for the exact added mass a method based on the pseudo procedure illustrated in Fig. 5 is performed manually for SIMO-RIFLEX. The method is based on the initial set of frequencies ω_n and implies an iteration at each frequency by assuming that the corresponding modeshape remains the same. By manually defining the added mass as the exact added mass at the corresponding frequency, i.e. $A_{jk}(\omega_n)$, the final solution is obtained when the difference between two consecutive frequencies is below a user specified tolerance. The natural periods found based on this method are denoted by T_n^a. In OrcaFlex the exact added mass is accounted for in the T_n^b values which are found manually using a graphical method. In the graphical method the modeshapes are again assumed to remain in the original order and shape. By first solving the standard eigenvalue problem 60 times for each of the 60 hydrodynamic added mass values a line can be drawn for each mode in a coordinate system with two axes representing periods. This line contains the horizontal coordinate values equal to the 60 periods related to the hydrodynamic added mass values inserted in the standard eiganvalue problem. The vertical coordinate values represent natural periods of the relevant mode for each solution to the standard eigenvalue problem. By drawing a second line with the same horizontal and vertical period values representing the equation $T_j = T_j$ the solution is found as the intersection between these two lines.

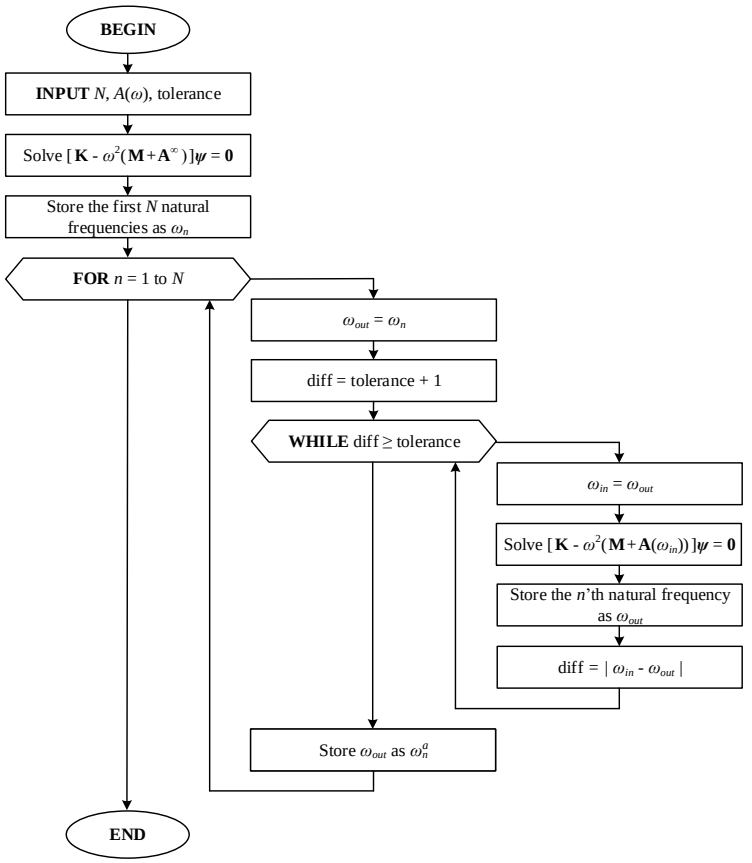

Fig. 5. Pseudo procedure to solve the standard eigenvalue problem when manually including frequency-dependent added mass

Solving the Time-Domain Equations

Equation (1) is a non-linear time domain equation which includes geometric stiffness and hydrodynamic loading. The solution is found in SIMO-RIFLEX using a step-by-step numerical integration based on the Newmark β-family integration method (SINTEF Ocean, 2017a). Here the integration parameters are $\beta_{int} = 0.256$ and $\gamma_{int} = 0.505$ which adds small amounts of artificial damping to the system in order to reach convergence earlier. This artificial damping has negligible effect on the final results.

In OrcaFlex the implicit Generalized-α integration scheme is used. This method also adds small amounts of numerical damping to the system in order to damp out the non-physical high-frequency part of the response inherent in the FEM solution procedure (Orcina, 2019). Again, this added damping has close to no effect on the final solution.

Several steps have been taken to stabilize the time-domain solution in both computer programs. To reduce the effect of transients in the results a ramping time of 100 seconds is used and the initial 1,000 seconds are removed from the response time series in the post-analysis. The time steps used in the two computer programs are based on individual time step convergence studies. SIMO-RIFLEX uses a time step of 0.01 seconds, whereas OrcaFlex uses 0.2. To compensate for this difference the SIMO-RIFLEX time series are down sampled to a time step of 0.2 before comparing standard deviations, response spectra and so forth.

TABLE 3. Load cases with irregular waves used in the present study with a main wave direction of 270° and JONSWAP parameters $H_s = 2.4$ m, $T_p = 5.9$ s and $\gamma = 2.0$. Load case LC2a and LC2b include 11 wave directions in the directional spreading function distributed according to the default of each program (LC2a) and by manually specifying the exact same directions in SIMO-RIFLEX as in OrcaFlex (LC2b).

Load Case	Waves Loads	Viscous Effects	Spreading
LC1	1st order	No	-
LC2a	1st order	No	4
LC2b	1st order	No	4
LC3	1st order	Yes	4
LC4	1st + 2nd order	No	-
LC5	1st + 2nd order	Yes	-

Program Comparison Method

The static response and the modal properties given by the two computer programs are compared, and subsequently several comparisons are made between time domain results. The comparison in the time domain includes deterministic response from regular long-crested waves, followed by six stochastic load cases listed in Table 3. The load cases are chosen in order to identify the differences in the response for each step of complexity added in the models. Starting with first order long-crested irregular wave loads and no viscous effects from the heave plate (LC1), the comparison follows two paths; A) Directional spreading is included in two different ways (LC2a and LC2b) and later viscous effects from the heave plate are added (LC3). B) Second order long-crested irregular wave loads are added (LC4) and finally viscous effects from the heave plate is added (LC5). The JONSWAP wave parameters specified for each load case are chosen according to the 100-year wave environment at the Bjørnafjorden site for a wave direction of 270° (Statens Vegvesen, 2017). For each load case six 1-hour simulations with unique sets of wave seeds are used in the analysis in order to have a stable standard deviation of the response. The comparison focuses on the vertical displacement and the bending moments along the bridge

RESULTS AND DISCUSSION

Static Response of Floating Bridge

Table 4 shows a selection of the static response along the bridge girder in calm water based on the same stiffness and mass input for the bridge superstructure and the pontoons. The two computer programs generally show the same results but small differences are present. An increasing difference in the vertical displacement z from AX3 to AX8 is noted between the two computer programs, with differences starting at 0.03 % (1.5 cm) and steadily increasing to 0.87 % (13.0 cm). The increasing difference is a result of SIMO-RIFLEX exhibiting increasingly smaller values along the high bridge section. At the low bridge section from AX8 to AX21 the difference is constant at roughly 0.87 % (13.0 cm). The weak axis bending moment shows a slight difference of up to 7 % (60 MNm) between the two computer programs noting that SIMO-RIFLEX consistently gives larger negative values along the bridge. The effective tension T_e varies along the bridge with positive values between 300 and 800 kN at AX3 to AX7 in OrcaFlex. At the same locations SIMO-RIFLEX show roughly 35 % larger positive (tension) values. At the low bridge section from AX8 to AX21 OrcaFlex show negative tension of roughly -250 kN whereas SIMO-RIFLEX show slightly positive tension around 40 kN. Although these differences are small they are thought to have an effect on the natural frequencies and modeshapes in the two computer programs.

Natural Frequencies and Modeshapes

Table 5 lists the natural periods found using the two computer programs and an indication of the dominating motions for the corresponding modeshapes. The natural periods T_n are found using the added mass at infinite frequency when solving the standard eigenvalue problem, whereas T_n^a values are found by using the pseudo procedure listed in Fig. 5 for SIMO-RIFLEX. Natural periods denoted by T_n^b are found manually using OrcaFlex and the graphical method described above.

An initial observation is the significance influence of the frequency-dependent added mass on the estimated natural periods. Due to the heave plate the frequency-dependent part of the added mass has a significant influence and should

TABLE 4. Static response at selected locations along the floating bridge

Axis	SIMO-RIFLEX			OrcaFlex		
	z [m]	M_y [MNm]	T_e [kN]	z [m]	M_y [MNm]	T_e [kN]
AX3	47.5	-532	798	47.4	-521	539
AX4	42.3	-1,000	1,011	42.4	-939	743
AX5	34.7	-856	1,074	34.8	-799	818
AX6	26.8	-898	1,064	27.0	-839	802
AX7	19.0	-889	567	19.1	-830	290
AX8	15.0	-893	57	15.1	-834	-236
AX10	15.0	-895	51	15.1	-835	-244
AX15	15.0	-899	37	15.1	-838	-257
AX20	15.0	-901	21	15.1	-839	-262

not be neglected.

In general the first eight natural periods T_n have distinct values separated with a large margin and their corresponding modeshapes are primarily in the horizontal plane and has secondary torsional motions. From mode eight and upwards the difference in the values are less than a second and for the most part less than roughly 0.3 seconds. The lower natural periods will be excited by both first and second order wave loads, while the higher natural periods coincide with the wave spectrum at the Bjørnafjorden site resulting in roughly 35 active modeshapes to be accounted for in the design. The higher modes are important since the dominating motions are in the vertical plane and include pendulum motion of the pontoons. Both of these increase the weak axis bending moment in the bridge girder significantly.

A reasonable match within 2% is noted between most of the natural periods in the two computer programs, with only mode 3, 6 and 7 having differences of 3.8, 4.9 and 4.1%, respectively. Although natural periods T_n^a are given for the pseudo procedure shown in Fig. 5 they will not be compared to the natural periods T_n^b using the graphical method due to fundamental differences in the two methods. Instead the T_n^a values will later be used to link the natural periods to the response spectra.

As the natural periods differ slightly so do the corresponding modeshapes shown in Fig. 6. The first six modes show the same form but as the modes increase so do the differences between the two computer programs. Mode 10 to 28 all show the same general shapes with increasing dominance of the vertical and pendulum motion. OrcaFlex seems to emphasise the horizontal and torsional motion more than SIMO-RIFLEX. This can have important effects on the dynamic response of the bridge in general. The differences observed in the natural periods are thought to be related to the small deviations in the static response, possible rounding errors and more generally a difference in the implementation of the theory in the two computer programs. With mass and stiffness being the only governing parameters for the value of the natural periods of the structure, the difference is to be found in either erroneous mass and stiffness input by the users of the two computer programs, or the implemented methods governing the calculation of the natural periods inside the two computer programs. We have made our best effort to compensate for the differences in the implementation of the theory in the two computer programs and checked the input on several different occasions to eliminate any possible user mistakes. A potential user mistake is how the rotational mass is included in the two computer programs. In OrcaFlex the rotational mass is included using 6 DOF Buoys at each element node along the bridge elements. These 6 DOF Buoys are only given rotational mass properties and have no other effect on the model. In SIMO-RIFLEX it is included as a constant radius of gyration value r_x for each cross-section. The values are linked through Eqn. 9.

$$r_x = \sqrt{\frac{R_x}{m \cdot L_e}} \tag{9}$$

Where r_x is the radius of gyration used in SIMO-RIFLEX, R_x is the total moment of inertia of the 6 DOF Buoy, m is the average mass per meter of the adjacent elements and L_e is the average element length. As the 6 DOF Buoys are attached to the element nodes a sensitivity study has been carried out internally regarding the needed distance

TABLE 5. Natural periods of the floating bridge models. The notation T_n indicates the use of added mass at infinite frequency when solving the standard eigenvalue problem. The notations T_n^a and T_n^b indicate the use of the iterative and graphical procedure to include the exact added mass, respectively. The symbols for primary and secondary motions refer to horizontal (H), vertical (V), torsional (T) and pendulum (P) motions. Pendulum motion is the motion of the pontoons going from side to side like a pendulum.

Mode	SIMO-RIFLEX				OrcaFlex				Diff.
n	T_n	T_n^a	Dominating motion		T_n	T_n^b	Dominating motion		T_n
[-]	[s]	[s]	Primary	Secondary	[s]	[s]	Primary	Secondary	[%]
1	50.79	55.63	H	-	51.81	54.15	H	-	2.0
2	29.28	31.63	H	-	29.79	30.64	H	-	1.7
3	22.55	24.41	H	T	21.76	22.79	H	T	3.8
4	17.56	19.28	H	T	17.52	18.53	H	T	0.2
5	13.56	14.91	H	T, V	13.59	14.66	H	T	0.1
6	12.67	13.06	T	H, V	12.08	12.26	H	T	4.9
7	12.15	12.31	V	T	11.67	11.71	H	V	4.1
8	11.44	11.29	T	V	11.39	11.53	V	H	0.5
9	11.39	11.27	V	-	11.37	11.34	V	H, T	0.2
10	11.39	11.09	V	-	11.36	11.16	V	H, T	0.2
17	10.69	9.96	V	P	10.61	-	V	P, H	0.8
24	8.91	9.24	V	P	8.81	-	V	T, P	1.1
28	8.13	8.02	T	H	7.97	-	V	H, V, P	2.0

between the Buoys. The findings suggest that the 10 m used in the present paper is a sufficient length. Based on this procedure, the differences observed in the natural periods are thought to be related to how the two computer programs implement the theory governing the calculation of the natural periods, including the used of the final static position in the Generalized Lanczos Method when calculating the natural periods. It is particularly the rotational modes that are shown to be the most uncertain and further experimental verification is needed before any concluding remarks can be made regarding this issue. A validation towards old experiments for a short floating bridge structure has been carried out in Xiang and Løken (2019) for OrcaFlex and a similar verification is currently under way for SIMO-RIFLEX. However, the shorter bridge has very different dynamic properties with the lowest natural period of approximately 10 s. Furthermore, in order to verify the numerical models of the presented long floating bridge structure, only a part of the bridge can be compared due to size limitations of existing ocean basins and hybrid tests are the only option. This forces the experimental results to rely heavily on the computer program used. The issue with the rotational modes highlighted here is hence an important contribution and sheds light on the need for including model tests aimed at the issue with rotation.

Dynamic Response in Regular Waves

This section describes the deterministic response from regular long-crested waves. Figure 7 illustrates the dynamic vertical motion of the bridge girder at AX11 calculated using the two computer programs showing an insignificant variation in the amplitude and period. Initial transients are observed in both computer programs up to roughly 1,000 seconds depending on the wave period but eventually a stable steady state response is found.

The response amplitude operator (RAO) of the vertical displacement z, the weak axis bending moment M_y and the strong axis bending moment M_z are illustrated in Fig. 8 with the chosen locations representing the general behaviour along the bridge. The natural periods T_n^a from SIMO-RIFLEX using the iterative method are also shown in the figure for mode 4, 5, 6, 10 and 28 in order to illustrate the connection to the relevant modeshapes.

The two computer programs show a satisfactory agreement with some differences at AX10 for the weak axis bending moment. Generally the RAOs for the vertical displacement in the two computer programs follow the same behaviour. The most dominating peak in the vertical displacement RAO located at 11 s is recurring at almost every pontoon and is explained by roughly six vertical modeshapes being active at natural periods within 1 s away from this peak. For OrcaFlex two additional peaks are shown at roughly 15 s (mode 5) and 19 s (mode 4) for AX10, AX15 and

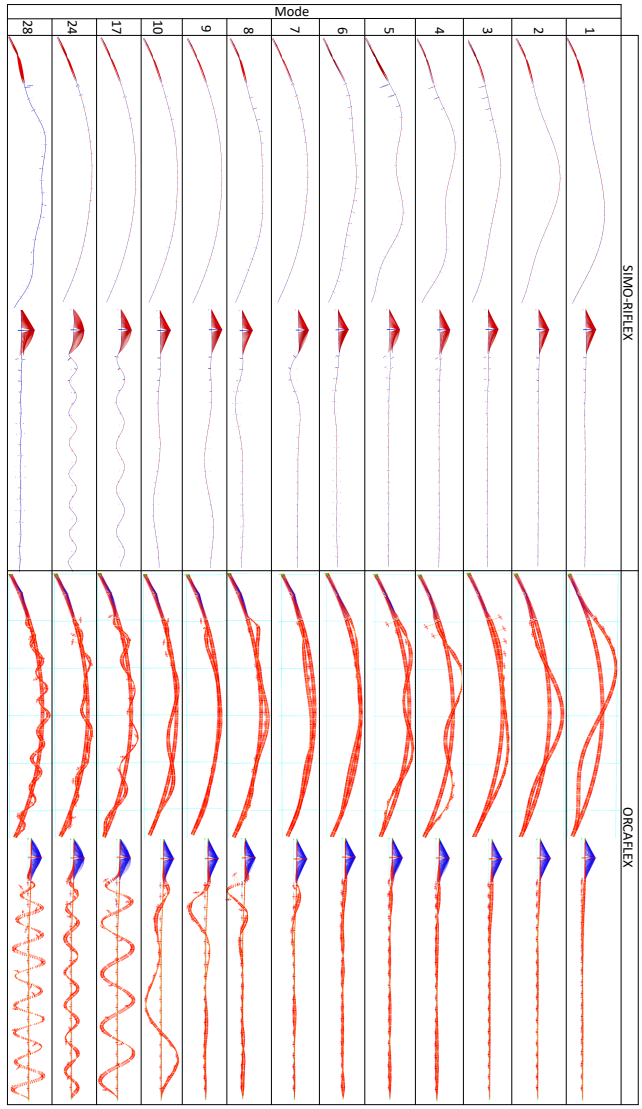

Fig. 6. Modeshapes of floating pontoon bridge using added mass at infinite frequency

AX20. This peak is not represented in SIMO-RIFLEX which seems to be related to the different shape of mode 4 and 5 in the two computer programs.

The strong axis bending moment in the bridge girder exhibits similar trends in the RAOs with some notable shifts in the peak periods, corresponding to the slight differences in the periods of mode 4 and 5 representing horizontal modes. The amplitudes at the corresponding peaks show a satisfactory agreement.

The RAOs for the weak axis bending moment are less similar in shape but are within the same order of magnitude. The complexity of the system makes it difficult to explain the exact reasons but some general comments can be given about the behaviour. In both computer programs the weak axis bending moment RAOs seem to be governed primarily by high frequency modes around mode 28, except for the bridge ends (here illustrated with the RAOs at AX5 and

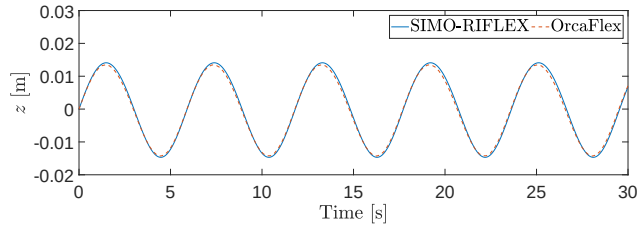

Fig. 7. Dynamic vertical motion of bridge girder at AX11 when subjected to regular long-crested waves from 27° with $T = 5.9$ s and $H = 2.4$ m

AX20), where the energy at low frequency modeshapes is significantly larger. In OrcaFlex the three dominating peaks at AX5 are strongly correlated to mode 4, 5 and 7. The same peaks are also present at the low bridge section, although with significantly smaller amplitudes. Instead the frequencies around mode 10 and 28 are relatively more important. Using the same analogy for SIMO-RIFLEX, the dominating frequencies are close to mode 4, 5, 6, 10 and 28, albeit the correlation is not as strong as in OrcaFlex.

The structural system is not only complex due to the close modeshapes but also directionality sensitivity is a large contributor. Figure 9 shows the RAOs at AX5 with a resolution of 1 second in OrcaFlex for three different wave directions. Waves travelling in directions larger than 270° are more aligned with the longitudinal direction of the bridge girder at AX5 and will generate larger wave forces in surge on the pontoons resulting in higher excitation of the pendulum motion in the bridge girder. This increases the weak axis bending moment as seen in the figure. Similarly the changing wave direction affects the vertical displacement and the strong axis bending moment along the bridge. This effect is captured by both computer programs with only small differences that can be explained by the same source of errors as mentioned above. The directional sensitivity has been reported for similar floating bridges with varying lengths, see e.g. Leira and Remseth (1990), Kvåle et al. (2016), Villoria (2016) and Viuff et al. (2019), and is in part a consequence of the many different modeshapes of the structure.

It should be noted that the mentioned RAOs are found using the time domain method and will not show the same behaviour as results found using the frequency domain method. However, no frequency domain method is available in SIMO-RIFLEX and instead the RAOs include effects apparent in the non-linear time domain solution procedure and imperfect wave loads from the FFT method.

Dynamic Response in Long-crested Irregular Waves

The wind driven waves are governed by the JONSWAP wave spectrum with a peak period of 5.9 s and with the most significant part of the wave energy between 2 and 12 s. The response is therefore governed mostly by the higher modes from 7 and upwards where generally speaking the differences in the RAOs are smaller. However, these higher modes are also the ones showing the largest differences in their corresponding modeshapes.

Figure 10 illustrates variation of the average absolute differences in the standard deviation of the vertical displacement, the effective tension and the weak axis bending moment at the specific axis locations along the bridge based on the six stochastic time domain simulations for load case LC1. The difference in each response change along the entire bridge with each response having minimum and maximum differences at different axes. The average absolute differences along the bridge of the vertical displacement, the effective tension and the weak axis bending moment are roughly 7, 13 and 9%, respectively.

Effect of Directional Spreading

Including directional spreading is a better representation of the wave environment at the Bjørnafjord site and the response spectra of the weak axis bending moment at AX4 and AX11 for load case LC1 and LC2b for both computer programs are shown in Fig. 11. The weak axis bending moment response spectra at the axes generally become more narrow-banded when going from the bridge ends towards the middle of the bridge but the same differences between the two computer programs are present at all locations. The two computer programs capture roughly the same total energy in the weak axis bending moment response spectra but the amplitudes at the different frequencies are not the same, which is again thought to be a consequence of the slight differences in the modal properties for the two computer programs. The directional spreading of the waves increases the number of active modeshapes and in this case for AX4 and AX11 the response spectra for the weak axis bending moment show an increased energy which is also supported

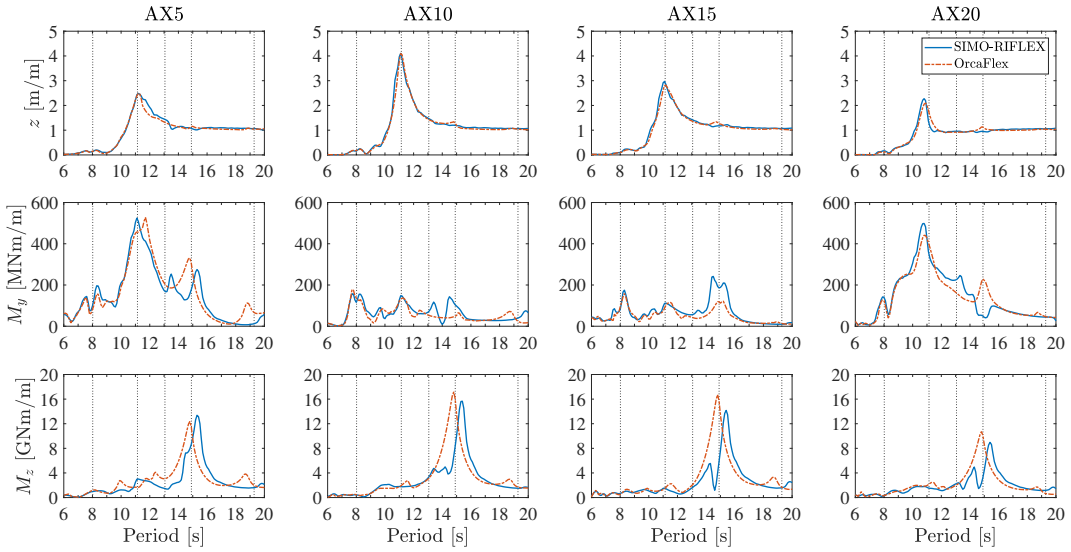

Fig. 8. RAOs at 270° waves for vertical displacement, weak axis bending moment and strong axis bending moment at axis AX5, AX10, AX15 and AX20 along the bridge. The natural periods T_n^a based on the iterative method in SIMO-RIFLEX are shown as the vertical dotted lines for mode 4, 5, 6, 10 and 28 from right to left.

by the study by Langen and Sigbjörnsson (1980). Interestingly enough, the two computer programs do not have the same distribution of the energy over the wave frequencies.

Effect of Second Order Wave Loads

For the investigated wave direction, the effect from the second order wave load on the vertical displacement and the weak axis bending moment is negligible. This is expected since the vertical mean drift loads have been omitted in the present study. Instead the transverse displacement along the bridge is increased significantly. Figure 12 shows the response spectrum of the transverse displacement in the global y-direction at AX19, and shows four clear peaks for both software, indicating the natural period of the first four modes of the bridge. The modes shown in the response spectra are close to the predicted values (within 10%).

Another effect seen in Fig. 12 is the increased standard deviation of the transverse displacement along the bridge. The transverse displacement in OrcaFlex is slightly larger, especially close to the high bridge, but with statistical uncertainties they compare well.

Influence From Viscous Effects

The effect of the heave plate on the pontoon is two-fold; to increase the added mass of the bridge and thereby shifting important modes away from the wave spectrum, and to increase the viscous drag on the pontoon in order to damp out the vertical motion and thereby decrease the weak axis bending moment (Xiang et al., 2017).

In the present study the viscous effect is added in two separate steps, between LC2b and LC3 and between LC4 and LC5, to see its effect on the response from short-crested first order wave loads and unidirectional first and second order wave loads, respectively.

With the vertical drag coefficients and the corresponding cross-sectional area being relatively larger than those for the horizontal directions, the viscous effect seen on the responses from short-crested first order wave loads is mainly present in the the vertical responses as seen in Fig. 13 for the vertical motion with an average reduction of roughly 8%. A similar average reduction is present in the weak axis bending moment and overall the same effects are captured in both software when including viscous drag.

The viscous effect on the response from the unidirectional first and second order wave loads is mainly seen in the horizontal response with a reduction in the horizontal motion and effective tension of roughly 20 and 14%, respectively, at almost all axes for OrcaFlex. On average the corresponding values for SIMO-RIFLEX are roughly 7-10% larger. The

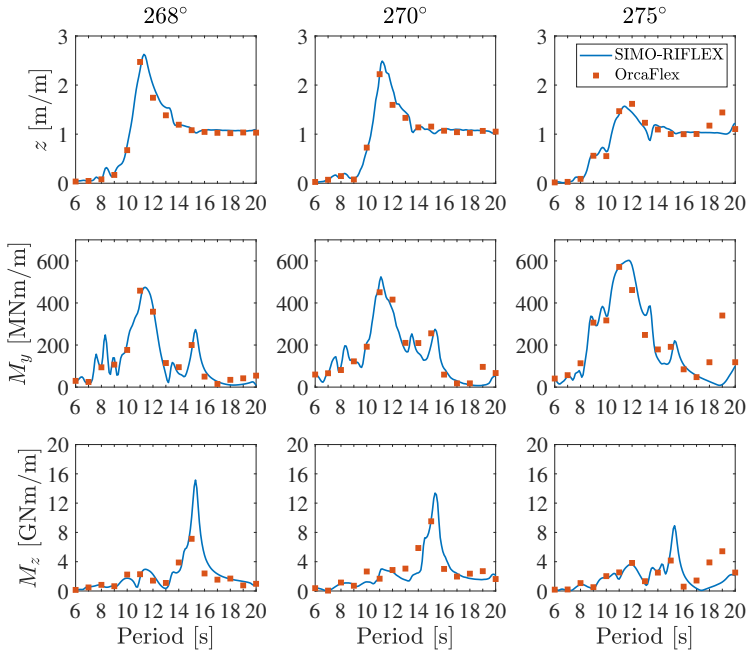

Fig. 9. RAOs at AX5 for different wave directions, showing vertical displacement, weak axis bending moment and strong axis bending moment

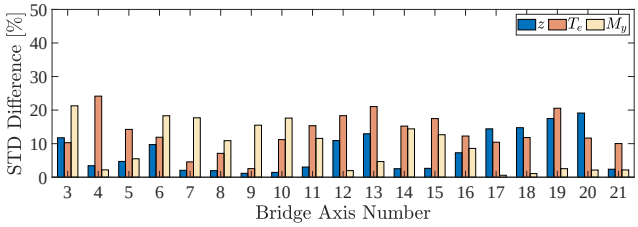

Fig. 10. Average absolute differences in standard deviation of bridge girder response along the bridge for all six simulations of load case LC1.

effect on the strong axis bending moment is shown in Fig. 13 where an average reduction of roughly 7% is present for OrcaFlex, although the actual effect at each axis varies along the bridge. For almost all axes SIMO-RIFLEX shows an increased 5% reduction. The vertical response is also affected, although the effect is much smaller. Negative damping shown as a negative reduction (increase in response) is present at some axes in both software for the vertical motion and the weak axis bending moment, although in OrcaFlex this effect is larger and located at more axes.

Final Notes on Averaged Differences

The standard deviation of the different responses serves to quantify the response along the bridge girder in the two computer programs. As a benchmark of the comparison, averaged absolute differences in the standard deviations of the response along the bridge can be applied. Equation (10) shows how these averaged differences are calculated:

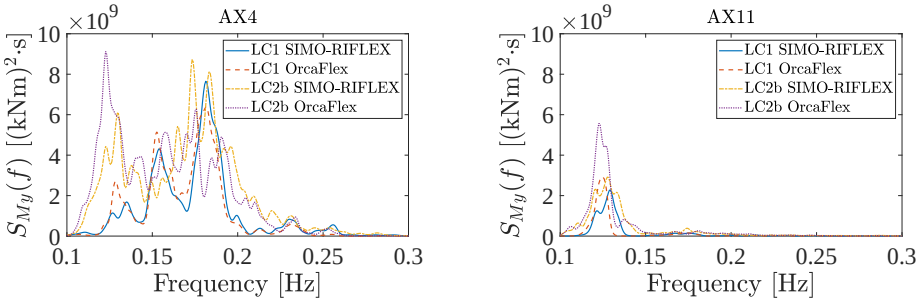

Fig. 11. A comparison of weak axis bending moment response spectra at AX4 and AX11 for load case LC1 and LC2b

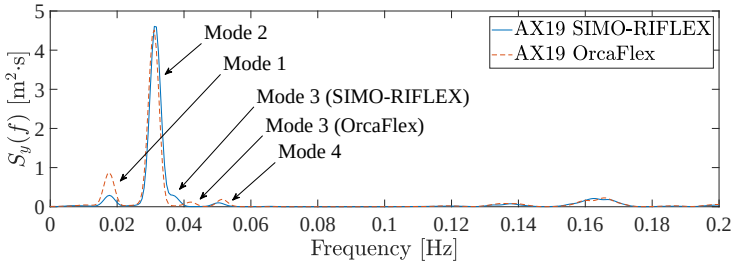

(a) Response spectra of transverse displacement at AX19

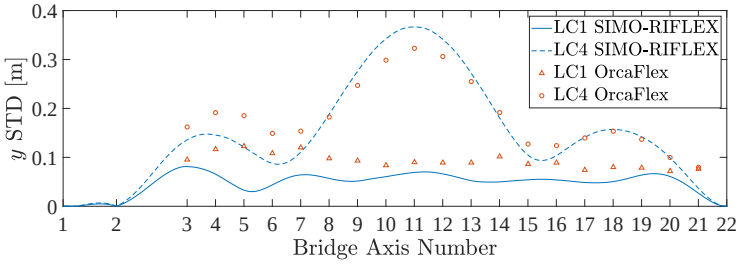

(b) Standard deviation of transverse displacement along the bridge

Fig. 12. Effect of including second order wave loads in the analysis. (a) Response spectra of transverse displacement at AX19. (b) Comparison of standard deviation of transverse displacement along the bridge.

$$\mathrm{STD}_{\mathrm{Diff}} = \frac{1}{N_p}\sum_{p=1}^{N_p}\left(\frac{|\mathrm{STD}_{\text{SIMO-RIFLEX}} - \mathrm{STD}_{\text{OrcaFlex}}|}{\mathrm{STD}_{\text{OrcaFlex}}}\right) \tag{10}$$

where N_p is the number of pontoons. Figure 14 shows box plots of the differences in the internal forces M_y, M_z and T_e in the bridge girder above the 19 pontoon locations along the bridge with the $\times$ representing the averaged difference along all the axes for each response type. Furthermore, the horizontal line indicate the median (located at AX12), the two ends show the minimum and maximum differences and the ends of the box indicate the 50% quantiles. The weak and strong axis bending moments are among the main contributors to the normal stresses in the design of the bridge girder and existing differences will have a significant influence on the final design.

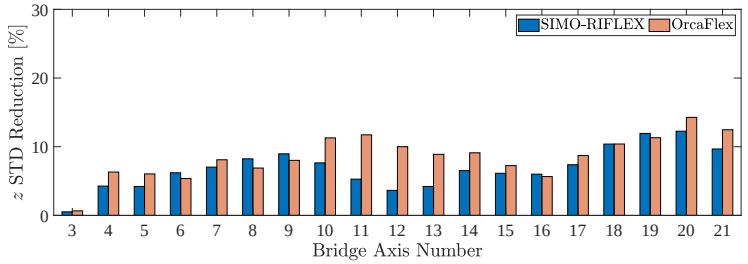

(a) Reduction in vertical displacement going from load case LC2b to LC3

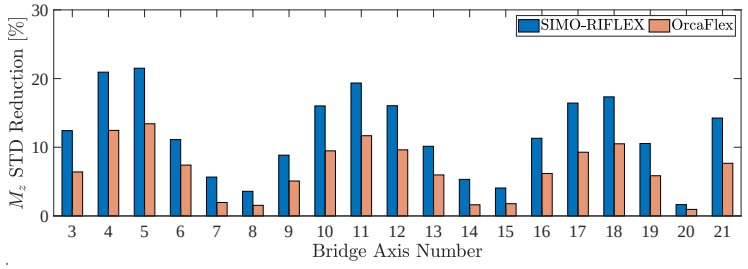

(b) Reduction in strong axis bending moment going from load case LC4 to LC5

Fig. 13. Reduction in standard deviation of responses when including viscous effects. (a) Reduction in vertical displacement going from load case LC2b to LC3. (b) Reduction in strong axis bending moment going from load case LC4 to LC5.

For load case LC1 the average difference in the stochastic response is within 5 and 15%, which is thought to be a realistic benchmark. When comparing the response for short-crested waves however, care must be given to modelling exactly the same directional spreading function $D(\theta)$ in the two computer programs. In SIMO-RIFLEX the spreading angles are by default linearly distributed from $-\frac{\pi}{2}$ to $\frac{\pi}{2}$, whereas in OrcaFlex the spreading angles are weighted according to an equal energy strategy (Orcina, 2019). In Fig. 14 load case LC2a uses the default modelling in both computer programs, whereas in load case LC2b the numerical values for the directional spreading function in OrcaFlex are given as manual input to SIMO-RIFLEX, resulting in significant differences in the average standard deviation for the weak axis bending moment. These larger values for LC2a is due to the larger portion of the waves hitting the pontoons from the side and hence increasing the bridge girder weak axis bending moment. Taking care of modelling exactly the same wave load input in the two computer programs the differences are down to less than 10%. These differences are to some extent directly linked to the general complexity of the system amplifying any small modelling differences when calculating the global response. On top of this, modelling of the boundary conditions, pre-tension forces, methods for implementation of the wave loads and definition of the mass properties of the bridge girder elements are all influencing factors on the final modeshapes and thereby the different stochastic response characteristics. In our experience, if it is not possible to obtain natural periods within less than 5% from each other and having the same modeshapes, it will influence the comparison of any RAOs or stochastic response of the floating bridge structure due to the high complexity. Particularly the uncertainty in the rotational modes is thought to have an effect on the stochastic response. Furthermore different methods for including artificial damping and differences in the solution algorithms also contribute to the variations between the two computer programs.

When comparing the differences in the response for unidirectional first and second order wave loads (LC4), the weak and strong axis bending moment are both close to 10% from each other. Some larger differences are observed in the effective tension along the bridge axes between 5-25% with an average of 20%. However, these standard deviations are observed to fluctuate up to 20% from the average within the six simulated time series due to the strong dependency on the randomly generated wave seed.

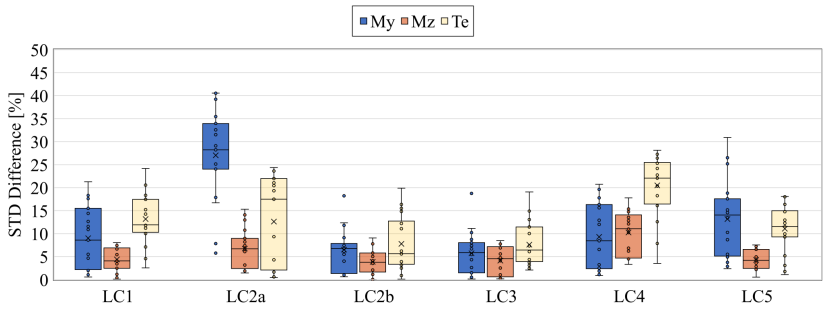

Fig. 14. Box plots of the absolute difference in the standard deviation of the response for load effects in the different load cases. LC2a and LC2b are with SIMO-RIFLEX default and manually specified angles in the spreading function, respectively. The × indicate the average value along the bridge axes.

Including viscous drag using Morison elements in the two models (LC3 and LC5) it seems that the previously listed sources of error are both amplified and reduced by the positive and negative damping, respectively.

CONCLUDING REMARKS

An extensive software-to-software comparison of the dynamic characteristics of an end-anchored floating pontoon bridge is presented. The comparison includes natural frequencies, regular long-crested wave response, response amplitude operators (RAOs), first and second order long-crested stochastic waves, directional spreading and viscous effects of the pontoon heave plate. The responses compared in the two computer programs are the vertical and horizontal displacement, effective tension and weak and strong axis bending moments in the bridge girder.

The natural frequencies compared are based on results from solving the standard eigenvalue problem and show differences below 5%. Noticeable differences in the modeshapes are observed between the two computer programs related to longitudinal rotation of the bridge. The differences are thought to be related to software differences in the implemented methods governing the calculation of the static response, natural frequencies and modeshapes. Particularly the uncertainty in the rotational modes is an important finding and needs further investigation using model tests.

Good agreement between the two computer programs is found for the vertical displacement RAOs along the bridge girder. The peaks in the weak and strong axis bending moment RAOs follow the modal properties of each program and the comparison between the two computer programs is strongly influenced by small differences in their respective modal properties.

Special care was taken when modelling the directional spreading function in the two computer programs. Different methods are by default applied in the two computer programs when distributing the wave direction angles in the spreading function, and an exact replica of the OrcaFlex spreading function was manually specified in SIMO-RIFLEX. The difference in the comparison with default and manual settings are roughly 20% for the average standard deviation of the weak axis bending moment along the bridge.

The effect of second order wave loads are captured well in both computer programs where only the horizontal displacement and the strong axis bending moment are influenced. The first four natural frequencies are captured in the horizontal displacement response spectrum and agree well with the natural frequencies found using the iterative approach.

Including viscous effects in the two computer programs reduces the differences in the weak axis bending moment and can hide potential modelling errors.

Based on the findings in the present paper any future hybrid model tests should expect uncertainties between the mentioned software of roughly 5-15% depending on the response type.

DATA AVAILABILITY STATEMENT

Some or all data, models, or code generated or used during the study are available from the corresponding author by request. These items are specifically software input files and result values shown in the present paper.

ACKNOWLEDGEMENTS

This research was carried out with financial support from the Coastal Highway Route E39 Project of the Norwegian Public Roads Administration. The authors greatly acknowledge this support.

REFERENCES

Cheng, Z., Gao, Z., and Moan, T. (2018a). "Hydrodynamic load modeling and analysis of a floating bridge in homogeneous wave conditions." *Marine Structures*, 59, 122–141.

Cheng, Z., Gao, Z., and Moan, T. (2018b). "Numerical modeling and dynamic analysis of a floating bridge subjected to wind, wave, and current loads." *Journal of Offshore Mechanics and Arctic Engineering*, ASME, 141.

Cheng, Z., Gao, Z., and Moan, T. (2018c). "Wave load effect analysis of a floating bridge in a fjord considering inhomogeneous wave conditions." *Journal of Engineering Structures*, 163, 197–214.

Cummins, W. E. (1962). *The impulse response function and ship motions*. Washington D.C., USA. Report no. DTMB-1661. Accessed January 14, 2020. `https://dome.mit.edu/handle/1721.3/49049`.

DNV (2014). *Wadam - Wave analysis by diffraction and morison theory, SESAM user Manual*. Høvik, Norway. Report no. 94-7100.

Faltinsen, O. M. (1993). *Sea loads on ships and offshore structures*. Cambridge University Press.

Fu, S., Wei, W., Ou, S., Moan, T., Deng, S., and Lie, H. (2017). "A time-domain method for hydroelastic analysis of floating bridges in inhomogeneous waves." Vol. Volume 9: Offshore Geotechnics; Torgeir Moan Honoring Symposium of *International Conference on Offshore Mechanics and Arctic Engineering*, ASME, 1–8 (09).

Hasselmann, K., Barnett, T. P., Bouws, E., Carlson, H., Cartwright, D. E., Enke, K., Ewing, J. A., Gienapp, H., Hasselmann, D. E., Kruseman, P., Meerburg, A., Muller, P., Olbers, D. J., Richter, K., Sell, W., and Walden, H. (1973). "Measurements of Wind-Wave Growth and Swell Decay during the Joint North Sea Wave Project (JONSWAP)." *Deutsche Hydrographische Zeitschrift*, 8.

Karimirad, M., Meissonnier, Q., Gao, Z., and Moan, T. (2011). "Hydroelastic code-to-code comparison for a tension leg spar-type floating wind turbine." *Marine Structures*, 24, 412–435.

Kvåle, K. A., Sigbjörnsson, R., and Øiseth, O. (2016). "Modelling the stochastic dynamic behaviour of a pontoon bridge: A case study." *Computers and Structures*, 165, 123–135.

Langen, I. and Sigbjörnsson, R. (1980). "On stochastic dynamics of floating bridges." *Engineering Structures*, 2(4), 209–216.

Leira, B. J. and Remseth, S. (1990). "Directional effects and multicomponent dynamic response of marine bridges." *Proceedings of the 2nd Symposium on Strait Crossings*, Balkema Publishers Rotterdam, 233–239.

Løken, A. E. and Oftedal, R. A. (1990). "Aspects of hydrodynamic loading and response in design of floating bridges." *Second Symposium on Strait Crossings*, 479–486.

Orcina (2019). *OrcaFlex Documentation*. Accessed January 14, 2020. `https://www.orcina.com/webhelp/OrcaFlex/`.

Pan, Z. Y., Vada, T., and Hanssen, F.-C. W. (2013). "A mesh dependency study for the mean drift forces by pressure integration." *Proceedings of the 32nd International Conference on Ocean, Offshore and Arctic Engineering*, ASME, Nantes, France.

Robertson, A., Jonkman, J., Vorpahl, F., Popko, W., Qvist, J., Frøyd, L., Chen, X., Azcona, J., Uzunoglu, E., Soares, C. G., Luan, C., Yutong, H., Pengcheng, F., Yde, A., Larsen, T., Nichols, J., Buils, R., Lei, L., Nygaard, T. A., Manolas, D., Heege, A., Vatne, S. R., Ormberg, H., Duarte, T., Godreau, C., Hansen, H. F., Nielsen, A. W., Riber, H., Cunff, C. L., Beyer, F., Yamaguchi, A., Jung, K. J., Shin, H., Shi, W., Park, H., Alves, M., and Guérinel, M. (2014). "Offshore code comparison collaboration continuation within iea wind task 30: Phase ii results regarding a floating semisubmersible wind system." *Proceedings of the 33rd International Conference on Ocean, Offshore and Arctic Engineering*, ASME.

Shao, Y.-l., You, J., and Glomnes, E. B. (2016). "Stochastic linearization and its application in motion analysis of cylindrical floating structure with bilge box." *Proceedings of the 35th International Conference on Ocean, Offshore and Arctic Engineering*, ASME, Busan, South Korea.

SINTEF Ocean (2017a). *RIFLEX 4.10.0 Theory Manual*. Trondheim, Norway.

SINTEF Ocean (2017b). *SIMO 4.10.0 Theory Manual*. Trondheim, Norway.

Stansberg, C. T., Ormberg, H., and Oritsland, O. (2002). "Challenges in deep water experiments: Hybrid approach." *Journal of Offshore Mechanics and Arctic Engineering*, ASME, 124, 90–96.

Statens Vegvesen (2016). *Curved bridge navigation channel in south - environmental loading analyses*. Oslo, Norway. Report no. NOT-HYDA-018.

Statens Vegvesen (2017). *Hydrodynamic model tests specification - Floating Bridge Pontoons*. Oslo, Norway. Report no. SBJ-20-C3-SVV-21-TN-002.

Sørum, S. H., Horn, J.-T. H., and Amdahl, J. (2017). "Comparison of numerical response predictions for a bottom-fixed offshore wind turbine." *Energy Procedia*, 137, 89–99.

Tao, L. and Cai, S. (2004). "Heave motion suppression of a spar with a heave plate." *Ocean Engineering*, 31, 669–692.

Villoria, B. (2016). "Floating bridge technology - prediction of extreme environmental load effects." *Proceedings of the 35th International Conference on Ocean, Offshore and Arctic Engineering*, ASME, 1–8.

Viuff, T., Leira, B. J., Xiang, X., and Øiseth, O. (2019). "Effects of wave directionality on extreme response for a long end-anchored floating bridge." *Journal of Applied Ocean Research*, 90.

Viuff, T., Xiang, X., Leira, B. J., and Øiseth, O. (2018). "Code-to-code verification of end-anchored floating bridge global analysis." *Proceedings of the 37th International Conference on Offshore Mechanics and Arctic Engineering*, 1–9.

Xiang, X. and Løken, A. (2019). "Hydroelastic analysis and validation of an end-anchored floating bridge under wave and current loads." *Proceedings of the 38th International Conference on Offshore Mechanics and Arctic Engineering*, ASME, 1–9.

Xiang, X., Svangstu, E., Nedrebø, Ø., Jakobsen, B., Eidem, M. E., Larsen, P. N., and Sørby, B. (2017). "Viscous damping modelling of floating bridge pontoons with heaving skirt and its impact on bridge girder bending moments." *Proceedings of the 36th International Conference on Ocean, Offshore and Arctic Engineering*, ASME, 1–10.

Paper 3

Thomas Viuff, Xu Xiang, Ole Øiseth and Bernt Johan Leira

"Model uncertainty assessment for wave- and current-induced global response of a curved floating pontoon bridge"

Applied Ocean Research, under review.

Preprint.

Model uncertainty assessment for wave- and current-induced global response of a curved floating pontoon bridge

Thomas Viuff[a,*], Xu Xiang[b], Ole Øiseth[c], Bernt Johan Leira[a]

[a]*Department of Marine Technology, Norwegian University of Science and Technology, N-7491 Trondheim, Norway*
[b]*Norwegian Public Roads Administration, N-0667 Oslo, Norway*
[c]*Department of Structural Engineering, Norwegian University of Science and Technology, N-7491 Trondheim, Norway*

Abstract

As for most offshore structures, the design and analysis of long floating bridges utilizes both numerical calculations and experimental tests in ocean basin facilities. Although existing computer programs that handle general multi-purpose offshore structural analysis of slender structures are founded on acknowledged theories within the field and broadly accepted engineering practices, it is always important to verify the calculated results with experiments prior to the final design phase. By comparing a numerical model to large-scale or small-scale experiments it is possible to update the numerical model which helps to improve the accuracy of the predicted response and to understand which parameters are important for any potential future designs. In the present paper an assessment of numerical and physical model uncertainties related to the wave- and current-induced global response of a 830 m long end-anchored floating pontoon bridge is presented. The experiment is for a generic end-anchored floating pontoon bridge with eight floating pontoons carried out in 1989 by SINTEF Ocean and will act as a feasibility study of the coupled hydro-elastic SIMO-RIFLEX computer program. A clear description of the model details is given for reproducibility and experimental data is made available for future references. Several sensitivity studies are performed to quantify the effect of the uncertainty related to different model parameters, which in turn are used to update the numerical model. Finally, a good agreement is found between the measured and calculated response, demonstrating the feasibility of the computer program when applied to the concept of floating bridges and increases the confidence in prior research related to floating bridges based on the investigated computer program.

Keywords: Response amplitude operators, Response spectra, Standard deviations, Experimental data

1. Introduction

Confidence in the accuracy of the calculated dynamic response is imperative to the design of dynamically sensitive structures. For structural concepts such as floating bridges, it is particularly important to assess the uncertainties related to the calculated global response by comparing to either full-scale response of existing bridges or small-scale response from experiments. Furthermore, with the excessive length of the proposed floating bridge concepts for the ferry-free Coastal Highway Route E39 project in Norway of up to 4,600 m, future experiments are rendered infeasible due to scaling requirements and size limitations of existing ocean basins. In these cases it is necessary to perform so-called hybrid tests in the ocean basin, where a specific part of the bridge is scaled within scaling requirements and used to verify a numerical model. The verified numerical model is then used to estimate the response of the entire bridge, making the experimental results from such hybrid tests rely heavily on the performance of computer programs.

Different methods to assess the performance of numerical models have been applied to floating bridge structures over the years. Application of system identification methods for a submerged floating bridge tested in an ocean basin was described by Larssen et al. [1], where the modal parameters were identified using a Covariance Block Hankel Matrix method and physical model parameters were estimated based on measured response and maximum likelihood estimates. In more recent years Petersen et al. [2] described a sensitivity-based finite element calibration method based on an analytical sensitivity matrix, which takes into account frequency-dependent system matrices due to the wave-structure interaction. By use of a system identification method with full-scale measurements of a floating pontoon bridge, the natural frequencies and mode shapes are calibrated. Kvåle et al. [3] investigated the feasibility of three different system identification methods for the same floating pontoon bridge and found that a Covariance-driven Stochastic Subspace Identification method was the most promising method, although the high damping levels made the procedure challenging. For most general multi-purpose computer programs used in the offshore sector, system identification methods as the ones described above are not an integrated option and the model uncertainty assessment is instead carried out using sensitivity studies of the most important physical parameters.

In the present paper a model uncertainty assessment of the coupled hydro-elastic SIMO-RIFLEX [4, 5] program is presented. Previously, the computer program has been compared to others used in the offshore industry for different applications, see e.g. [6–9], but no information is available regarding exper-

*Corresponding author. Email address: thomas.h.viuff@ntnu.no

imental verification of the computer program when applied to floating pontoon bridge structures. The present paper compares a numerical model made in SIMO-RIFLEX version 4.14 to experiments carried out in 1989 by MARINTEK (now SINTEF Ocean) for a generic floating bridge structure. The description of the experimental model and the associated meassured response are based on two internal reports [10, 11] commissioned by the Norwegian Public Roads Administration (NPRA) and have been used in previous comparisons with other computer programs in the past, see Løken and Oftedal [12] and Xiang and Løken [13], who also verified the calculated hydrodynamic properties of the pontoons with experiments. In [12] the numerical model was made up of hydrodynamic properties of the pontoons found using 3-dimensional radiation-diffraction theory, transferred to a linear beam model by an in-house algorithm. The dynamic equation was solved using a direct frequency-response method with one solution per wave frequency. Stochastic response was later derived using statistical methods in the post-processing of the data and all results were hence based on linear theory without including slow-drift, viscous drag or current. In [13] a comparison of the results from three different numerical models was conducted. The three models applied a frequency-domain and a time-domain solution with no hydrodynamic interaction between the pontoons and a time-domain solution that included hydrodynamic interaction effects. Based on the comparisons the hydrodynamic interaction was found to have an effect on the vertical response of the bridge and for some frequencies fitted better to the experiments for beam sea. They also found that adding current to the numerical model had a dampening effect on the response opposite to the amplifying effect seen in the measured response.

Although the previous comparisons exists, they mostly describe the experimental model and the findings of the comparison in overall terms with selected results for the comparison. Instead, the present paper gives a more detailed description of the experimental model and tries to show as much data as possible in the comparison. A meticulous case-by-case approach is employed in order to clarify the effect of different model uncertainties on the numerical model, including sensitivity tests on static response and natural frequencies in order to verify the fundamental properties of the numerical model. By manually implementing an iterative method to account for the frequency-dependent added mass of the pontoons, a closer match with the natural frequencies seen in measured response spectra is obtained, leading to a more trustworthy calibration of the the numerical model than in the previous comparison studies.

By validating the coupled hydro-elastic SIMO-RIFLEX program to the experiments for a generic floating pontoon bridge, the present paper aims to 1) improve the confidence in the already existing body of research related to floating bridges based on the computer program, 2) increase the confidence in the performance of the program when considered for any potential future hybrid tests related to the proposed long floating pontoon bridges commissioned by the NPRA and 3) to be used as a reference for future computer program comparisons.

Table 1: Original bridge girder cross-sectional properties [10]

Property	Unit	Full scale
Mass	[ton/m]	5.46E+00
Moment of inertia [11]	[ton·m^2/m]	6.53E+00
Radius of gyration [11]	[m]	1.09E+00
Area	[m^2]	1.94E+00
Second moment of area (X_G)†	[m^4]	1.02E-01
Second moment of area (Y_G)	[m^4]	3.89E-01
Second moment of area (Z_G)	[m^4]	9.10E-01
Axial stiffness‡	[kN]	5.34E+09
Weak axis bending stiffness‡	[kN·m^2]	1.07E+09
Strong axis bending stiffness‡	[kN·m^2]	2.51E+09
Torsional stiffness§	[kN·m^2/rad]	1.05E+08

† Based on measurements in small-scale

‡ Based on E = 69.0 GPa for aluminium used in the model test

§ Based on G = 22.5 GPa for aluminium used in the model test

2. Experimental setup

The floating bridge is modelled in scale 1:40 and values given in this section will refer to full scale. The bridge consists of a single horizontally curved beam (i.e. the bridge girder) supported by eight pontoons as illustrated in Fig. 1. The bridge is 830 m long with an arch length of 844.8 m and has a horizontal radius of 1,300 m. The center-line of the bridge girder is located at 8.8 m above the mean water level (MWL).

Three coordinate systems are used in the model, all of which are right-handed with the positive Z axes pointing upwards; the global Earth-fixed coordinate system ($O_EX_EY_EZ_E$) located at the middle of the bridge at the MWL, the local pontoon coordinate system ($O_PX_PY_PZ_P$) located at the center of the pontoons at the MWL following the orientation of each individual pontoon, and the local bridge girder coordinate system ($O_GX_GY_GZ_G$) located at the center-line of the bridge girder cross-section with the Y_G axis always perpendicular to the bridge girder and with X_G axis as a tangent to the curve.

The bridge girder consists of a single cross-section shaped as a cross with properties listed in Tab. 1. The length of the bridge girder is made up of four sections. The two sections closest to the middle are both 200 m long and the length of the other two is 222.4 m. Bending- and shear force gauges are inserted at the three assembly points between the four bridge sections to measure the bending moment around the local X_G and Y_G axes and shear force in the direction of those same axes. The mass of each gauge is 289.9 ton and the dimensions are $L \times W \times H$ = 12 m × 38 m × 16 m. The bending and torsional stiffness of the three gauges is relatively large compared to the bridge girder, although the details are unclear [10]. The two ends of the bridge (End 1 and End 2) are fixed in all translational degrees of freedom (DOFs). Torsional rotation around the X_G axis is restricted, while rotational springs with a spring stiffness of 192 MNm/deg are introduced for bending about the two other axes and the end forces are measured using a 6-axis force transducer at each end.

Eight identical pontoons are distributed along the bridge

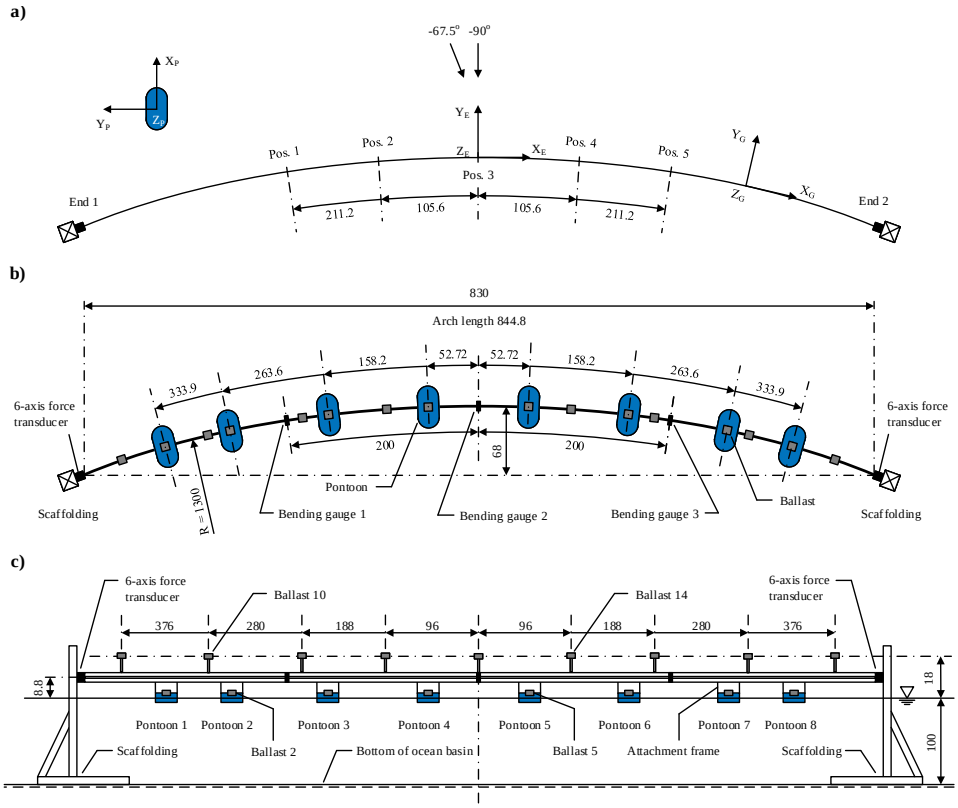

Figure 1: Sketch of the experimental floating bridge model setup with all dimensions in m referring to full scale. a) Top view of model with location of measurement positions Pos. 1 to 5, global coordinate system ($O_EX_EY_EZ_E$) with origo at the mean water line and Z_E pointing up, local pontoon coordinate system ($O_PX_PY_PZ_P$) with origo at the mean water line and Z_P pointing up and local bridge girder coordinate system ($O_GX_GY_GZ_G$) with origo at the center line of the bridge girder and Z_G pointing up and wave directions θ defined according to the positive X_E-axis. b) Top view of model with locations of instrumentation and pontoons along the bridge. c) Side view of model with locations of traffic mass (ballast) along the bridge (horizontal distances are given as arch length). Sketch inspired by [12].

with varying distance from each other as sketched in Fig. 1. The pontoon geometry, projected onto the horizontal plane, is made up of a rectangle and two half circles. The total length, width and height of each pontoon is 45 m, 22 m and 4.3 m, respectively. From left to right the pontoons are numbered 1 to 8. The total distance of each pontoon from the middle of the bridge (the location of the $O_EX_EY_EZ_E$ coordinate system) is given in Fig. 1 as arch length values. Each pontoon is rotated so as the positive X_P axis is perpendicular to the curvature of the bridge girder, pointing away from the center of the arch and the corresponding properties are listed in Tab. 2. The pontoons are rigidly connected to the bridge girder using attachment frames. The draft of the pontoons is the same and is based on freshwater density as freshwater is used in the model tests.

Traffic load is included in the experimental setup using ballast at 17 different locations along the bridge girder, of which eight (Ballast 1-8) are located in the center of pontoon 1-8 at a height 1.816 m above the MWL. The other nine (Ballast 9-17) are spread out along the bridge girder at a height of 18.0 m above MWL corresponding to 9.2 m above the bridge girder center-line as illustrated in Fig. 1 and numbered from left to right. The mass properties of the traffic loads are listed in Tab. 3.

The motion response is measured in the experimental model at the five positions Pos. 1, 2, 3, 4 and 5 illustrated in Fig. 1 located at the 1/4, 3/8, 1/2, 5/8 and 3/4 spans along the arch length of the bridge, respectively. The force response is measured at the two ends (End1 and End2) as well as at Pos. 1, 3 and 5. A wave direction of θ = -67.5° and -90° relative to the X_E axis is used, defined as positive when being counter-clockwise. In the verification of the numerical model the same wave directions and measurement points are used.

Table 2: Pontoon properties without ballast [10]. Mass values refer to the center of gravity (COG), stiffness values are defined relative to the local pontoon coordinate system ($O_P X_P Y_P Z_P$) and the location of the COG is measured from the keel.

Property	Unit	Full scale
Mass†	[ton]	1.20E+03
Roll inertia	[ton·m^2]	4.31E+04
Pitch inertia	[ton·m^2]	1.43E+05
Yaw inertia	[ton·m^2]	2.35E+05
Draft‡	[m]	2.65E+00
COG	[m]	3.30E+00
Displacement‡	[ton]	2.29E+03
Roll water plane stiffness	[kN·m^2/rad]	2.94E+05
Pitch water plane stiffness	[kN·m^2/rad]	1.17E+06
Heave stiffness	[kN/m]	8.70E+03

† The attachment frame is included in the pontoon mass

‡ Based on freshwater density

Table 3: Mass properties and vertical position of traffic load ballast and bending- and shear force gauges [10]

Instrumentation	Z_E [m]	Mass [ton]
Bending gauge 1-3	8.80E+00	2.90E+02
Ballast 1 & 8	1.82E+00	4.51E+02
Ballast 2 & 7	1.82E+00	1.18E+02
Ballast 3-6	1.82E+00	5.06E+01
Ballast 9-17	1.80E+01	2.13E+02

2.1. Tests carried out in the ocean basin

Several tests were carried out in the ocean basin, including static tests, decay tests, current, regular long-crested waves, irregular long-crested waves, short-crested waves, and a combination of current and irregular long-crested waves. The response measured for the listed test cases was presented as average values, standard deviations, maxima, minima, zero-up crossings, response spectra and response amplitude operators (RAOs) for the different responses measured at the seven positions along the bridge girder. Of the listed tests only results from selected tests are stated in [10]. Extra information is found in [11]. Of the given experimental results only some of them are reproduced in the present paper due to space considerations[1].

The static tests applied loads at the three positions along the bridge in both negative Z_G and Y_G direction and measured the translational displacements in the same three positions along the bridge each time.

Tests with regular waves were conducted for wave directions $\theta = -90°$ and -67.5°, respectively, and the wave periods used for the RAOs were 3.98 s, 4.49 s, 4.93 s, 5.44 s, 6.01 s, 7.02 s, 8.03 s, 8.92 s, 10.44 s, 12.02 s and 13.41 s, of which the three lowest regular waves are close to the limits of the capability of the ocean basin facility [14].

[1] An electronic appendix with most of the available experimental data is available upon request

Table 4: Measured wave parameters for irregular wave tests [10]

Test no.	θ [°]	U_c [m/s]	H_s [m]	T_p [s]	$\gamma^\dagger$ [-]	s [-]
530	-90.0	-	1.04	4.81	3.04	-
531	-90.0	-	1.44	4.93	3.33	-
532	-90.0	-	1.32	6.89	2.80	-
533	-90.0	0.92	0.96	4.74	3.19	-
534	-90.0	0.92	1.64	4.87	3.21	-
540	-90.0	-	0.96	4.87	3.62	2

† The peak enhancement factor γ is based on an assumed 1-to-1 relationship with the measured spectral peakedness parameter Q_P defined in [16]

The irregular wave tests compared in the present paper related to the hydro-elastic model tests are listed in Tab. 4. These tests include both long-crested waves, short-crested waves and finally, current and long-crested waves. The irregular waves generated in the experiments are assumed to be governed by the 3-parameter JONSWAP [15] wave spectum and the $\cos^s \theta$ spreading function based on information in [11, 12].

2.2. Uncertainties in experiments

As expected there are some uncertainties associated with tests carried out in the ocean basin laboratory related to accuracy in the measurements, precision in the positioning of the measurement equipment, wave maker proficiency, post-processing including signal filtering, and so on. The final accuracy of the experiments is estimated to 5-10% [12].

3. Numerical model

The numerical model illustrated in Fig. 2 is made in the coupled hydro-elastic program SIMO-RIFLEX. The theoretical background for all of the applied methods in the program is too extensive to cover in the present paper and instead only the most relevant information is given below for the sake of brevity. For more elaborate details the reader is referred to [4–6, 17]

The program utilizes the finite element method (FEM) to idealize the structural system as a combination of linear beam elements and 6 degree of freedom (DOF) bodies with hydrodynamic properties and is able to solve static equilibrium equations, the eigenvalue problem as well as dynamic response in the time domain.

Frequency-dependent hydrodynamic properties of the bodies are included in the solution of the equation of motion through the hybrid frequency- and time-domain equation [18].

$$q_j^{exc}(t) = \sum_{k=1}^{6} \left[M_{jk} + A_{jk}^{\infty} \right] \ddot{u}_k(t) + D_{jk}\dot{u}_k(t) + \left[K_{jk} + C_{jk} \right] u_k(t) + \int_0^{t_{mem}} k_{jk}(t-\tau)\dot{u}_k(\tau)d\tau \quad (1)$$

Here the structural mass, stiffness and damping properties are collected in the M_{jk}, K_{jk} and D_{jk} terms, respectively. The

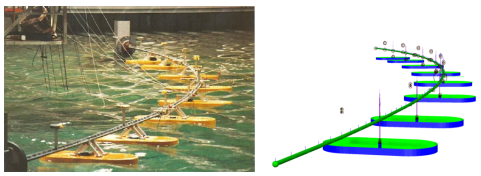

Figure 2: Experimental model [13] (left) and numerical model (right) of the generic floating bridge

notation $q_j^{exc}(t)$ is the wave excitation load on the 6 DOF bodies, including both linear first order wave load $q_j^{(1)}(t)$ and viscous drag load $q_j^{(d)}(t)$, as functions of time t. The displacement response and the corresponding first and second order derivatives of time are given by the notations $u_k(t)$, $\dot{u}_k(t)$ and $\ddot{u}_k(t)$. The angular frequency is denoted ω and the indices are defined according to the body-fixed pontoon coordinate system with $j = 1, 2, ..., 6$ constituting surge, sway, heave, roll, pitch and yaw, respectively. The hydrostatic stiffness of the 6 DOF bodies are included in the term C_{jk}. The frequency-dependent potential damping is given by $b_{jk}(\omega)$. The frequency-dependent added mass $A_{jk}(\omega) = A_{jk}^{\infty} + a_{jk}(\omega)$ is separated into a constant added mass at infinite frequency A_{jk}^{∞} and a frequency-dependent part $a_{jk}(\omega)$. The hydrodynamic properties of the 6 DOF bodies are included through the retardation function $k_{jk}(t)$ seen in Eqn. (2). This retardation function is multiplied with the response velocity for the same point in time and the resulting product is integrated from time zero to the "memory" time t_{mem} with a time lag τ.

$$k_{jk}(t) = \frac{1}{2\pi}\int_{-\infty}^{\infty}\left[b_{jk}(\omega) - i\omega a_{jk}(\omega)\right]e^{i\omega t}d\omega \qquad (2)$$

In the above, the term i is the imaginary unit. The hydrodynamic properties of the pontoons are calculated in Wadam [19] based on 3-dimensional potential radiation and diffraction theory and the boundary element method (BEM) using a panel model of the pontoon geometry up to the MWL as seen in Fig. 3. The water density is set to 1.000 ton/m^3 as that of freshwater and the draft of the pontoon is the same as in the experiment using freshwater. This is done to make the experiment and the numerical model as similar as possible, however, for any proper design in full scale, values corresponding to saltwater should be used. Figure 3 also shows the converged hydrodynamic coefficients based on the described panel model. The hydrodynamic interaction between the pontoons is neglected in the hydrodynamic analysis as a first approximation and no second order effects are considered due to no significant effects from slow drift excitation observed in the experiments [12].

3.1. Modelling first order wave loads

The time-dependent first order wave load $q_j^{(1)}(t)$ is generated using the Monte Carlo simulation method in Eqn. (3) based on a fast Fourier transformation of the real part $\Re(\cdot)$ of the directional wave spectrum $S_\zeta(\omega_m, \theta_n)$ and the first order wave

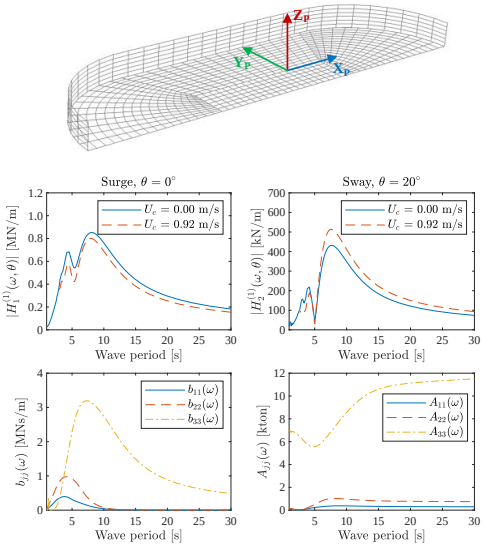

Figure 3: Panel model of pontoon with local pontoon coordinate system (top) and hydrodynamic coefficients of pontoon 1 (bottom)

transfer function $H_j^{(1)}(\omega_m, \theta_n)$. The directional wave spectrum is simplified as the product of the unidirectional wave spectrum $S_\zeta(\omega_m)$ and the directional spreading function $D_\zeta(\theta_n)$.

$$\begin{aligned} q_j^{(1)}(x,y,t) = &\Re\sum_{m=1}^{N_\omega}\sum_{n=1}^{N_\theta}\sqrt{2S_\zeta(\omega_m)D_\zeta(\theta_n)\Delta\omega_m\Delta\theta_n} \\ &\left|H_j^{(1)}(\omega_m,\theta_n)\right|\exp\left[i\left(\varepsilon_{nm}+\varphi_{H_{jnm}^{(1)}}\right)\right] \\ &\exp\left[i\left(\omega_m t - k_m x\cos(\theta_n) - k_m y\sin(\theta_n)\right)\right] \end{aligned} \qquad (3)$$

Here θ_n is the wave direction, ε_{nm} is a randomly generated phase angle, k_m is the wave number, x and y are coordinates of the pontoon bodies in the Earth-fixed global coordinate system and $\varphi_{H_{jnm}^{(1)}}$ is the phase angle of the first order wave force transfer function. The unidirectional wave spectrum is modelled as the 3-parameter JONSWAP wave spectrum with parameters listed in Tab. 4. See [4] or [6] for the implementation in SIMO-RIFLEX. The directional spreading function $D_\zeta(\theta)$ in Eqn. (4) is based on the Gamma function $\Gamma(\cdot)$, the main wave direction θ_0 and the spreading exponent s.

$$D_\zeta(\theta) = \frac{1}{\sqrt{\pi}}\frac{\Gamma(\frac{s}{2}+1)}{\Gamma(\frac{s}{2}+\frac{1}{2})}\cos^s(\theta-\theta_0), \quad |\theta-\theta_0| \le \frac{\pi}{2} \qquad (4)$$

3.2. Modelling viscous loads

Viscous drag loads are included in the numerical model using Morison elements at the center of each pontoon and Eqn. (5), which is the drag term in the semi-empirical Morison equation.

$$q_j^{(d)}(t) = \frac{1}{2}\rho C_j^d A_j \dot{u}_r(t)\,|\dot{u}_r(t)| \tag{5}$$

Here ρ is the water density, C_j^d is the drag coefficient, A_j is the cross-sectional area, $\dot{u}_r(t)$ is the relative velocity between the pontoon and the water and the index j is defined according to the body-fixed pontoon coordinate system with 1, 2 and 3 or interchangeably x, y and z indicating surge, sway and heave. The drag coefficients are based on values from the literature. Shao et al. [20] has described a numerical investigation of the wave frequency pontoon response using both BEM and 2-dimensional computational fluid dynamics (CDF) software, and compared the results to experiments. The vertical drag coefficient is estimated to $C_z^d = 5.0$ for a similar pontoon shape under comparable sea conditions. The horizontal drag coefficients are less understood and are in the present paper estimated to be $C_y^d = 1.0$ and $C_x^d = 0.5$. The estimates for the horizontal drag coefficients are close to the values from DNV-RP-C205 [21] for Reynolds numbers close to 1e5 and values from Delany and Sorensen [22] for Reynolds numbers close to 2.3e6, although both differ with roughly ±50%. However, based on characteristic lengths of the pontoon of 22 and 45 m, a water temperature of 5 degrees and a measured current of 0.92 m/s in the experiment, the Reynolds numbers in the present study are in the proximity of 1.3e7 and 2.7e7, respectively, making the estimates somewhat uncertain.

3.3. Modelling structural damping

The structural damping ratio of the floating bridge model is estimated to $\xi_{struc} = 0.32\%$ based on the aluminium used for the bridge girder cross-section [11]. The same structural damping ratio is achieved in the numerical model for the frequency range of the natural periods and the wave spectrum using Rayleigh damping with a mass proportional damping coefficient $\mu = 0.0031$ and a stiffness proportional damping coefficient $\lambda = 0.0024$.

3.4. Wave-current interaction and second order effects

By use of the drag coefficients described above, the viscous effect of the pontoons is accounted for when computing the response for cases with current. For large-volume structures however, the wave-current interaction also changes the hydrodynamic coefficients. The effect on the first order wave force transfer function is accounted for in Wadam for each of the pontoons by specifying different forward speed vectors corresponding to the rotation of each pontoon and then solving the diffraction problem anew. In the applied version of Wadam it is not possible to solve the new radiation problem and for this reason changes to the added mass and potential damping are not accounted for. In the case with current and $T_p \approx 4.9$ s the ratio $U_c\omega_e/g \approx 0.135 \leq 1/4$ meaning that the current is considered small and the free-surface condition can be approximated with success in the BEM [23]. In the previous notation U_c is the current, $\omega_e = \omega_0 + \omega_0^2 U_c \cos\beta/g$ is the wave encounter frequency, ω_0 is the angular wave frequency, β is the angle between the current and wave direction and g is the acceleration of gravity.

Although it was found by [24] that a current of 1 m/s increases the wave drift force by 50% for large-volume structures, the present paper does not include any second order effects. This choice is based on the fact that the contribution from the low-frequency response in the measured values was only 1-5% depending on the type of response [11]. By computing the response of test 534 listed in Tab. 4 with and without including second order effects such as wave drift forces and wave drift damping, the same 1-5% difference was found.

3.5. Other modelling details

The element length varies along the bridge girder due to modelling consideration such as the location of position gauges, pontoons and ballast, resulting in an element length of roughly 10 m corresponding to a total of 96 elements. The chosen number of elements is verified by an initial element length convergence study. The boundary conditions at the two ends are modelled using rotational springs and a combination of rigid body connections and nodal bodies are used to model the traffic load (ballast) above the bridge girder.

The connection between the bridge girder and the pontoons are modelled as rigid body connections to account for the stiff attachment frame used in the model test to connect the bridge girder and the pontoons. A buoyancy force is introduced in the center of buoyancy (COB) at each pontoon equivalent to the mass of the displaced water and in order not to count the roll and pitch restoring effect twice in the coupled analysis the buoyancy terms are removed from the hydrostatic stiffness matrix of the pontoon. The traffic load (ballast) located on the pontoons are modelled by modifying the structural mass matrix and the center of gravity (COG) of the pontoons.

3.6. Solution procedures

The static solution procedure is based on a Newton-Raphson iterative procedure to find convergence for incremental load steps. Natural periods and mode shapes are found using the Lanczos Method and includes hydrostatic stiffness and added mass at infinite frequency of the pontoons by default. The hybrid frequency- and time-domain equation given in Eqn. (1) are solved by applying an incremental formulation of the dynamic equilibrium equation and using the Newmark β-family integration method [5]. A slight amount of numerical damping is added by setting the integration parameters $\beta_{int} = 0.256$ and $\gamma_{int} = 0.505$. This facilitates an earlier convergence and the effect on the dynamic response is negligible. The time-domain solution is made stable by ramping up the load for 100 s and utilizing a time step of 0.01 s based on a time step convergence study.

4. Results and discussion

The following sections contain a comparison of the numerical model with static tests conducted in the experiments, as well as a modal comparison of some of the natural periods observed in the experimental model, which are used to tune the numerical model. The RAOs for two wave directions are compared to the

numerical results and a sensitivity study is performed for the drag coefficients. Stochastic response for both long-crested and short-crested waves is compared for the different tests listed in Tab. 4, including standard deviations and response spectra. Finally, the effect of applying a current is investigated and compared to the experiments.

The sensitivity towards different parameters is discussed in the following sections due to limited information available from the roughly 30 year old reports. The parameters are the modulus of elasticity E of the bridge girder cross-section material, orientation of the applied static load, rotational spring stiffness value at the two ends of the bridge, the weak and strong axis bending stiffness EI_{Y_G} and EI_{Z_G} of the bridge girder, torsional stiffness GI_{X_G}, the radius of gyration r_{gyr} of the bridge girder, the wave direction θ, the drag coefficients values, and the structural damping ratio ξ_{struc}.

4.1. Verification of static response and modal properties

In the experiment a total of six static tests were carried out, three of which were conducted by placing weights equivalent to $F_{Z_G} = -6240$ kN at Pos. 1, 3 and 5. The other three used strings attached at the same three positions to pull with a static force of $F_{Y_G} = -5952$ kN in the horizontal direction perpendicular to the bridge axis. The relative displacement between the initial static position and the position when the loads were applied is illustrated in Fig. 4 for both experimental and numerical response. In the experimental setup the horizontal loads were not perfectly perpendicular to the bridge girder, with an offset OS of 40-80 m from the center reported in [10]. An offset of 12 m from Pos. 3 in the positive X_G direction is also reported for the applied horizontal force in the static tests, which is included in the numerical model.

Based on a comparison of the static displacements, the sensitivity towards the modulus of elasticity of the bridge girder cross-section E of roughly 1.6% is checked and found insignificant. Similarly, a low sensitivity to the offset OS in the horizontal force direction is found. The static comparison shown in Fig. 4 implies that the experimental model is slightly stiffer than the numerical model in both the vertical and horizontal directions. The relatively large differences in the measured and calculated displacements of the structure is thought to be related to the, in relative terms, larger stiffness of the bending- and shear force gauges. Another less likely reason is uncertainty in the spring stiffness value of the inserted rotational springs at the two ends. To check both scenarios, a sensitivity test is carried out for both bridge girder bending stiffness and the rotational spring stiffness at the two ends. The bridge girder bending stiffness is changed with a modifier f_{EI} of 1.00, 1.10 and 1.20 multiplied with the original cross-section properties listed in Tab. 1. Likewise, the rotational spring stiffness at the two ends is changed with the modifier f_{BC} of 1.00, 2.00 and 4.00 multiplied with the original rotational spring stiffness of 192 MNm/deg. A change in the horizontal displacement is observed when changing f_{BC}, while the vertical displacement is almost unchanged. On the contrary, both the horizontal and vertical static response is sensitive to changes of f_{EI}. Based on the value of f_{EI} and f_{BC},

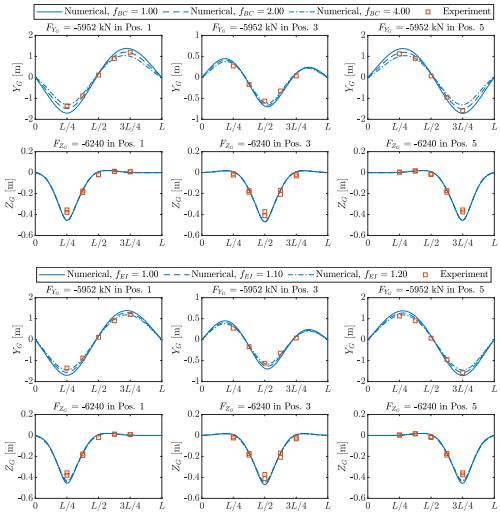

Figure 4: Displacement comparison for different static conditions in the five measured positions in the model test [10] and the numerical model along the arch length L of the bridge. Sensitivity study in the modifier f_{BC} applied to the rotational spring stiffness at the boundary conditions (top) and sensitivity study in bridge girder bending stiffness modifier f_{EI} (bottom). Base case: OS = 0 m, f_{BC} = 1.00 and f_{EI} = 1.00.

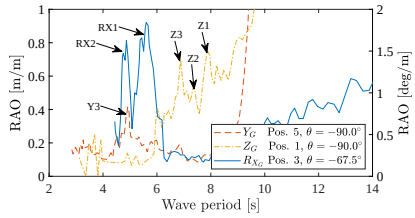

Figure 5: Observable modes of the experimental model [10, 11] in the displacement and rotation RAOs based on long-crested irregular waves

the structure is most sensitive to changes in the bridge girder bending stiffness properties.

The modal properties are estimated in the numerical model using added mass at infinite frequency matrices for the pontoons. By manually running an iterative procedure the modal comparison can be forced to include the frequency-dependent added mass of the pontoons: a) calculate the natural angular frequencies based on the added mass at infinite frequency matrices of the pontoons, b) update the added mass at infinite frequency matrices to include the added mass at the newly calculated natural angular frequencies, c) continue step a, and b until the difference between the angular natural frequencies used to obtain the input added mass and the natural frequencies obtained from the last run are within a specified tolerance level. The final natural periods obtained from this iterative procedure are listed in Tab. 5. The notation Y2 in the table is for the

first horizontal mode consisting of two half sine waves, Z1 is the first vertical mode consisting of a single half sine wave and RX1 is the first rotational mode with a single half sine wave. The natural periods of the experimental model are based on decay tests and vertical and horizontal displacement RAOs from test 532, see Fig. 5. The natural period of the first horizontal mode Y2 is compared to the model test value of 9.96 s and shows an original difference of roughly 7%. The same difference is observed between the second horizontal mode Y3 and the model test value of 4.95 s based on response spectra for test 532. Changing the bending stiffness of the bridge girder cross-section with the modifier $f_{EI} = 1.18$ corresponding roughly to an increase of the frequency by a factor of 1.07^2 gives a good match for the first two horizontal modes. The vertical modes are also changed, although not as much, due to the relatively large pontoon heave stiffness. The persisting difference in the natural periods of the vertical modes could be related to imperfections of the pontoon shapes in the experiment. The natural periods of the rotational modes are, as expected, practically unchanged by the mentioned modifications.

To obtain the same match in the first horizontal mode the rotational spring stiffness at the two ends of the bridge has to be changed with a modifier $f_{BC} = 1.85$ with only slight changes to the other modes. The natural periods of the first two torsional modes are roughly 7% lower than those observed in the RAO for torsion. This does not fit with the relatively larger torsional stiffness of the bending and shear force gauges mentioned earlier and when changing the torsional stiffness with ±20% the natural period of the first torsional mode is changed by less than 1%. For this reason, no modification of the torsional stiffness has been done. Similarly, no change to the radius of gyration of the bridge girder cross-section has been made. Assuming that the mass of the inserted shear and bending gauges is equally distributed over their dimensions, the radius of gyration of the bridge girder is increased by 46%, which is an insignificant change when compared to the contribution from the pontoons. Based on the previous sensitivity studies in both static and eigenvalue calculations, the bridge girder bending stiffness modifier is kept at $f_{EI} = 1.18$ and the rotational spring stiffness modifier at the two ends is kept at $f_{BC} = 1.00$ unless otherwise stated.

4.2. Potential damping from pontoons

With a structural damping ratio $\xi_{struc} = 0.32\%$ the potential damping from the pontoons are more likely to influence the amplitude of the response at resonance periods in general. A potential damping ratio ξ_{pot} can be found using Eqn. (6).

$$\xi_{pot,n} = \frac{N_p \cdot B(\omega_n)}{2\left[M_S + N_p \cdot A(\omega_n)\right]\omega_n} \tag{6}$$

Where, M_S is the total dry mass of the structure, $B(\omega_n)$ and $A(\omega_n)$ are the hydrodynamic potential damping and added mass at the angular frequency ω_n for mode n, respectively, and N_p is the number of pontoons. Based on Eqn. (6) together with the natural periods listed in Tab. 5, the structural mass and the hydrodynamic added mass and potential damping shown in Fig. 3, the potential damping ratio at the first four vertical modes is roughly 20% and are thought to be unaffected by other types of damping in the model. Instead, the potential damping ratios for the first and second horizontal mode is roughly 1.2% and 5%, respectively, and the response amplitudes at these two periods are more likely to be influenced by a correct modelling of the damping in the system.

Table 5: Comparison of modal properties of the experimental model with that of the numerical model using different modifiers f. Frequency-dependent added mass is taken into account manually.

Mode	$f_{BC} = 1.00$ $f_{EI} = 1.00$		$f_{BC} = 1.00$ $f_{EI} = 1.18$		Exp. [10, 11] Value	Diff
n	Shape	[s]	Shape	[s]	[s]	[%]
1	Y2	10.64	Y2	9.95†	9.96	-0.1
2	Z1	7.89	Z1	7.88	7.85	0.4
3	Z2	7.70	Z2	7.67	7.35	4.4
4	Z3	7.17	Z3	7.08	6.87	3.1
5	Z4	6.24	Z4	6.07	-	-
6	Y3	5.35	RX1	5.12	5.53	-7.4
7	RX1	5.13	Y3	4.97	4.95	0.4
8	Z5	5.10	Z5	4.88	-	-
9	RX2	4.58	RX2	4.56	4.82	-5.4
10	RX3	4.02	RX3	3.99	-	-
11	Z6	3.93	Z6	3.72	-	-
12	RX4	3.72	RX4	3.68	-	-
13	RX5	3.26	RX5	3.24	-	-
14	Z7	3.04	RX6	2.92	-	-

† Numerical decay test returns 9.94 s

4.3. Regular wave global response

The RAOs from the model test are compared with the computed response in Fig. 6 for the two ends and at Pos. 1, 3 and 5 and show that the computed response in general follow the experiments well. Even at the low periods where a high uncertainty is present in the experimental results as described above, the behaviour is captured to a satisfying level.

Due to imperfections in the experimental tests such as the accuracy of the orientation of the model and the long-crested regular wave generation, the first horizontal mode Y2 is excited, which is not the case for the numerical model where the mode is cancelled out due to the idealised symmetry of the bridge. Based on [10], the accuracy in the wave direction in the experimetns is 0.4°. By changing the wave direction in the numerical model by 0.5°, the mode is observed in several of the computed RAOs. The fact that this floating bridge concept is highly sensitive to the wave direction is not a new finding but has been discussed in many previous studies, see e.g. [17, 25, 26].

The weak axis bending moment M_{Y_G} shows a good comparison with a clear coupling to the vertical displacement around the first four vertical modes. The strong axis bending moment M_{Z_G} follow the behaviour of the horizontal displacement RAOs

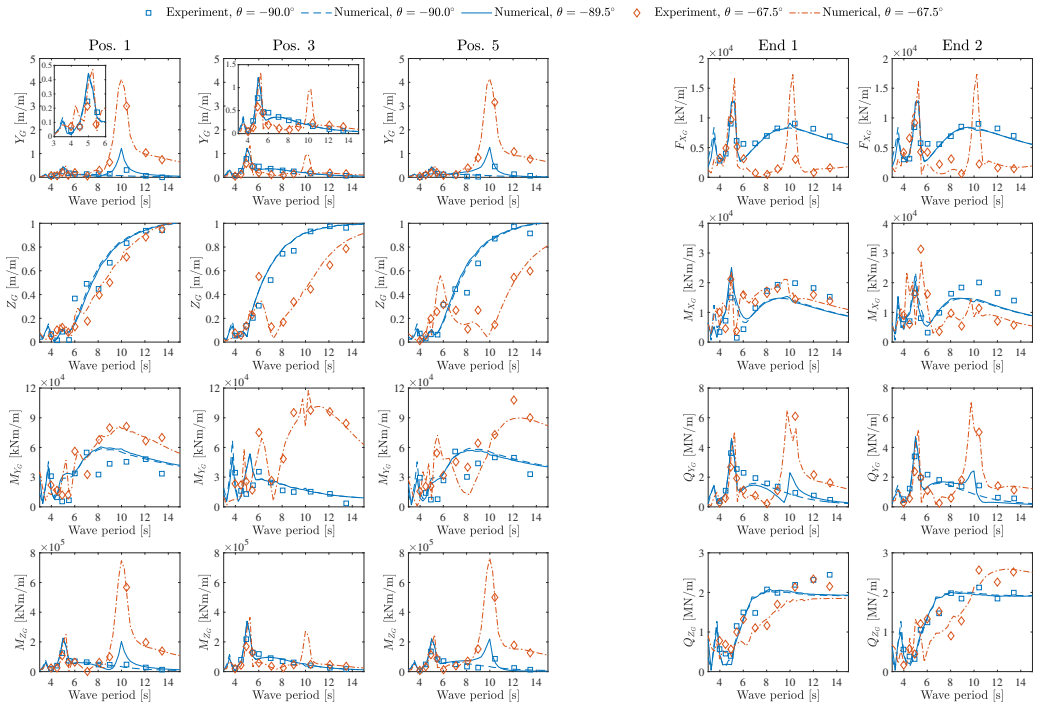

Figure 6: Comparison of regular wave RAOs at Pos. 1, 3 and 5 (left) and End 1 and 2 (right) for two wave directions θ in experiment [10, 11] and numerical model

and show a bump in the amplitude at 10 s corresponding to mode Y2. This bump is also present in the RAO for R_{X_G} at Pos. 3 and is thought to be a result of the coupling between pitch of the pontoon and the horizontal motion of the bridge girder.

The axial force F_{X_G}, the torsional moment M_{X_G}, the vertical shear force Q_{Z_G} and horizontal shear force Q_{Y_G} RAOs are shown for the two ends of the bridge and overall show a good match for both wave directions. The torsional moment is slightly under predicted by the numerical model but follow the same general behaviour as that of the experiment.

Other results such as the vertical and horizontal shear force RAOs at Pos. 1, 3 and 5 are also compared but omitted here due to space considerations. Similar to the torsional moment, the shear force is slightly lower than the measured values with a difference of up to 30% for $\theta = -67.5°$. In the case of the measured shear forces, a reported uncertainty of up to 64 kN persists in the measurd values [10]. With low shear force values at the middle of the bridge in beam sea, the uncertainty makes up roughly 50% of the measured response.

Other possible reasons for discrepancies is the hydrodynamic interaction between the pontoons not being taken into account in the numerical model. Xiang and Løken [13] have shown that for this particular bridge the hydrodynamic interaction has an impact on the vertical motion RAOs in a numerical model created with the software OrcaFlex [27].

4.3.1. Sensitivity towards drag coefficient values

Some uncertainty is tied to the drag coefficients used to model the viscous drag around the pontoons. To evaluate the importance of these coefficients a sensitivity study is performed using ±50% of the initial values for both -90.0° and -67.5° wave directions. Only small changes in the structural response is present at the lower wave periods and in general an insignificant effect is found. This is due to the relatively high amounts of potential dampening from the pontoons. Another reason is the relatively small vertical motion of the bridge, resulting in low viscous damping effects.

4.4. Long-crested irregular wave global response

A comparison between standard deviations of the measured response and the computed response based on three different wave directions is listed in Tab. 6. The factor in the table is defined as the standard deviations of the computed response divided with the corresponding measured values and the computed standard deviations are based on 10 3-hour simulations in order to achieve convergence.

As a first observation, the horizontal response types Y_G, M_{Z_G} and Q_{Y_G} show a higher sensitivity towards the wave direction than the vertical response types Z_G, M_{Y_G} and Q_{Z_G}, which can explain most of the differences between the experiment and

Table 6: Comparison of standard deviations for test 532 highlighting the directional sensitivity. The factor is defined as numerical/experiment.

Response	Position	Unit	Exp. [10]	Numerical			Factor		
				-89.0°	-89.5°	-90.0°	-89.0°	-89.5°	-90.0°
Y_G	Pos. 1	[m]	6.34e-02	9.49e-02	6.75e-02	4.96e-02	1.50	1.06	0.78
Y_G	Pos. 3	[m]	1.33e-01	1.36e-01	1.37e-01	1.38e-01	1.03	1.03	1.04
Y_G	Pos. 5	[m]	5.37e-02	7.53e-02	5.29e-02	4.96e-02	1.40	0.99	0.92
Z_G	Pos. 1	[m]	1.37e-01	1.31e-01	1.26e-01	1.19e-01	0.96	0.92	0.87
Z_G	Pos. 3	[m]	1.66e-01	1.73e-01	1.75e-01	1.75e-01	1.04	1.05	1.05
Z_G	Pos. 5	[m]	1.27e-01	1.08e-01	1.14e-01	1.19e-01	0.85	0.90	0.94
R_{X_G}	Pos. 1	[deg]	2.88e-01	3.66e-01	3.43e-01	3.23e-01	1.27	1.19	1.12
R_{X_G}	Pos. 3	[deg]	3.75e-01	5.85e-01	5.84e-01	5.84e-01	1.56	1.56	1.56
R_{X_G}	Pos. 5	[deg]	2.70e-01	2.85e-01	3.03e-01	3.23e-01	1.06	1.12	1.20
M_{Y_G}	Pos. 1	[kNm]	1.48e+04	1.32e+04	1.36e+04	1.40e+04	0.89	0.92	0.95
M_{Y_G}	Pos. 3	[kNm]	1.15e+04	8.50e+03	9.30e+03	9.77e+03	0.74	0.81	0.85
M_{Y_G}	Pos. 5	[kNm]	1.51e+04	1.46e+04	1.45e+04	1.42e+04	0.97	0.96	0.94
M_{Z_G}	Pos. 1	[kNm]	2.43e+04	2.94e+04	2.68e+04	2.52e+04	1.21	1.10	1.04
M_{Z_G}	Pos. 3	[kNm]	3.53e+04	3.73e+04	3.75e+04	3.79e+04	1.06	1.06	1.07
M_{Z_G}	Pos. 5	[kNm]	2.15e+04	2.54e+04	2.45e+04	2.52e+04	1.18	1.14	1.17
Q_{Z_G}	Pos. 1	[kN]	3.03e+02	2.20e+02	2.31e+02	2.41e+02	0.73	0.76	0.79
Q_{Z_G}	Pos. 3	[kN]	1.67e+02	5.28e+01	4.55e+01	3.87e+01	0.32	0.27	0.23
Q_{Z_G}	Pos. 5	[kN]	3.05e+02	2.55e+02	2.46e+02	2.37e+02	0.84	0.81	0.78
Q_{Y_G}	Pos. 1	[kN]	4.05e+02	3.93e+02	3.94e+02	3.98e+02	0.97	0.97	0.98
Q_{Y_G}	Pos. 3	[kN]	1.21e+02	1.16e+02	7.39e+01	6.09e+01	0.95	0.61	0.50
Q_{Y_G}	Pos. 5	[kN]	3.96e+02	3.48e+02	3.47e+02	3.42e+02	0.88	0.87	0.86
F_{X_G}	End 1	[kN]	2.03e+03	1.93e+03	1.91e+03	1.91e+03	0.95	0.94	0.94
F_{X_G}	End 2	[kN]	2.02e+03	1.87e+03	1.89e+03	1.91e+03	0.93	0.93	0.95
Q_{Y_G}	End 1	[kN]	7.05e+02	6.24e+02	5.90e+02	5.59e+02	0.89	0.84	0.79
Q_{Y_G}	End 2	[kN]	6.48e+02	5.09e+02	5.30e+02	5.59e+02	0.79	0.82	0.86
Q_{Z_G}	End 1	[kN]	5.29e+02	4.88e+02	4.90e+02	4.92e+02	0.92	0.93	0.93
Q_{Z_G}	End 2	[kN]	4.84e+02	4.85e+02	4.91e+02	4.92e+02	1.00	1.01	1.02
M_{X_G}	End 1	[kNm]	4.30e+03	3.47e+03	3.52e+03	3.62e+03	0.81	0.82	0.84
M_{X_G}	End 2	[kNm]	4.25e+03	3.86e+03	3.71e+03	3.62e+03	0.91	0.87	0.85

the numerical model. Figure 7 highlights the directional sensitivity in the corresponding response spectra of the horizontal response types and also R_{X_G} at locations along the bridge where they are most influenced. It is clear that the energy around the first horizontal mode Y2 is strongly influenced by the small changes in the wave direction. The mode is clearly present in the measured response spectra, while it is only present in the response spectra from the computed response types for wave directions -89.0° and -89.5° due to the symmetrical properties of the numerical model. The shapes of the response spectra compare best at -89.5°. This is also seen in the factors listed in Tab. 6, where the standard deviations of the computed horizontal response fit best at that particular wave direction. Looking at the average factor for each response type over all the listed positions for -89.5°, the horizontal response types Y_G, M_{Z_G} and Q_{Y_G} are within 3%, 10% and 18% of the experiment. Some of the remaining differences for the horizontal response types are related to the energy in the response spectra around mode Y3, where the numerical model have relatively larger amplitudes, depending on the response type. The energy around this mode, however, does not seem to be affected by changes in the wave direction.

The average factor for the vertical response types Z_G, M_{Y_G} and Q_{Z_G} for -89.5°, are within 4%, 10% and 24% of the experiments, respectively. The largest outlier is the vertical shear force at Pos. 3, with a factor of 0.27. This is mainly connected to the uncertainty of 64 kN in the measurements combined with the relatively small standard deviation values at this position equivalent to 0.01% of the yield stress capacity of the bridge girder cross-section used in the experiment. Excluding this outlier then the average Q_{Z_G} response is only 13% lower than that of the experiment, with the best comparison at the two ends of the bridge. This uncertainty also influences the measured Q_{Y_G} response at Pos. 3.

The torsional rotation R_{X_G} of the bridge seems to compare poorly with an average factor of 1.29 along the bridge and with a factor of 1.56 at Pos. 3 for -89.5°. Furthermore, the response shows a low sensitivity towards changes in the wave direction. From Fig. 7 it seems that the numerical model overestimates the torsional response at the peak period of the wave spectrum

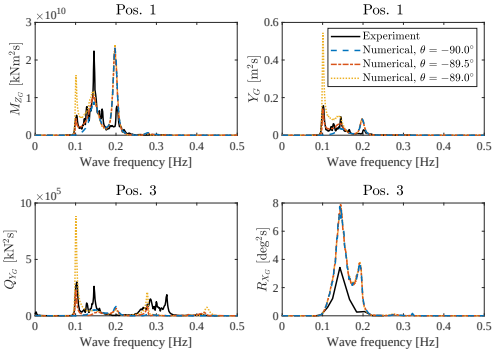

Figure 7: Directional sensitivity in response spectra for long-crested irregular wave test 532 [10, 11]

and at mode RX2 for beam sea. The accuracy of the rotation measurements are however 0.08°, corresponding to 21-30% of the measured values [10]. A similar study [13] between the same experiment and another numerical software found similar differences in the torsional rotation response.

The axial force F_{X_G} and the vertical shear force Q_{Z_G} at the two ends of the floating bridge show a low sensitivity towards the wave direction and are both well within the 10% uncertainty related to the measurements. Instead, the torsional moment M_{X_G} is roughly 15% different and is thought to be linked to the discrepancies observed for the torsional rotation.

Other less significant sources of error is the presence of transient effects such as slamming which was present during the experimental tests, especially for beam sea [11]. This effect is not included in the numerical model.

4.4.1. Sensitivity towards structural damping ratio

Due to the low potential damping from the pontoons at the natural period of mode Y3, it is worth investigating the influence from the amount of structural damping applied to the numerical model. The specified target structural damping ratio of 0.32% is for the entire range of active wave periods and the actual structural damping ratio value at the natural period of mode Y3 is instead 0.27%. Using a target structural damping ratio of 0.5% the actual damping ratio in the range of mode Y3 is 0.38%. The effect on the computed standard deviation values for the horizontal response types is, however, only 0.5%.

4.5. Short-crested irregular wave global response

Short-crested sea was investigated using the directional spreading function in Eqn. (4), with the spreading exponent $s = 2$ and the main wave direction $\theta_0 = -90.0°$ according to Tab. 4. In the experiments a total of up to 120 wave directions is possible using a *snake wave spectrum* [14] although the exact number used is uncertain. The default option in SIMO-RIFLEX is to specify an odd number of wave directions in the spreading function, although the option for manually defining a directional wave spectrum is also available. In the present paper the computed results are based on 101 equally distributed wave directions, although 12 was used in the numerical model in [11].

Table 7: Comparison of standard deviations for test 540. The factor is defined as numerical/experiment and the numerical model is based on $\theta_0 = -89.5°$.

Resp.	Pos.	Unit	Exp. [11]	Num.	Fac.
Y_G	Pos. 1	[m]	3.60e-02	4.13e-02	1.15
Y_G	Pos. 2	[m]	5.40e-02	5.41e-02	1.00
Y_G	Pos. 3	[m]	9.20e-02	9.96e-02	1.08
Z_G	Pos. 1	[m]	3.80e-02	4.49e-02	1.18
Z_G	Pos. 2	[m]	4.60e-02	4.66e-02	1.01
Z_G	Pos. 3	[m]	4.50e-02	4.44e-02	0.99
R_{X_G}	Pos. 3	[deg]	2.35e-01	3.11e-01	1.33
Q_{Z_G}	Pos. 1	[kN]	1.66e+02	1.60e+02	0.96
Q_{Z_G}	Pos. 3	[kN]	1.98e+02	1.53e+02	0.77
Q_{Y_G}	Pos. 1	[kN]	2.56e+02	2.62e+02	1.02
Q_{Y_G}	Pos. 3	[kN]	1.04e+02	1.05e+02	1.01
M_{Y_G}	Pos. 1	[kNm]	7.65e+03	8.14e+03	1.06
M_{Y_G}	Pos. 3	[kNm]	9.33e+03	9.38e+03	1.01
M_{Z_G}	Pos. 1	[kNm]	1.67e+04	1.90e+04	1.14
M_{Z_G}	Pos. 3	[kNm]	2.71e+04	2.81e+04	1.04
F_{X_G}	End 1	[kN]	1.20e+03	1.42e+03	1.18
Q_{Y_G}	End 1	[kN]	4.25e+02	3.91e+02	0.92
Q_{Z_G}	End 1	[kN]	2.06e+02	1.90e+02	0.92
M_{X_G}	End 1	[kNm]	3.49e+03	3.70e+03	1.06

A comparison of the response standard deviations is given in Tab. 7 showing a good agreement between computed and measured reponse in short-crested waves. Here, the main wave direction is -89.5°, although changes in the response when compared to waves from -90.0° is within 1%, which indicates that the response in short-crested waves is less sensitive to changes in the main wave direction. This is supported by [17] who showed a low sensitivity in the extreme response of a longer but similar floating pontoon bridge for main wave directions within 15° from beam sea. A check using 12, 13 and 51 wave directions indicate that for 12 and 13 wave directions, the results vary on average with 5% of the experimental values with some up to 13%. Instead the variation is on average less than 1% and up to 2% when using 51 and 101 wave directions.

4.6. Comparison of the current-wave interaction effect

Table 8 lists the measured and computed response standard deviations normalized by H_s for test 530, 531, 533 and 534 with varying H_s and U_c values. In the experiments with and without current, the same 6% increase in the response is found with increasing H_s. In the numerical model this effect is 9% in both cases. When H_s is kept constant in the experiments as in test 530 and 533 or 531 and 534, there is an average increase of 18% and 17% when adding current, respectively. This effect is also captured in the numerical model, although slightly smaller. When H_s is kept constant there is an 11% and 10% increase when adding a current to the low and high H_s cases, respectively. According to [11] there is a 17% increase with increasing H_s for cases with current, although this is found by

Table 8: Standard deviations normalized by H_s. Test 530 and 533 have lower H_s than test 531 and 534. The numerical model is based on $\theta = -89.5°$.

Resp.	Pos.	Unit	Experiment [11]				Numerical			
			U_c = 0.00 m/s		U_c = 0.92 m/s		U_c = 0.00 m/s		U_c = 0.92 m/s	
			530	531	533	534	530	531	533	534
Y_G	Pos. 1	[m/m]	3.48e-02	3.62e-02	4.14e-02	4.31e-02	4.92e-02	5.43e-02	5.49e-02	6.04e-02
Y_G	Pos. 2	[m/m]	5.90e-02	6.00e-02	6.65e-02	7.15e-02	7.21e-02	7.94e-02	8.06e-02	8.88e-02
Y_G	Pos. 3	[m/m]	9.92e-02	1.03e-01	1.15e-01	1.26e-01	1.37e-01	1.51e-01	1.53e-01	1.68e-01
Z_G	Pos. 1	[m/m]	2.95e-02	3.31e-02	3.37e-02	3.94e-02	2.18e-02	2.41e-02	2.19e-02	2.41e-02
Z_G	Pos. 2	[m/m]	3.29e-02	3.81e-02	4.05e-02	4.96e-02	3.27e-02	3.64e-02	3.12e-02	3.51e-02
Z_G	Pos. 3	[m/m]	3.89e-02	4.66e-02	4.73e-02	6.05e-02	3.90e-02	4.33e-02	3.78e-02	4.23e-02
R_{X_G}	Pos. 3	[deg/m]	1.81e-01	1.99e-01	1.93e-01	2.05e-01	3.20e-01	3.56e-01	3.17e-01	3.47e-01
M_{Y_G}	Pos. 1	[kNm/m]	7.40e+03	7.13e+03	8.79e+03	7.29e+03	4.87e+03	5.15e+03	6.30e+03	6.31e+03
M_{Z_G}	Pos. 1	[kNm/m]	1.69e+04	1.76e+04	1.95e+04	2.12e+04	2.50e+04	2.76e+04	2.79e+04	3.07e+04
M_{Z_G}	Pos. 3	[kNm/m]	2.80e+04	2.89e+04	3.23e+04	3.53e+04	3.79e+04	4.17e+04	4.23e+04	4.66e+04
Q_{Y_G}	Pos. 1	[kN/m]	3.12e+02	3.19e+02	3.62e+02	3.65e+02	3.76e+02	4.12e+02	4.31e+02	4.70e+02
F_{X_G}	End 1	[kN/m]	1.31e+03	1.41e+03	1.40e+03	1.54e+03	1.61e+03	1.76e+03	1.71e+03	1.87e+03
Q_{Y_G}	End 1	[kN/m]	4.94e+02	5.04e+02	5.70e+02	6.02e+02	5.38e+02	5.92e+02	6.10e+02	6.69e+02
Q_{Z_G}	End 1	[kN/m]	2.12e+02	2.18e+02	2.83e+02	2.51e+02	1.54e+02	1.65e+02	1.73e+02	1.79e+02
M_{X_G}	End 1	[kNm/m]	2.38e+03	2.73e+03	3.29e+03	3.12e+03	2.89e+03	3.00e+03	4.03e+03	4.06e+03

normalizing the response with the specified H_s and not the measured one.

5. Conclusion

An extensive model uncertainty assessment and experimental verification of the coupled hydro-elastic SIMO-RIFLEX program is presented for wave- and current-induced global response of a 830 m long end-anchored floating pontoon bridge.

An assessment of the sensitivity (effect) in the computed static and modal results is carried out for a list of known experimental model uncertainties. The list includes static horizontal load orientation (low), bridge girder bending stiffness (high), rotational spring stiffness at the two ends (medium), bridge girder torsional stiffness (low) and bridge girder torsional inertia (low). An agreement in static and modal properties is achieved by increasing the original bridge girder bending stiffness with 18% due to the relatively larger bending stiffness of the bending and shear force gauges inserted at the 1/4, 1/2 and 3/4 span of the bridge in the experiment. With the increased bending stiffness, the computed natural periods of the first three vertical modes and the first two horizontal modes corresponds to the peaks observed in the response spectra from the experiments with an accuracy within 5% and 1%, respectively.

The response amplitude operators (RAOs) are compared between the experimental model and time domain results for two wave directions showing a good agreement. Due to the symmetrical shape of the first horizontal mode, a high sensitivity towards the long-crested wave direction is found in the horizontal response close to beam sea, which explains most of the differences between the calculated and measured response. Insignificant changes are observed in the computed RAOs when changing the values of the applied drag coefficients with ±50%. This is assumed to be a consequence of the high amount of potential damping at the pontoons.

For irregular long-crested waves, a low sensitivity towards the structural damping ratio is found in the response and, similar to the RAOs, a high sensitivity in the horizontal response towards wave direction changes of 0.5° and 1.0° is found. Relatively large differences in the rotational response of the bridge is observed, which are partly due to a low accuracy in the measurements. Still, this finding indicates challenges regarding the modelling of the torsional motion of the floating bridge presented in the present paper.

For short-crested waves a low sensitivity towards the main wave direction is found in both the computed and measured response and a good agreement is found using 101 wave directions in the directional spreading function. The same comparison is valid using 51 wave directions but for 13 wave directions the uncertainty increases significantly.

In the case of adding current to the long-crested waves, a similar amplifying effect is observed in the measured and computed response. Due to lack of information, some uncertainty persists regarding whether or not the excitation effect increases with larger significant wave heights and further investigations are needed before any concluding remarks can be made.

Acknowledgements

This research was carried out with financial support from the NPRA. The authors greatly acknowledge this support and NPRA's permission to publish the experimental data.

References

[1] R. M. Larssen, B. J. Leira, S. N. Remseth, Structural parameter identification for marine bridges, in: Proceedings of the 15th International Con-

ference on Offshore Mechanics and Arctic Engineering, Vol. 2, Florence, 1996.

[2] Ø. W. Petersen, O. Øiseth, Sensitivity-based finite element model updating of a pontoon bridge, Engineering Structures 150 (2017) 573–584. doi:10.1016/j.engstruct.2017.07.025.

[3] K. A. Kvåle, O. Øiseth, A. Rønnquist, Operational modal analysis of an end-supported pontoon bridge, Engineering Structures 148 (2017) 410–423. doi:10.1016/j.engstruct.2017.06.069.

[4] SINTEF Ocean, SIMO 4.14.0 Theory Manual, Trondheim, Norway (2018).

[5] SINTEF Ocean, RIFLEX 4.14.0 Theory Manual, Trondheim, Norway (2018).

[6] T. Viuff, X. Xiang, B. J. Leira, O. Øiseth, Software-to-Software Comparison of End-Anchored Floating Bridge Global Analysis, Journal of Bridge Engineering, In Print.

[7] M. Karimirad, Q. Meissonnier, Z. Gao, T. Moan, Hydroelastic code-to-code comparison for a tension leg spar-type floating wind turbine, Marine Structures 24 (2011) 412–435. doi:10.1016/j.marstruc.2011.05.006.

[8] A. Robertson, J. Jonkman, F. Vorpahl, W. Popko, J. Qvist, L. Frøyd, X. Chen, J. Azcona, E. Uzunoglu, C. G. Soares, C. Luan, H. Yutong, F. Pengcheng, A. Yde, T. Larsen, J. Nichols, R. Buils, L. Lei, T. A. Nygaard, D. Manolas, A. Heege, S. R. Vatne, H. Ormberg, T. Duarte, C. Godreau, H. F. Hansen, A. W. Nielsen, H. Riber, C. L. Cunff, F. Beyer, A. Yamaguchi, K. J. Jung, H. Shin, W. Shi, H. Park, M. Alves, M. Gurinel, Offshore Code Comparison Collaboration Continuation Within IEA Wind Task 30: Phase II Results Regarding a Floating Semisubmersible Wind System, in: Proceedings of the 33rd International Conference on Ocean, Offshore and Arctic Engineering, ASME, 2014. doi:10.1115/OMAE2014-24040.

[9] S. H. Sørum, J.-T. H. Horn, J. Amdahl, Comparison of numerical response predictions for a bottom-fixed offshore wind turbine, Energy Procedia 137 (2017) 89–99. doi:10.1016/j.egypro.2017.10.336.

[10] Statens vegvesen, Modellforsøk med flytebru: Kontinuerlig pontongbru, Oslo, Norway, report no. MT40 F89-0252 (1989).

[11] Statens vegvesen, Sammenligning mellom modellforsøk og beregninger av en enkelt pongtong og en flytebru med separate pongtonger, Høvik, Norway, report no. 89-3440 (1990).

[12] A. E. Løken, R. A. Oftedal, Aspects of hydrodynamic loading and response in design of floating bridges, Second Symposium on Strait Crossings (1990) 479–486.

[13] X. Xiang, A. Løken, Hydroelastic analysis and validation of an end-anchored floating bridge under wave and current loads, in: Proceedings of the 38th International Conference on Offshore Mechanics and Arctic Engineering, 2019, pp. 1–9.

[14] H. Næser, NHL - Ocean Basin Capabilities and Limitations, in: Proceedings of the International Symposium on Hydrodynamics in Ocean Engineering, Trondheim, Vol. 2, The Norwegian Institute of Technology, 1981, pp. 1191–1210.

[15] K. Hasselmann, T. P. Barnett, E. Bouws, H. Carlson, D. E. Cartwright, K. Enke, J. A. Ewing, H. Gienapp, D. E. Hasselmann, P. Kruseman, A. Meerburg, P. Muller, D. J. Olbers, K. Richter, W. Sell, H. Walden, Measurements of Wind-Wave Growth and Swell Decay during the Joint North Sea Wave Project (JONSWAP), Deutsche Hydrographische Zeitschrift 8 (12).

[16] Y. Goda, Numerical experiments on wave statistics with spectral simulation, Report Port Harbour Res. Inst. 9 (1970) 3–57.

[17] T. Viuff, B. J. Leira, X. Xiang, O. Øiseth, Effects of wave directionality on extreme response for a long end-anchored floating bridge, Applied Ocean Research 90 (2019) 101843. doi:10.1016/j.apor.2019.05.028.

[18] W. E. Cummins, The impulse response function and ship motions, Washington DC, USA, report no. DTMB-1661 (1962).
URL https://dome.mit.edu/handle/1721.3/49049

[19] DNV, Wadam - Wave analysis by diffraction and Morison theory, SESAM user manual, Høvik, Norway, Report no. 94-7100 (2014).

[20] Y. Shao, X. Xiang, J. Liu, Numerical investigation of wave-frequency pontoon responses of a floating bridge based on model test results, in: Proceedings of the 38th International Conference on Offshore Mechanics and Arctic Engineering, 2019.

[21] DNV, DNV-RP-C205 Environmental conditions and environmental loads, Oslo, Norway (2010).

[22] N. K. Delany, N. E. Sorensen, Low-speed drag of cylinders of various shapes, Washington, USA, technical note 3038 (1953).

[23] O. M. Faltinsen, Sea loads on ships and offshore structures, Cambridge University Press, 1993.

[24] R. Zhao, O. M. Faltinsen, J. R. Krokstad, V. Aanesland, Wave-current interaction effects on large-volume structures, Proc. Int. Conf. Behaviour of Offshore Structures 2 (1988) 623–638.

[25] B. Villoria, Floating bridge technology - prediction of extreme environmental load effects, in: Proceedings of the 35th International Conference on Ocean, Offshore and Arctic Engineering, ASME, 2016, pp. 1–8. doi:10.1115/OMAE2016-54433.

[26] I. Langen, R. Sigbjörnsson, On stochastic dynamics of floating bridges, Engineering Structures 2 (4) (1980) 209–216. doi:10.1016/0141-0296(80)90002-4.

[27] Orcina, OrcaFlex Documentation, Accessed January 22, 2020 (2019).
URL https://www.orcina.com/webhelp/OrcaFlex/

Previous Ph.D. theses published at the department

List of previous Ph.D. theses published at the Department of Marine Technology in the Norwegian University of Science and Technology

Previous Ph.D. Theses published at the Department of Marine Technology (earlier: Faculty of Marine Technology) NORWEGIAN UNIVERSITY OF SCIENCE AND TECHNOLOGY

Report No.	Author	Title
	Kavlie, Dag	Optimization of Plane Elastic Grillages, 1967
	Hansen, Hans R.	Man-Machine Communication and Data-Storage Methods in Ship Structural Design, 1971
	Gisvold, Kaare M.	A Method for non-linear mixed -integer programming and its Application to Design Problems, 1971
	Lund, Sverre	Tanker Frame Optimalization by means of SUMT-Transformation and Behaviour Models, 1971
	Vinje, Tor	On Vibration of Spherical Shells Interacting with Fluid, 1972
	Lorentz, Jan D.	Tank Arrangement for Crude Oil Carriers in Accordance with the new Anti-Pollution Regulations, 1975
	Carlsen, Carl A.	Computer-Aided Design of Tanker Structures, 1975
	Larsen, Carl M.	Static and Dynamic Analysis of Offshore Pipelines during Installation, 1976
UR-79-01	Brigt Hatlestad, MK	The finite element method used in a fatigue evaluation of fixed offshore platforms. (Dr.Ing. Thesis)
UR-79-02	Erik Pettersen, MK	Analysis and design of cellular structures. (Dr.Ing. Thesis)
UR-79-03	Sverre Valsgård, MK	Finite difference and finite element methods applied to nonlinear analysis of plated structures. (Dr.Ing. Thesis)
UR-79-04	Nils T. Nordsve, MK	Finite element collapse analysis of structural members considering imperfections and stresses due to fabrication. (Dr.Ing. Thesis)
UR-79-05	Ivar J. Fylling, MK	Analysis of towline forces in ocean towing systems. (Dr.Ing. Thesis)
UR-80-06	Nils Sandsmark, MM	Analysis of Stationary and Transient Heat Conduction by the Use of the Finite Element Method. (Dr.Ing. Thesis)
UR-80-09	Sverre Haver, MK	Analysis of uncertainties related to the stochastic modeling of ocean waves. (Dr.Ing. Thesis)
UR-81-15	Odland, Jonas	On the Strength of welded Ring stiffened cylindrical Shells primarily subjected to axial Compression
UR-82-17	Engesvik, Knut	Analysis of Uncertainties in the fatigue Capacity of Welded Joints

UR-82-18	Rye, Henrik	Ocean wave groups
UR-83-30	Eide, Oddvar Inge	On Cumulative Fatigue Damage in Steel Welded Joints
UR-83-33	Mo, Olav	Stochastic Time Domain Analysis of Slender Offshore Structures
UR-83-34	Amdahl, Jørgen	Energy absorption in Ship-platform impacts
UR-84-37	Mørch, Morten	Motions and mooring forces of semi submersibles as determined by full-scale measurements and theoretical analysis
UR-84-38	Soares, C. Guedes	Probabilistic models for load effects in ship structures
UR-84-39	Aarsnes, Jan V.	Current forces on ships
UR-84-40	Czujko, Jerzy	Collapse Analysis of Plates subjected to Biaxial Compression and Lateral Load
UR-85-46	Alf G. Engseth, MK	Finite element collapse analysis of tubular steel offshore structures. (Dr.Ing. Thesis)
UR-86-47	Dengody Sheshappa, MP	A Computer Design Model for Optimizing Fishing Vessel Designs Based on Techno-Economic Analysis. (Dr.Ing. Thesis)
UR-86-48	Vidar Aanesland, MH	A Theoretical and Numerical Study of Ship Wave Resistance. (Dr.Ing. Thesis)
UR-86-49	Heinz-Joachim Wessel, MK	Fracture Mechanics Analysis of Crack Growth in Plate Girders. (Dr.Ing. Thesis)
UR-86-50	Jon Taby, MK	Ultimate and Post-ultimate Strength of Dented Tubular Members. (Dr.Ing. Thesis)
UR-86-51	Walter Lian, MH	A Numerical Study of Two-Dimensional Separated Flow Past Bluff Bodies at Moderate KC-Numbers. (Dr.Ing. Thesis)
UR-86-52	Bjørn Sortland, MH	Force Measurements in Oscillating Flow on Ship Sections and Circular Cylinders in a U-Tube Water Tank. (Dr.Ing. Thesis)
UR-86-53	Kurt Strand, MM	A System Dynamic Approach to One-dimensional Fluid Flow. (Dr.Ing. Thesis)
UR-86-54	Arne Edvin Løken, MH	Three Dimensional Second Order Hydrodynamic Effects on Ocean Structures in Waves. (Dr.Ing. Thesis)
UR-86-55	Sigurd Falch, MH	A Numerical Study of Slamming of Two-Dimensional Bodies. (Dr.Ing. Thesis)
UR-87-56	Arne Braathen, MH	Application of a Vortex Tracking Method to the Prediction of Roll Damping of a Two-Dimension Floating Body. (Dr.Ing. Thesis)
UR-87-57	Bernt Leira, MK	Gaussian Vector Processes for Reliability Analysis involving Wave-Induced Load Effects. (Dr.Ing. Thesis)
UR-87-58	Magnus Småvik, MM	Thermal Load and Process Characteristics in a Two-Stroke Diesel Engine with Thermal Barriers (in Norwegian). (Dr.Ing.

		Thesis)
MTA-88-59	Bernt Arild Bremdal, MP	An Investigation of Marine Installation Processes – A Knowledge-Based Planning Approach. (Dr.Ing. Thesis)
MTA-88-60	Xu Jun, MK	Non-linear Dynamic Analysis of Space-framed Offshore Structures. (Dr.Ing. Thesis)
MTA-89-61	Gang Miao, MH	Hydrodynamic Forces and Dynamic Responses of Circular Cylinders in Wave Zones. (Dr.Ing. Thesis)
MTA-89-62	Martin Greenhow, MH	Linear and Non-Linear Studies of Waves and Floating Bodies. Part I and Part II. (Dr.Techn. Thesis)
MTA-89-63	Chang Li, MH	Force Coefficients of Spheres and Cubes in Oscillatory Flow with and without Current. (Dr.Ing. Thesis
MTA-89-64	Hu Ying, MP	A Study of Marketing and Design in Development of Marine Transport Systems. (Dr.Ing. Thesis)
MTA-89-65	Arild Jæger, MH	Seakeeping, Dynamic Stability and Performance of a Wedge Shaped Planing Hull. (Dr.Ing. Thesis)
MTA-89-66	Chan Siu Hung, MM	The dynamic characteristics of tilting-pad bearings
MTA-89-67	Kim Wikstrøm, MP	Analysis av projekteringen for ett offshore projekt. (Licenciat-avhandling)
MTA-89-68	Jiao Guoyang, MK	Reliability Analysis of Crack Growth under Random Loading, considering Model Updating. (Dr.Ing. Thesis)
MTA-89-69	Arnt Olufsen, MK	Uncertainty and Reliability Analysis of Fixed Offshore Structures. (Dr.Ing. Thesis)
MTA-89-70	Wu Yu-Lin, MR	System Reliability Analyses of Offshore Structures using improved Truss and Beam Models. (Dr.Ing. Thesis)
MTA-90-71	Jan Roger Hoff, MH	Three-dimensional Green function of a vessel with forward speed in waves. (Dr.Ing. Thesis)
MTA-90-72	Rong Zhao, MH	Slow-Drift Motions of a Moored Two-Dimensional Body in Irregular Waves. (Dr.Ing. Thesis)
MTA-90-73	Atle Minsaas, MP	Economical Risk Analysis. (Dr.Ing. Thesis)
MTA-90-74	Knut-Aril Farnes, MK	Long-term Statistics of Response in Non-linear Marine Structures. (Dr.Ing. Thesis)
MTA-90-75	Torbjørn Sotberg, MK	Application of Reliability Methods for Safety Assessment of Submarine Pipelines. (Dr.Ing. Thesis)
MTA-90-76	Zeuthen, Steffen, MP	SEAMAID. A computational model of the design process in a constraint-based logic programming environment. An example from the offshore domain. (Dr.Ing. Thesis)
MTA-91-77	Haagensen, Sven, MM	Fuel Dependant Cyclic Variability in a Spark Ignition Engine - An Optical Approach. (Dr.Ing. Thesis)
MTA-91-78	Løland, Geir, MH	Current forces on and flow through fish farms. (Dr.Ing. Thesis)

MTA-91-79	Hoen, Christopher, MK	System Identification of Structures Excited by Stochastic Load Processes. (Dr.Ing. Thesis)
MTA-91-80	Haugen, Stein, MK	Probabilistic Evaluation of Frequency of Collision between Ships and Offshore Platforms. (Dr.Ing. Thesis)
MTA-91-81	Sødahl, Nils, MK	Methods for Design and Analysis of Flexible Risers. (Dr.Ing. Thesis)
MTA-91-82	Ormberg, Harald, MK	Non-linear Response Analysis of Floating Fish Farm Systems. (Dr.Ing. Thesis)
MTA-91-83	Marley, Mark J., MK	Time Variant Reliability under Fatigue Degradation. (Dr.Ing. Thesis)
MTA-91-84	Krokstad, Jørgen R., MH	Second-order Loads in Multidirectional Seas. (Dr.Ing. Thesis)
MTA-91-85	Molteberg, Gunnar A., MM	The Application of System Identification Techniques to Performance Monitoring of Four Stroke Turbocharged Diesel Engines. (Dr.Ing. Thesis)
MTA-92-86	Mørch, Hans Jørgen Bjelke, MH	Aspects of Hydrofoil Design: with Emphasis on Hydrofoil Interaction in Calm Water. (Dr.Ing. Thesis)
MTA-92-87	Chan Siu Hung, MM	Nonlinear Analysis of Rotordynamic Instabilities in Highspeed Turbomachinery. (Dr.Ing. Thesis)
MTA-92-88	Bessason, Bjarni, MK	Assessment of Earthquake Loading and Response of Seismically Isolated Bridges. (Dr.Ing. Thesis)
MTA-92-89	Langli, Geir, MP	Improving Operational Safety through exploitation of Design Knowledge - an investigation of offshore platform safety. (Dr.Ing. Thesis)
MTA-92-90	Sævik, Svein, MK	On Stresses and Fatigue in Flexible Pipes. (Dr.Ing. Thesis)
MTA-92-91	Ask, Tor Ø., MM	Ignition and Flame Growth in Lean Gas-Air Mixtures. An Experimental Study with a Schlieren System. (Dr.Ing. Thesis)
MTA-86-92	Hessen, Gunnar, MK	Fracture Mechanics Analysis of Stiffened Tubular Members. (Dr.Ing. Thesis)
MTA-93-93	Steinebach, Christian, MM	Knowledge Based Systems for Diagnosis of Rotating Machinery. (Dr.Ing. Thesis)
MTA-93-94	Dalane, Jan Inge, MK	System Reliability in Design and Maintenance of Fixed Offshore Structures. (Dr.Ing. Thesis)
MTA-93-95	Steen, Sverre, MH	Cobblestone Effect on SES. (Dr.Ing. Thesis)
MTA-93-96	Karunakaran, Daniel, MK	Nonlinear Dynamic Response and Reliability Analysis of Drag-dominated Offshore Platforms. (Dr.Ing. Thesis)
MTA-93-97	Hagen, Arnulf, MP	The Framework of a Design Process Language. (Dr.Ing. Thesis)
MTA-93-98	Nordrik, Rune, MM	Investigation of Spark Ignition and Autoignition in Methane and Air Using Computational Fluid Dynamics and Chemical Reaction Kinetics. A Numerical Study of Ignition Processes

		in Internal Combustion Engines. (Dr.Ing. Thesis)
MTA-94-99	Passano, Elizabeth, MK	Efficient Analysis of Nonlinear Slender Marine Structures. (Dr.Ing. Thesis)
MTA-94-100	Kvålsvold, Jan, MH	Hydroelastic Modelling of Wetdeck Slamming on Multihull Vessels. (Dr.Ing. Thesis)
MTA-94-102	Bech, Sidsel M., MK	Experimental and Numerical Determination of Stiffness and Strength of GRP/PVC Sandwich Structures. (Dr.Ing. Thesis)
MTA-95-103	Paulsen, Hallvard, MM	A Study of Transient Jet and Spray using a Schlieren Method and Digital Image Processing. (Dr.Ing. Thesis)
MTA-95-104	Hovde, Geir Olav, MK	Fatigue and Overload Reliability of Offshore Structural Systems, Considering the Effect of Inspection and Repair. (Dr.Ing. Thesis)
MTA-95-105	Wang, Xiaozhi, MK	Reliability Analysis of Production Ships with Emphasis on Load Combination and Ultimate Strength. (Dr.Ing. Thesis)
MTA-95-106	Ulstein, Tore, MH	Nonlinear Effects of a Flexible Stern Seal Bag on Cobblestone Oscillations of an SES. (Dr.Ing. Thesis)
MTA-95-107	Solaas, Frøydis, MH	Analytical and Numerical Studies of Sloshing in Tanks. (Dr.Ing. Thesis)
MTA-95-108	Hellan, Øyvind, MK	Nonlinear Pushover and Cyclic Analyses in Ultimate Limit State Design and Reassessment of Tubular Steel Offshore Structures. (Dr.Ing. Thesis)
MTA-95-109	Hermundstad, Ole A., MK	Theoretical and Experimental Hydroelastic Analysis of High Speed Vessels. (Dr.Ing. Thesis)
MTA-96-110	Bratland, Anne K., MH	Wave-Current Interaction Effects on Large-Volume Bodies in Water of Finite Depth. (Dr.Ing. Thesis)
MTA-96-111	Herfjord, Kjell, MH	A Study of Two-dimensional Separated Flow by a Combination of the Finite Element Method and Navier-Stokes Equations. (Dr.Ing. Thesis)
MTA-96-112	Æsøy, Vilmar, MM	Hot Surface Assisted Compression Ignition in a Direct Injection Natural Gas Engine. (Dr.Ing. Thesis)
MTA-96-113	Eknes, Monika L., MK	Escalation Scenarios Initiated by Gas Explosions on Offshore Installations. (Dr.Ing. Thesis)
MTA-96-114	Erikstad, Stein O., MP	A Decision Support Model for Preliminary Ship Design. (Dr.Ing. Thesis)
MTA-96-115	Pedersen, Egil, MH	A Nautical Study of Towed Marine Seismic Streamer Cable Configurations. (Dr.Ing. Thesis)
MTA-97-116	Moksnes, Paul O., MM	Modelling Two-Phase Thermo-Fluid Systems Using Bond Graphs. (Dr.Ing. Thesis)
MTA-97-117	Halse, Karl H., MK	On Vortex Shedding and Prediction of Vortex-Induced Vibrations of Circular Cylinders. (Dr.Ing. Thesis)
MTA-97-118	Igland, Ragnar T., MK	Reliability Analysis of Pipelines during Laying, considering

		Ultimate Strength under Combined Loads. (Dr.Ing. Thesis)
MTA-97-119	Pedersen, Hans-P., MP	Levendefiskteknologi for fiskefartøy. (Dr.Ing. Thesis)
MTA-98-120	Vikestad, Kyrre, MK	Multi-Frequency Response of a Cylinder Subjected to Vortex Shedding and Support Motions. (Dr.Ing. Thesis)
MTA-98-121	Azadi, Mohammad R. E., MK	Analysis of Static and Dynamic Pile-Soil-Jacket Behaviour. (Dr.Ing. Thesis)
MTA-98-122	Ulltang, Terje, MP	A Communication Model for Product Information. (Dr.Ing. Thesis)
MTA-98-123	Torbergsen, Erik, MM	Impeller/Diffuser Interaction Forces in Centrifugal Pumps. (Dr.Ing. Thesis)
MTA-98-124	Hansen, Edmond, MH	A Discrete Element Model to Study Marginal Ice Zone Dynamics and the Behaviour of Vessels Moored in Broken Ice. (Dr.Ing. Thesis)
MTA-98-125	Videiro, Paulo M., MK	Reliability Based Design of Marine Structures. (Dr.Ing. Thesis)
MTA-99-126	Mainçon, Philippe, MK	Fatigue Reliability of Long Welds Application to Titanium Risers. (Dr.Ing. Thesis)
MTA-99-127	Haugen, Elin M., MH	Hydroelastic Analysis of Slamming on Stiffened Plates with Application to Catamaran Wetdecks. (Dr.Ing. Thesis)
MTA-99-128	Langhelle, Nina K., MK	Experimental Validation and Calibration of Nonlinear Finite Element Models for Use in Design of Aluminium Structures Exposed to Fire. (Dr.Ing. Thesis)
MTA-99-129	Berstad, Are J., MK	Calculation of Fatigue Damage in Ship Structures. (Dr.Ing. Thesis)
MTA-99-130	Andersen, Trond M., MM	Short Term Maintenance Planning. (Dr.Ing. Thesis)
MTA-99-131	Tveiten, Bård Wathne, MK	Fatigue Assessment of Welded Aluminium Ship Details. (Dr.Ing. Thesis)
MTA-99-132	Søreide, Fredrik, MP	Applications of underwater technology in deep water archaeology. Principles and practice. (Dr.Ing. Thesis)
MTA-99-133	Tønnessen, Rune, MH	A Finite Element Method Applied to Unsteady Viscous Flow Around 2D Blunt Bodies With Sharp Corners. (Dr.Ing. Thesis)
MTA-99-134	Elvekrok, Dag R., MP	Engineering Integration in Field Development Projects in the Norwegian Oil and Gas Industry. The Supplier Management of Norne. (Dr.Ing. Thesis)
MTA-99-135	Fagerholt, Kjetil, MP	Optimeringsbaserte Metoder for Ruteplanlegging innen skipsfart. (Dr.Ing. Thesis)
MTA-99-136	Bysveen, Marie, MM	Visualization in Two Directions on a Dynamic Combustion Rig for Studies of Fuel Quality. (Dr.Ing. Thesis)
MTA-2000-137	Storteig, Eskild, MM	Dynamic characteristics and leakage performance of liquid annular seals in centrifugal pumps. (Dr.Ing. Thesis)

MTA-2000-138	Sagli, Gro, MK	Model uncertainty and simplified estimates of long term extremes of hull girder loads in ships. (Dr.Ing. Thesis)
MTA-2000-139	Tronstad, Harald, MK	Nonlinear analysis and design of cable net structures like fishing gear based on the finite element method. (Dr.Ing. Thesis)
MTA-2000-140	Kroneberg, André, MP	Innovation in shipping by using scenarios. (Dr.Ing. Thesis)
MTA-2000-141	Haslum, Herbjørn Alf, MH	Simplified methods applied to nonlinear motion of spar platforms. (Dr.Ing. Thesis)
MTA-2001-142	Samdal, Ole Johan, MM	Modelling of Degradation Mechanisms and Stressor Interaction on Static Mechanical Equipment Residual Lifetime. (Dr.Ing. Thesis)
MTA-2001-143	Baarholm, Rolf Jarle, MH	Theoretical and experimental studies of wave impact underneath decks of offshore platforms. (Dr.Ing. Thesis)
MTA-2001-144	Wang, Lihua, MK	Probabilistic Analysis of Nonlinear Wave-induced Loads on Ships. (Dr.Ing. Thesis)
MTA-2001-145	Kristensen, Odd H. Holt, MK	Ultimate Capacity of Aluminium Plates under Multiple Loads, Considering HAZ Properties. (Dr.Ing. Thesis)
MTA-2001-146	Greco, Marilena, MH	A Two-Dimensional Study of Green-Water Loading. (Dr.Ing. Thesis)
MTA-2001-147	Heggelund, Svein E., MK	Calculation of Global Design Loads and Load Effects in Large High Speed Catamarans. (Dr.Ing. Thesis)
MTA-2001-148	Babalola, Olusegun T., MK	Fatigue Strength of Titanium Risers – Defect Sensitivity. (Dr.Ing. Thesis)
MTA-2001-149	Mohammed, Abuu K., MK	Nonlinear Shell Finite Elements for Ultimate Strength and Collapse Analysis of Ship Structures. (Dr.Ing. Thesis)
MTA-2002-150	Holmedal, Lars E., MH	Wave-current interactions in the vicinity of the sea bed. (Dr.Ing. Thesis)
MTA-2002-151	Rognebakke, Olav F., MH	Sloshing in rectangular tanks and interaction with ship motions. (Dr.Ing. Thesis)
MTA-2002-152	Lader, Pål Furset, MH	Geometry and Kinematics of Breaking Waves. (Dr.Ing. Thesis)
MTA-2002-153	Yang, Qinzheng, MH	Wash and wave resistance of ships in finite water depth. (Dr.Ing. Thesis)
MTA-2002-154	Melhus, Øyvin, MM	Utilization of VOC in Diesel Engines. Ignition and combustion of VOC released by crude oil tankers. (Dr.Ing. Thesis)
MTA-2002-155	Ronæss, Marit, MH	Wave Induced Motions of Two Ships Advancing on Parallel Course. (Dr.Ing. Thesis)
MTA-2002-156	Økland, Ole D., MK	Numerical and experimental investigation of whipping in twin hull vessels exposed to severe wet deck slamming. (Dr.Ing. Thesis)
MTA-2002-157	Ge, Chunhua, MK	Global Hydroelastic Response of Catamarans due to Wet

		Deck Slamming. (Dr.Ing. Thesis)
MTA-2002-158	Byklum, Eirik, MK	Nonlinear Shell Finite Elements for Ultimate Strength and Collapse Analysis of Ship Structures. (Dr.Ing. Thesis)
IMT-2003-1	Chen, Haibo, MK	Probabilistic Evaluation of FPSO-Tanker Collision in Tandem Offloading Operation. (Dr.Ing. Thesis)
IMT-2003-2	Skaugset, Kjetil Bjørn, MK	On the Suppression of Vortex Induced Vibrations of Circular Cylinders by Radial Water Jets. (Dr.Ing. Thesis)
IMT-2003-3	Chezhian, Muthu	Three-Dimensional Analysis of Slamming. (Dr.Ing. Thesis)
IMT-2003-4	Buhaug, Øyvind	Deposit Formation on Cylinder Liner Surfaces in Medium Speed Engines. (Dr.Ing. Thesis)
IMT-2003-5	Tregde, Vidar	Aspects of Ship Design: Optimization of Aft Hull with Inverse Geometry Design. (Dr.Ing. Thesis)
IMT-2003-6	Wist, Hanne Therese	Statistical Properties of Successive Ocean Wave Parameters. (Dr.Ing. Thesis)
IMT-2004-7	Ransau, Samuel	Numerical Methods for Flows with Evolving Interfaces. (Dr.Ing. Thesis)
IMT-2004-8	Soma, Torkel	Blue-Chip or Sub-Standard. A data interrogation approach of identity safety characteristics of shipping organization. (Dr.Ing. Thesis)
IMT-2004-9	Ersdal, Svein	An experimental study of hydrodynamic forces on cylinders and cables in near axial flow. (Dr.Ing. Thesis)
IMT-2005-10	Brodtkorb, Per Andreas	The Probability of Occurrence of Dangerous Wave Situations at Sea. (Dr.Ing. Thesis)
IMT-2005-11	Yttervik, Rune	Ocean current variability in relation to offshore engineering. (Dr.Ing. Thesis)
IMT-2005-12	Fredheim, Arne	Current Forces on Net-Structures. (Dr.Ing. Thesis)
IMT-2005-13	Heggernes, Kjetil	Flow around marine structures. (Dr.Ing. Thesis)
IMT-2005-14	Fouques, Sebastien	Lagrangian Modelling of Ocean Surface Waves and Synthetic Aperture Radar Wave Measurements. (Dr.Ing. Thesis)
IMT-2006-15	Holm, Håvard	Numerical calculation of viscous free surface flow around marine structures. (Dr.Ing. Thesis)
IMT-2006-16	Bjørheim, Lars G.	Failure Assessment of Long Through Thickness Fatigue Cracks in Ship Hulls. (Dr.Ing. Thesis)
IMT-2006-17	Hansson, Lisbeth	Safety Management for Prevention of Occupational Accidents. (Dr.Ing. Thesis)
IMT-2006-18	Zhu, Xinying	Application of the CIP Method to Strongly Nonlinear Wave-Body Interaction Problems. (Dr.Ing. Thesis)
IMT-2006-19	Reite, Karl Johan	Modelling and Control of Trawl Systems. (Dr.Ing. Thesis)
IMT-2006-20	Smogeli, Øyvind Notland	Control of Marine Propellers. From Normal to Extreme

		Conditions. (Dr.Ing. Thesis)
IMT-2007-21	Storhaug, Gaute	Experimental Investigation of Wave Induced Vibrations and Their Effect on the Fatigue Loading of Ships. (Dr.Ing. Thesis)
IMT-2007-22	Sun, Hui	A Boundary Element Method Applied to Strongly Nonlinear Wave-Body Interaction Problems. (Ph.D. Thesis, CeSOS)
IMT-2007-23	Rustad, Anne Marthine	Modelling and Control of Top Tensioned Risers. (Ph.D. Thesis, CeSOS)
IMT-2007-24	Johansen, Vegar	Modelling flexible slender system for real-time simulations and control applications
IMT-2007-25	Wroldsen, Anders Sunde	Modelling and control of tensegrity structures. (Ph.D. Thesis, CeSOS)
IMT-2007-26	Aronsen, Kristoffer Høye	An experimental investigation of in-line and combined inline and cross flow vortex induced vibrations. (Dr. avhandling, IMT)
IMT-2007-27	Gao, Zhen	Stochastic Response Analysis of Mooring Systems with Emphasis on Frequency-domain Analysis of Fatigue due to Wide-band Response Processes. (Ph.D. Thesis, CeSOS)
IMT-2007-28	Thorstensen, Tom Anders	Lifetime Profit Modelling of Ageing Systems Utilizing Information about Technical Condition. (Dr.Ing. Thesis, IMT)
IMT-2008-29	Refsnes, Jon Erling Gorset	Nonlinear Model-Based Control of Slender Body AUVs. (Ph.D. Thesis, IMT)
IMT-2008-30	Berntsen, Per Ivar B.	Structural Reliability Based Position Mooring. (Ph.D. Thesis, IMT)
IMT-2008-31	Ye, Naiquan	Fatigue Assessment of Aluminium Welded Box-stiffener Joints in Ships. (Dr.Ing. Thesis, IMT)
IMT-2008-32	Radan, Damir	Integrated Control of Marine Electrical Power Systems. (Ph.D. Thesis, IMT)
IMT-2008-33	Thomassen, Paul	Methods for Dynamic Response Analysis and Fatigue Life Estimation of Floating Fish Cages. (Dr.Ing. Thesis, IMT)
IMT-2008-34	Pákozdi, Csaba	A Smoothed Particle Hydrodynamics Study of Two-dimensional Nonlinear Sloshing in Rectangular Tanks. (Dr.Ing. Thesis, IMT/ CeSOS)
IMT-2007-35	Grytøyr, Guttorm	A Higher-Order Boundary Element Method and Applications to Marine Hydrodynamics. (Dr.Ing. Thesis, IMT)
IMT-2008-36	Drummen, Ingo	Experimental and Numerical Investigation of Nonlinear Wave-Induced Load Effects in Containerships considering Hydroelasticity. (Ph.D. Thesis, CeSOS)
IMT-2008-37	Skejic, Renato	Maneuvering and Seakeeping of a Singel Ship and of Two Ships in Interaction. (Ph.D. Thesis, CeSOS)
IMT-2008-38	Harlem, Alf	An Age-Based Replacement Model for Repairable Systems with Attention to High-Speed Marine Diesel Engines. (Ph.D.

		Thesis, IMT)
IMT-2008-39	Alsos, Hagbart S.	Ship Grounding. Analysis of Ductile Fracture, Bottom Damage and Hull Girder Response. (Ph.D. Thesis, IMT)
IMT-2008-40	Graczyk, Mateusz	Experimental Investigation of Sloshing Loading and Load Effects in Membrane LNG Tanks Subjected to Random Excitation. (Ph.D. Thesis, CeSOS)
IMT-2008-41	Taghipour, Reza	Efficient Prediction of Dynamic Response for Flexible amd Multi-body Marine Structures. (Ph.D. Thesis, CeSOS)
IMT-2008-42	Ruth, Eivind	Propulsion control and thrust allocation on marine vessels. (Ph.D. Thesis, CeSOS)
IMT-2008-43	Nystad, Bent Helge	Technical Condition Indexes and Remaining Useful Life of Aggregated Systems. (Ph.D. Thesis, IMT)
IMT-2008-44	Soni, Prashant Kumar	Hydrodynamic Coefficients for Vortex Induced Vibrations of Flexible Beams. (Ph.D. Thesis, CeSOS)
IMT-2009-45	Amlashi, Hadi K.K.	Ultimate Strength and Reliability-based Design of Ship Hulls with Emphasis on Combined Global and Local Loads. (Ph.D. Thesis, IMT)
IMT-2009-46	Pedersen, Tom Arne	Bond Graph Modelling of Marine Power Systems. (Ph.D. Thesis, IMT)
IMT-2009-47	Kristiansen, Trygve	Two-Dimensional Numerical and Experimental Studies of Piston-Mode Resonance. (Ph.D. Thesis, CeSOS)
IMT-2009-48	Ong, Muk Chen	Applications of a Standard High Reynolds Number Model and a Stochastic Scour Prediction Model for Marine Structures. (Ph.D. Thesis, IMT)
IMT-2009-49	Hong, Lin	Simplified Analysis and Design of Ships subjected to Collision and Grounding. (Ph.D. Thesis, IMT)
IMT-2009-50	Koushan, Kamran	Vortex Induced Vibrations of Free Span Pipelines. (Ph.D. Thesis, IMT)
IMT-2009-51	Korsvik, Jarl Eirik	Heuristic Methods for Ship Routing and Scheduling. (Ph.D. Thesis, IMT)
IMT-2009-52	Lee, Jihoon	Experimental Investigation and Numerical in Analyzing the Ocean Current Displacement of Longlines. (Ph.D. Thesis, IMT).
IMT-2009-53	Vestbøstad, Tone Gran	A Numerical Study of Wave-in-Deck Impact usin a Two-Dimensional Constrained Interpolation Profile Method. (Ph.D. Thesis, CeSOS)
IMT-2009-54	Bruun, Kristine	Bond Graph Modelling of Fuel Cells for Marine Power Plants. (Ph.D. Thesis, IMT)
IMT-2009-55	Holstad, Anders	Numerical Investigation of Turbulence in a Sekwed Three-Dimensional Channel Flow. (Ph.D. Thesis, IMT)

IMT-2009-56	Ayala-Uraga, Efren	Reliability-Based Assessment of Deteriorating Ship-shaped Offshore Structures. (Ph.D. Thesis, IMT)
IMT-2009-57	Kong, Xiangjun	A Numerical Study of a Damaged Ship in Beam Sea Waves. (Ph.D. Thesis, IMT/CeSOS)
IMT-2010-58	Kristiansen, David	Wave Induced Effects on Floaters of Aquaculture Plants. (Ph.D. Thesis, CeSOS)
IMT-2010-59	Ludvigsen, Martin	An ROV-Toolbox for Optical and Acoustic Scientific Seabed Investigation. (Ph.D. Thesis, IMT)
IMT-2010-60	Hals, Jørgen	Modelling and Phase Control of Wave-Energy Converters. (Ph.D. Thesis, CeSOS)
IMT-2010- 61	Shu, Zhi	Uncertainty Assessment of Wave Loads and Ultimate Strength of Tankers and Bulk Carriers in a Reliability Framework. (Ph.D. Thesis, IMT/ CeSOS)
IMT-2010-62	Shao, Yanlin	Numerical Potential-Flow Studies on Weakly-Nonlinear Wave-Body Interactions with/without Small Forward Speed. (Ph.D. Thesis, CeSOS)
IMT-2010-63	Califano, Andrea	Dynamic Loads on Marine Propellers due to Intermittent Ventilation. (Ph.D. Thesis, IMT)
IMT-2010-64	El Khoury, George	Numerical Simulations of Massively Separated Turbulent Flows. (Ph.D. Thesis, IMT)
IMT-2010-65	Seim, Knut Sponheim	Mixing Process in Dense Overflows with Emphasis on the Faroe Bank Channel Overflow. (Ph.D. Thesis, IMT)
IMT-2010-66	Jia, Huirong	Structural Analysis of Intect and Damaged Ships in a Collission Risk Analysis Perspective. (Ph.D. Thesis, CeSOS)
IMT-2010-67	Jiao, Linlin	Wave-Induced Effects on a Pontoon-type Very Large Floating Structures (VLFS). (Ph.D. Thesis, CeSOS)
IMT-2010-68	Abrahamsen, Bjørn Christian	Sloshing Induced Tank Roof with Entrapped Air Pocket. (Ph.D. Thesis, CeSOS)
IMT-2011-69	Karimirad, Madjid	Stochastic Dynamic Response Analysis of Spar-Type Wind Turbines with Catenary or Taut Mooring Systems. (Ph.D. Thesis, CeSOS)
IMT-2011-70	Erlend Meland	Condition Monitoring of Safety Critical Valves. (Ph.D. Thesis, IMT)
IMT-2011-71	Yang, Limin	Stochastic Dynamic System Analysis of Wave Energy Converter with Hydraulic Power Take-Off, with Particular Reference to Wear Damage Analysis. (Ph.D. Thesis, CeSOS)
IMT-2011-72	Visscher, Jan	Application of Particla Image Velocimetry on Turbulent Marine Flows. (Ph.D. Thesis, IMT)
IMT-2011-73	Su, Biao	Numerical Predictions of Global and Local Ice Loads on Ships. (Ph.D. Thesis, CeSOS)
IMT-2011-74	Liu, Zhenhui	Analytical and Numerical Analysis of Iceberg Collision with

		Ship Structures. (Ph.D. Thesis, IMT)
IMT-2011-75	Aarsæther, Karl Gunnar	Modeling and Analysis of Ship Traffic by Observation and Numerical Simulation. (Ph.D. Thesis, IMT)
IMT-2011-76	Wu, Jie	Hydrodynamic Force Identification from Stochastic Vortex Induced Vibration Experiments with Slender Beams. (Ph.D. Thesis, IMT)
IMT-2011-77	Amini, Hamid	Azimuth Propulsors in Off-design Conditions. (Ph.D. Thesis, IMT)
IMT-2011-78	Nguyen, Tan-Hoi	Toward a System of Real-Time Prediction and Monitoring of Bottom Damage Conditions During Ship Grounding. (Ph.D. Thesis, IMT)
IMT-2011-79	Tavakoli, Mohammad T.	Assessment of Oil Spill in Ship Collision and Grounding. (Ph.D. Thesis, IMT)
IMT-2011-80	Guo, Bingjie	Numerical and Experimental Investigation of Added Resistance in Waves. (Ph.D. Thesis, IMT)
IMT-2011-81	Chen, Qiaofeng	Ultimate Strength of Aluminium Panels, considering HAZ Effects, IMT
IMT-2012-82	Kota, Ravikiran S.	Wave Loads on Decks of Offshore Structures in Random Seas, CeSOS
IMT-2012-83	Sten, Ronny	Dynamic Simulation of Deep Water Drilling Risers with Heave Compensating System, IMT
IMT-2012-84	Berle, Øyvind	Risk and resilience in global maritime supply chains, IMT
IMT-2012-85	Fang, Shaoji	Fault Tolerant Position Mooring Control Based on Structural Reliability, CeSOS
IMT-2012-86	You, Jikun	Numerical studies on wave forces and moored ship motions in intermediate and shallow water, CeSOS
IMT-2012-87	Xiang ,Xu	Maneuvering of two interacting ships in waves, CeSOS
IMT-2012-88	Dong, Wenbin	Time-domain fatigue response and reliability analysis of offshore wind turbines with emphasis on welded tubular joints and gear components, CeSOS
IMT-2012-89	Zhu, Suji	Investigation of Wave-Induced Nonlinear Load Effects in Open Ships considering Hull Girder Vibrations in Bending and Torsion, CeSOS
IMT-2012-90	Zhou, Li	Numerical and Experimental Investigation of Station-keeping in Level Ice, CeSOS
IMT-2012-91	Ushakov, Sergey	Particulate matter emission characteristics from diesel enignes operating on conventional and alternative marine fuels, IMT

IMT-2013-1	Yin, Decao	Experimental and Numerical Analysis of Combined In-line and Cross-flow Vortex Induced Vibrations, CeSOS
IMT-2013-2	Kurniawan, Adi	Modelling and geometry optimisation of wave energy converters, CeSOS
IMT- 2013-3	Al Ryati, Nabil	Technical condition indexes doe auxiliary marine diesel engines, IMT
IMT-2013-4	Firoozkoohi, Reza	Experimental, numerical and analytical investigation of the effect of screens on sloshing, CeSOS
IMT-2013-5	Ommani, Babak	Potential-Flow Predictions of a Semi-Displacement Vessel Including Applications to Calm Water Broaching, CeSOS
IMT- 2013-6	Xing, Yihan	Modelling and analysis of the gearbox in a floating spar-type wind turbine, CeSOS
IMT-7-2013	Balland, Océane	Optimization models for reducing air emissions from ships, IMT
IMT-8-2013	Yang, Dan	Transitional wake flow behind an inclined flat plate - Computation and analysis, IMT
IMT-9-2013	Abdillah, Suyuthi	Prediction of Extreme Loads and Fatigue Damage for a Ship Hull due to Ice Action, IMT
IMT-10-2013	Ramìrez, Pedro Agustìn Pèrez	Ageing management and life extension of technical systems - Concepts and methods applied to oil and gas facilities, IMT
IMT-11-2013	Chuang, Zhenju	Experimental and Numerical Investigation of Speed Loss due to Seakeeping and Maneuvering, IMT
IMT-12-2013	Etemaddar, Mahmoud	Load and Response Analysis of Wind Turbines under Atmospheric Icing and Controller System Faults with Emphasis on Spar Type Floating Wind Turbines, IMT
IMT-13-2013	Lindstad, Haakon	Strategies and measures for reducing maritime CO2 emissons, IMT
IMT-14-2013	Haris, Sabril	Damage interaction analysis of ship collisions, IMT
IMT-15-2013	Shainee, Mohamed	Conceptual Design, Numerical and Experimental Investigation of a SPM Cage Concept for Offshore Mariculture, IMT
IMT-16-2013	Gansel, Lars	Flow past porous cylinders and effects of biofouling and fish behavior on the flow in and around Atlantic salmon net cages, IMT
IMT-17-2013	Gaspar, Henrique	Handling Aspects of Complexity in Conceptual Ship Design, IMT
IMT-18-2013	Thys, Maxime	Theoretical and Experimental Investigation of a Free Running Fishing Vessel at Small Frequency of Encounter, CeSOS
IMT-19-2013	Aglen, Ida	VIV in Free Spanning Pipelines, CeSOS

IMT-1-2014	Song, An	Theoretical and experimental studies of wave diffraction and radiation loads on a horizontally submerged perforated plate, CeSOS
IMT-2-2014	Rogne, Øyvind Ygre	Numerical and Experimental Investigation of a Hinged 5-body Wave Energy Converter, CeSOS
IMT-3-2014	Dai, Lijuan	Safe and efficient operation and maintenance of offshore wind farms, IMT
IMT-4-2014	Bachynski, Erin Elizabeth	Design and Dynamic Analysis of Tension Leg Platform Wind Turbines, CeSOS
IMT-5-2014	Wang, Jingbo	Water Entry of Freefall Wedged – Wedge motions and Cavity Dynamics, CeSOS
IMT-6-2014	Kim, Ekaterina	Experimental and numerical studies related to the coupled behavior of ice mass and steel structures during accidental collisions, IMT
IMT-7-2014	Tan, Xiang	Numerical investigation of ship's continuous- mode icebreaking in leverl ice, CeSOS
IMT-8-2014	Muliawan, Made Jaya	Design and Analysis of Combined Floating Wave and Wind Power Facilities, with Emphasis on Extreme Load Effects of the Mooring System, CeSOS
IMT-9-2014	Jiang, Zhiyu	Long-term response analysis of wind turbines with an emphasis on fault and shutdown conditions, IMT
IMT-10-2014	Dukan, Fredrik	ROV Motion Control Systems, IMT
IMT-11-2014	Grimsmo, Nils I.	Dynamic simulations of hydraulic cylinder for heave compensation of deep water drilling risers, IMT
IMT-12-2014	Kvittem, Marit I.	Modelling and response analysis for fatigue design of a semisubmersible wind turbine, CeSOS
IMT-13-2014	Akhtar, Juned	The Effects of Human Fatigue on Risk at Sea, IMT
IMT-14-2014	Syahroni, Nur	Fatigue Assessment of Welded Joints Taking into Account Effects of Residual Stress, IMT
IMT-1-2015	Bøckmann, Eirik	Wave Propulsion of ships, IMT
IMT-2-2015	Wang, Kai	Modelling and dynamic analysis of a semi-submersible floating vertical axis wind turbine, CeSOS
IMT-3-2015	Fredriksen, Arnt Gunvald	A numerical and experimental study of a two-dimensional body with moonpool in waves and current, CeSOS
IMT-4-2015	Jose Patricio Gallardo Canabes	Numerical studies of viscous flow around bluff bodies, IMT
IMT-5-2015	Vegard Longva	Formulation and application of finite element techniques for slender marine structures subjected to contact interactions, IMT

IMT-6-2015	Jacobus De Vaal	Aerodynamic modelling of floating wind turbines, CeSOS
IMT-7-2015	Fachri Nasution	Fatigue Performance of Copper Power Conductors, IMT
IMT-8-2015	Oleh I Karpa	Development of bivariate extreme value distributions for applications in marine technology, CeSOS
IMT-9-2015	Daniel de Almeida Fernandes	An output feedback motion control system for ROVs, AMOS
IMT-10-2015	Bo Zhao	Particle Filter for Fault Diagnosis: Application to Dynamic Positioning Vessel and Underwater Robotics, CeSOS
IMT-11-2015	Wenting Zhu	Impact of emission allocation in maritime transportation, IMT
IMT-12-2015	Amir Rasekhi Nejad	Dynamic Analysis and Design of Gearboxes in Offshore Wind Turbines in a Structural Reliability Perspective, CeSOS
IMT-13-2015	Arturo Jesùs Ortega Malca	Dynamic Response of Flexibles Risers due to Unsteady Slug Flow, CeSOS
IMT-14-2015	Dagfinn Husjord	Guidance and decision-support system for safe navigation of ships operating in close proximity, IMT
IMT-15-2015	Anirban Bhattacharyya	Ducted Propellers: Behaviour in Waves and Scale Effects, IMT
IMT-16-2015	Qin Zhang	Image Processing for Ice Parameter Identification in Ice Management, IMT
IMT-1-2016	Vincentius Rumawas	Human Factors in Ship Design and Operation: An Experiential Learning, IMT
IMT-2-2016	Martin Storheim	Structural response in ship-platform and ship-ice collisions, IMT
IMT-3-2016	Mia Abrahamsen Prsic	Numerical Simulations of the Flow around single and Tandem Circular Cylinders Close to a Plane Wall, IMT
IMT-4-2016	Tufan Arslan	Large-eddy simulations of cross-flow around ship sections, IMT
IMT-5-2016	Pierre Yves-Henry	Parametrisation of aquatic vegetation in hydraulic and coastal research, IMT
IMT-6-2016	Lin Li	Dynamic Analysis of the Instalation of Monopiles for Offshore Wind Turbines, CeSOS
IMT-7-2016	Øivind Kåre Kjerstad	Dynamic Positioning of Marine Vessels in Ice, IMT
IMT-8-2016	Xiaopeng Wu	Numerical Analysis of Anchor Handling and Fish Trawling Operations in a Safety Perspective, CeSOS
IMT-9-2016	Zhengshun Cheng	Integrated Dynamic Analysis of Floating Vertical Axis Wind Turbines, CeSOS

IMT-10-2016	Ling Wan	Experimental and Numerical Study of a Combined Offshore Wind and Wave Energy Converter Concept
IMT-11-2016	Wei Chai	Stochastic dynamic analysis and reliability evaluation of the roll motion for ships in random seas, CeSOS
IMT-12-2016	Øyvind Selnes Patricksson	Decision support for conceptual ship design with focus on a changing life cycle and future uncertainty, IMT
IMT-13-2016	Mats Jørgen Thorsen	Time domain analysis of vortex-induced vibrations, IMT
IMT-14-2016	Edgar McGuinness	Safety in the Norwegian Fishing Fleet – Analysis and measures for improvement, IMT
IMT-15-2016	Sepideh Jafarzadeh	Energy effiency and emission abatement in the fishing fleet, IMT
IMT-16-2016	Wilson Ivan Guachamin Acero	Assessment of marine operations for offshore wind turbine installation with emphasis on response-based operational limits, IMT
IMT-17-2016	Mauro Candeloro	Tools and Methods for Autonomous Operations on Seabed and Water Coumn using Underwater Vehicles, IMT
IMT-18-2016	Valentin Chabaud	Real-Time Hybrid Model Testing of Floating Wind Tubines, IMT
IMT-1-2017	Mohammad Saud Afzal	Three-dimensional streaming in a sea bed boundary layer
IMT-2-2017	Peng Li	A Theoretical and Experimental Study of Wave-induced Hydroelastic Response of a Circular Floating Collar
IMT-3-2017	Martin Bergström	A simulation-based design method for arctic maritime transport systems
IMT-4-2017	Bhushan Taskar	The effect of waves on marine propellers and propulsion
IMT-5-2017	Mohsen Bardestani	A two-dimensional numerical and experimental study of a floater with net and sinker tube in waves and current
IMT-6-2017	Fatemeh Hoseini Dadmarzi	Direct Numerical Simualtion of turbulent wakes behind different plate configurations
IMT-7-2017	Michel R. Miyazaki	Modeling and control of hybrid marine power plants
IMT-8-2017	Giri Rajasekhar Gunnu	Safety and effiency enhancement of anchor handling operations with particular emphasis on the stability of anchor handling vessels
IMT-9-2017	Kevin Koosup Yum	Transient Performance and Emissions of a Turbocharged Diesel Engine for Marine Power Plants
IMT-10-2017	Zhaolong Yu	Hydrodynamic and structural aspects of ship collisions

IMT-11-2017	Martin Hassel	Risk Analysis and Modelling of Allisions between Passing Vessels and Offshore Installations
IMT-12-2017	Astrid H. Brodtkorb	Hybrid Control of Marine Vessels – Dynamic Positioning in Varying Conditions
IMT-13-2017	Kjersti Bruserud	Simultaneous stochastic model of waves and current for prediction of structural design loads
IMT-14-2017	Finn-Idar Grøtta Giske	Long-Term Extreme Response Analysis of Marine Structures Using Inverse Reliability Methods
IMT-15-2017	Stian Skjong	Modeling and Simulation of Maritime Systems and Operations for Virtual Prototyping using co-Simulations
IMT-1-2018	Yingguang Chu	Virtual Prototyping for Marine Crane Design and Operations
IMT-2-2018	Sergey Gavrilin	Validation of ship manoeuvring simulation models
IMT-3-2018	Jeevith Hegde	Tools and methods to manage risk in autonomous subsea inspection,maintenance and repair operations
IMT-4-2018	Ida M. Strand	Sea Loads on Closed Flexible Fish Cages
IMT-5-2018	Erlend Kvinge Jørgensen	Navigation and Control of Underwater Robotic Vehicles
IMT-6-2018	Bård Stovner	Aided Intertial Navigation of Underwater Vehicles
IMT-7-2018	Erlend Liavåg Grotle	Thermodynamic Response Enhanced by Sloshing in Marine LNG Fuel Tanks
IMT-8-2018	Børge Rokseth	Safety and Verification of Advanced Maritime Vessels
IMT-9-2018	Jan Vidar Ulveseter	Advances in Semi-Empirical Time Domain Modelling of Vortex-Induced Vibrations
IMT-10-2018	Chenyu Luan	Design and analysis for a steel braceless semi-submersible hull for supporting a 5-MW horizontal axis wind turbine
IMT-11-2018	Carl Fredrik Rehn	Ship Design under Uncertainty
IMT-12-2018	Øyvind Ødegård	Towards Autonomous Operations and Systems in Marine Archaeology
IMT-13- 2018	Stein Melvær Nornes	Guidance and Control of Marine Robotics for Ocean Mapping and Monitoring
IMT-14-2018	Petter Norgren	Autonomous Underwater Vehicles in Arctic Marine Operations: Arctic marine research and ice monitoring
IMT-15-2018	Minjoo Choi	Modular Adaptable Ship Design for Handling Uncertainty in the Future Operating Context

MT-16-2018	Ole Alexander Eidsvik	Dynamics of Remotely Operated Underwater Vehicle Systems
IMT-17-2018	Mahdi Ghane	Fault Diagnosis of Floating Wind Turbine Drivetrain-Methodologies and Applications
IMT-18-2018	Christoph Alexander Thieme	Risk Analysis and Modelling of Autonomous Marine Systems
IMT-19-2018	Yugao Shen	Operational limits for floating-collar fish farms in waves and current, without and with well-boat presence
IMT-20-2018	Tianjiao Dai	Investigations of Shear Interaction and Stresses in Flexible Pipes and Umbilicals
IMT-21-2018	Sigurd Solheim Pettersen	Resilience by Latent Capabilities in Marine Systems
IMT-22-2018	Thomas Sauder	Fidelity of Cyber-physical Empirical Methods. Application to the Active Truncation of Slender Marine Structures
IMT-23-2018	Jan-Tore Horn	Statistical and Modelling Uncertainties in the Design of Offshore Wind Turbines
IMT-24-2018	Anna Swider	Data Mining Methods for the Analysis of Power Systems of Vessels
IMT-1-2019	Zhao He	Hydrodynamic study of a moored fish farming cage with fish influence
IMT-2-2019	Isar Ghamari	Numerical and Experimental Study on the Ship Parametric Roll Resonance and the Effect of Anti-Roll Tank
IMT-3-2019	Håkon Strandenes	Turbulent Flow Simulations at Higher Reynolds Numbers
IMT-4-2019	Siri Mariane Holen	Safety in Norwegian Fish Farming – Concepts and Methods for Improvement
IMT-5-2019	Ping Fu	Reliability Analysis of Wake-Induced Riser Collision
IMT-6-2019	Vladimir Krivopolianskii	Experimental Investigation of Injection and Combustion Processes in Marine Gas Engines using Constant Volume Rig
IMT-7-2019	Anna Maria Kozlowska	Hydrodynamic Loads on Marine Propellers Subject to Ventilation and out of Water Condition.
IMT-8-2019	Hans-Martin Heyn	Motion Sensing on Vessels Operating in Sea Ice: A Local Ice Monitoring System for Transit and Stationkeeping Operations under the Influence of Sea Ice
IMT-9-2019	Stefan Vilsen	Method for Real-Time Hybrid Model Testing of Ocean Structures – Case on Slender Marine Systems
IMT-10-2019	Finn-Christian W. Hanssen	Non-Linear Wave-Body Interaction in Severe Waves

IMT-11-2019	Trygve Olav Fossum	Adaptive Sampling for Marine Robotics
IMT-12-2019	Jørgen Bremnes Nielsen	Modeling and Simulation for Design Evaluation
IMT-13-2019	Yuna Zhao	Numerical modelling and dyncamic analysis of offshore wind turbine blade installation
IMT-14-2019	Daniela Myland	Experimental and Theoretical Investigations on the Ship Resistance in Level Ice
IMT-15-2019	Zhengru Ren	Advanced control algorithms to support automated offshore wind turbine installation
IMT-16-2019	Drazen Polic	Ice-propeller impact analysis using an inverse propulsion machinery simulation approach
IMT-17-2019	Endre Sandvik	Sea passage scenario simulation for ship system performance evaluation
IMT-18-2019	Loup Suja-Thauvin	Response of Monopile Wind Turbines to Higher Order Wave Loads
IMT-19-2019	Emil Smilden	Structural control of offshore wind turbines – Increasing the role of control design in offshore wind farm development
IMT-20-2019	Aleksandar-Sasa Milakovic	On equivalent ice thickness and machine learning in ship ice transit simulations
IMT-1-2020	Amrit Shankar Verma	Modelling, Analysis and Response-based Operability Assessment of Offshore Wind Turbine Blade Installation with Emphasis on Impact Damages
IMT-2-2020	Bent Oddvar Arnesen Haugaløkken	Autonomous Technology for Inspection, Maintenance and Repair Operations in the Norwegian Aquaculture
IMT-3-2020	Seongpil Cho	Model-based fault detection and diagnosis of a blade pitch system in floating wind turbines
IMT-4-2020	Jose Jorge Garcia Agis	Effectiveness in Decision-Making in Ship Design under Uncertainty
IMT-5-2020	Thomas Hansen Viuff	Uncertainty assessment of wave- and current-induced global response of floating bridges